

2022-12-01

Applications Of Micro-X-Ray Fluorescence (μ XRF) Techniques To Ore Formation Questions In Economic Geology

Hannah Adwoa Buamono
University of Texas at El Paso

Follow this and additional works at: https://scholarworks.utep.edu/open_etd



Part of the [Geology Commons](#)

Recommended Citation

Buamono, Hannah Adwoa, "Applications Of Micro-X-Ray Fluorescence (μ XRF) Techniques To Ore Formation Questions In Economic Geology" (2022). *Open Access Theses & Dissertations*. 3658.
https://scholarworks.utep.edu/open_etd/3658

This is brought to you for free and open access by ScholarWorks@UTEP. It has been accepted for inclusion in Open Access Theses & Dissertations by an authorized administrator of ScholarWorks@UTEP. For more information, please contact lweber@utep.edu.

APPLICATIONS OF MICRO-X-RAY FLUORESCENCE (μ XRF) TECHNIQUES TO ORE
FORMATION QUESTIONS IN ECONOMIC GEOLOGY

HANNAH A. BUAMONO

Master's Program in Geological Sciences

APPROVED:

Antonio Arribas, Ph.D., Chair

Hugo Gutierrez, Ph.D.

Guikuan Yue, Ph.D.

Stephen L. Crites, Jr., Ph.D.
Dean of the Graduate School

Dedication

I dedicate this thesis to my mother, Dora Buamono, who gave everything she had to ensure I had an opportunity to education. Her efforts motivated me to strive harder and achieve my goals.

APPLICATIONS OF MICRO-X-RAY FLUORESCENCE (μ XRF) TECHNIQUES TO ORE
FORMATION QUESTIONS IN ECONOMIC GEOLOGY

by

HANNAH A. BUAMONO

THESIS

Presented to the Faculty of the Graduate School of

The University of Texas at El Paso

in Partial Fulfillment

of the Requirements

for the Degree of

MASTER OF SCIENCE

Department of Earth, Environmental and Resource Sciences

THE UNIVERSITY OF TEXAS AT EL PASO

December 2022

Acknowledgements

I want to thank the Department of Earth, Environmental and Resource Sciences, especially my adviser, Dr. Antonio Arribas, for his guidance and support. Having him as an advisor is the best thing anyone could ever wish to have, and his mentorship has been invaluable to me. I sincerely thank my thesis committee members: Dr. Hugo Gutierrez and Dr. Guikuan Yue. I appreciate your time and support in this endeavor. I also want to thank Dr. Annette Veilleux, the department's graduate coordinator, for her patience and advice. In addition to Dr. Mark Engle and Dr. Benjamin Brunner, I would like to express my gratitude to them. Thank you, Nigel Kelly, of Bruker Nano Analytics, for taking the time and patience to train me on how to use the Micro-XRF. Also, I thank Mpho Keeditse, Renaldi Suhendra, and Imura Takumi for kindly providing the samples and the collaboration on the geologic questions in their respective project areas.

I am very grateful to my sister, Doris Gyamfi, for her love, continuous support, and prayers and to my Aunty, Augustina Frimpong, for her encouragement and prayers, both of whom spur on because they believe in me.

Thank you to my colleagues, Claudio Araya and David Muller, for their motivation and beautiful moments. My experience in UTEP couldn't have been better without them.

Abstract

Advances in x-ray optics over the past decade have enabled a new generation of benchtop micro energy-dispersive x-ray fluorescence (μ XRF/EDS) instruments to analyze samples with an x-ray spot size of 25 microns or less and detection limits of tens to hundreds of parts per million. The analysis of samples from mineral (ore) deposits may illustrate some of the capabilities and limitations of these instruments applied to geoscience problems. The qualitative elemental analysis process allows the production of detailed elemental maps which, together with line scan profiles and other petrographic and geochemical evidence, leads to a better definition of key chemical, structural and textural features. Importantly, minimal sample preparation is required to identify mineral phases in different sample types. Standardless quantification based on international standards and internal references results in highly reproducible results that allow a semi-quantitative analysis of a wide range of samples.

The main objective of this research project is to better understand mineralization processes in a variety of ore-forming environments through the visualization of key geologic parameters such as 1) mineralogical and chemical composition, 2) textures and textural relationship among ore and gangue, and 3) assessment of the timing of mineralization. For this purpose, samples were collected for the study from four deposits or mineralization environments: i) epithermal Au-Ag-(Sn-Se-Te) mineralization of Miocene age from the Rodalquilar deposit in Spain, ii) sediment-hosted Cu mineralization of pre-Cambrian age from the Khoemacau-Zone 5 deposit, Botswana, iii) metamorphic-rock hosted orogenic Au mineralization of uncertain age from Awak Mas, Indonesia, and iv) shallow geothermal and magmatic-hydrothermal alteration in crater lake sediments and altered volcanic rocks of the Adatarata volcano in central Japan.

Results from a representative sample of breccia vein from the Rodalquilar Au deposit show a complex sequence of alteration stages and mineralizing pulses that start with: i) barren wall rock hydrothermal alteration (Stage 1, white mica and alunite kaolinite) and continue with ii) strong silicification, pyrite and low grade Zn-Cu-Ag-Au-As mineralization (Stage 2), iii) fine grained, amorphous silica (banded) cavity fill with high-grade Au and Sn-W (Stage 3) and iv) late cavity fill of Se and pyrite. followed by Te. Silica precipitates through the evolution of the deposit, but by the time of Stage 3 silica is deposited as finely laminated bands of amorphous silica colloids, which implies formation temperature below 180°C. Overall, these observations suggest mineralization from consecutive pulses of magmatic-hydrothermal fluids from cooling and crystallizing magma at depth and decreasing temperature.

The study of multiple samples from the Khoemacau-Zone 5 Cu-Ag deposit in Botswana shows that the main-stage Cu mineralization is structurally controlled and associated with hydrothermal activity in an orogenic deformation setting. Chalcopyrite (CuFeS_2) and bornite (Cu_5FeS_4) display morphology, geometry, and timing characteristics of mineralization associated with post-peak metamorphism and deformation (cleavage) and are associated with quartz, illite and, carbonate gangue. Mineralization at Khoemacau is multi-stage and formed over a protracted period, which has broadly been associated with the Damaran orogeny. By contrast, diagenetic (framboidal) pyrite mineralization is a much older age and unrelated to the main Cu-Ag mineralizing event that characterizes the Kalahari Copperbelt.

Results from the Awak Mas Au deposit in Sulawesi, Indonesia, show that Au mineralization is also epigenetic and hydrothermal in origin and associated with sulfidation and albitization of the host rocks, which are significantly higher in Fe-rich hosts such as meta-hematitic mudstones and metavolcanic rocks. Mineralogical and textural relations indicate that Au

mineralization occurred by sulfidation during a stage (Stage 3) of hydrothermal quartz veining that followed barren Stage-2 carbonate veins.

The study of hot crater lake sediments from the Adataara volcano in central Japan presented an example of the type of sample that delivers a limited use of the μ XRF instrument. The crater lake sediments are very fine-grained (<0.1 mm) and present a very homogenous mineralogical and chemical composition, consisting of native S, silica, pyrite, and minor clays (i.e., S, Si, Fe, K, Al). The conclusion is that a lack of mineralogical (chemical) heterogeneity, a lack of elements with a higher atomic weight, and a very fine-grained nature of a sample may detract heavily from effective use of μ XRF applications.

The results from this study illustrate the value of an μ XRF/EDS instrument to the discipline of economic geology. Its application to well-selected and representative samples from three different deposit types highlights the potential to achieve a better understanding of the genetic processes of ore mineralization.

Table of Contents

Acknowledgments.....	iv
Abstract.....	v
Table of Contents.....	viii
List of Tables.....	x
List of Figures.....	xi
Chapter 1: Micro-XRF and applications to economic geology.....	1
1.1. Introduction.....	1
1.2. Research Problem.....	3
1.3. Research Objectives.....	4
Chapter 2: Experimental Methods.....	5
2.1. Analytical instrumentation.....	5
2.2. Qualitative analysis with μ XRF.....	8
2.3. Maximum pixel spectrum processing.....	10
2.4. Examples of previous ore-forming studies using μ XRF.....	12
Chapter 3: Gold-Ag-(Cu-Te-Se-Sn) mineralization, Rodalquilar deposit, Spain.....	14
3.1. Introduction.....	14
3.2. The Rodalquilar caldera complex and Au-Ag deposits.....	14
3.1. Samples and ore evolution.....	20
Chapter 4: Sediment-hosted Cu-Ag mineralization, Khoemacau Zone 5, Botswana.....	27
4.1 Introduction.....	27
4.2. Geologic Setting.....	29
4.3 Copper-Silver deposits of Khoemacau district.....	31
4.4. Analytical Parameters.....	32
4.5. Results.....	34
4.6. Discussion.....	44
Chapter 5: Gold mineralization, Awak Mas deposit, Sulawesi (Indonesia).....	47
5.1 Introduction.....	47
5.2 Geologic Setting.....	49

5.2.1	Alteration and Mineralization	51
5.3.	Analytical Parameters	52
5.4.	Results	53
5.4.1	Description of the ores	54
5.4.2	Mineral chemistry and bulk chemical composition	60
5.5	Discussion	61
Chapter 6:	Hydrothermal alteration in a hot crater late, Adatara volcano, Japan	66
6.3.	Samples	69
6.4.	Results and discussion	70
Chapter 7:	Conclusions	72
References	73
Appendix:	Micro-XRF user manual	84
Vita	93

List of Tables

Table 4.1: Analytical conditions for the Khoemacau Zone 5 deposit.....	33
Table 5.1: Analytical conditions for Awak Mas Au deposit.	53
Table 5.2: Major and trace element composition of host rocks and altered zones.	53
Table 6.1: Analytical conditions for Adatara crater lake sediment.	69

List of Figures

Figure 2.1: Schematic configuration of the Bruker M4 Tornado μ XRF system	5
Figure 2.2: Main components of the M4 Tornado	6
Figure 2.3: Sample chamber of the M4 Tornado	7
Figure 2.4: Example of drill core sample of porphyry copper ore ready for analysis.	9
Figure 2.5: Elemental map for same sample for Si ($K\alpha$) and K ($K\alpha$).....	9
Figure 2.6: A regular spectrum of sample ROD-340.....	11
Figure 2.7: Maximum pixel spectrum of sample ROD-340.	11
Figure 3.1: View of the Rodalquilar deposit located in the eastern wall of the Lomilla caldera (arcuate scarp). Gold was extracted from open pits and underground workings in caldera wall. 15	
Figure 3.2: (top) Geologic map of the Rodalquilar caldera complex in the Cabo de Gata volcanic field, SE Spain (inset map), showing the margins of the Rodalquilar and Lomilla calderas, major faults, and location of epithermal base metal and Ag-Au deposits. (bottom) Section through the Rodalquilar district (from Arribas et al., 1995, in Hedenquist et al., 1996).	15
Figure 3.3: (top) Alteration map of the Rodalquilar caldera; (bottom) Section A-A' showing generalized alteration pattern, based on drill hole samples (drill holes shown). The vuggy quartz core that hosts ore has outward and downward halos of advanced argillic and argillic alteration; the argillic alteration pinches out downward at depths >350 m and gives way to quartz-sericite alteration typical of porphyry systems (from Arribas et al., 1995, in Hedenquist et al., 1996)....	16
Figure 3.4: Schematic illustration of the relation between wall rock and chalcedonic quartz Au ore filling fractures and open spaces. Early acid wall rock alteration was followed by open space filling by breccia layers and mineralized/barren amorphous silica (Arribas et al., 1995).	17
Figure 3.5: Sample of hydrothermal vein breccia consisting of altered (vuggy quartz and advanced argillic) rhyolite (D) and earlier vein clasts (C_1) in a chalcedony matrix (C_2). Hypogene Au occurs as dark calaverite ($AuTe_2$)-bearing chalcedony.....	18
Figure 3.6: Banded chalcedonic ore at Rodalquilar: fracture filled with Au-bearing black, horizontally banded chalcedonic quartz. Some layers appear light in color due to weathering of sulfides. Average Au grade for the vein is 15 g/t; the Au content of the vuggy silica envelope is 1.3 g/t (Arribas et al. 1995).....	18
Figure 3.7: Elevation vs. temperature diagram showing range and average of fluid inclusion homogenization temperatures from Rodalquilar (Cinto) high-sulfidation deposit and the S-isotopic fractionation temperatures (circles) for coexisting pyrite-alunite pyrite. Hydrostatic boiling-point curve (for 5 wt% NaCl solution) and lithostatic pressure curve (for 25 wt% NaCl)	

are fitted to the data, suggesting low-salinity fluids were at hydrostatic pressures, whereas the younger higher temperature, higher salinity fluids (at a given depth) associated with quartz-sericite alteration were at lithostatic pressures, perhaps at paleodepths of only 600m. The present surface is 200-300 m beneath the paleosurface (from Arribas et al., 1995, in Hedenquist et al., 1996). 19

Figure 3.8: Minerals present in the Rodalquilar deposit (Arribas et al. 1995). While many minerals were identified, the details of the paragenetic sequence of the mineralization were incompletely defined..... 20

Figure 3.9: Sample selected for study from the Rodalquilar Cinto deposit (ROD-1). Image on the right is the mosaic image from the M4 Tornado; green outline indicates area analyzed. 21

Figure 3.10: Screen image of the Bruker M4 Tornado showing spectrum collected from sample ROD-1 (green outline in Fig. 3.9, right) 22

Figure 3.11: Complete spectrum with peaks and background identified..... 22

Figure 3.12: X-ray maps of elements corresponding to Stage 1 of wall rock alteration. 23

Figure 3.13: X-ray maps of elements corresponding to Stg. 2 of wall rock alteration, with strong silicification, pyrite and low-grade Zn-Cu-Ag-Au mineralization (ROD-1)..... 23

Figure 3.14: X-ray maps of elements corresponding to Stage 3, fine grained amorphous silica cavity fill with high-grade Au and Sn-W. The presence of Sr is not well understood (ROD-1).. 24

Figure 3.15: X-ray maps of elements corresponding to Stage 4, Se following Au-Sn-W, followed by Te. Pyrite (FeS₂) is present both in Stage 2 and Stage 4 (ROD-1). 24

Figure 3.16: Composite elemental maps showing two selections of elements that characterize the four stages of mineralization in sample ROD-1. Top image: Si (light gray), Pb (dark blue), Se (bright green), Ag (cyan), Au (yellow); bottom image: Si (light gray), Al (pink), Sn (light yellow), W (red), Pb (cyan), Se (bright green) 25

Figure 3.17: The entire chemical and mineralogical evolution of the high grade 340 hydrothermal breccia at Rodalquilar identified in a single sample with the help of the μ XRF. 26

Figure 4.1: Generalized geologic map and Cu-Ag deposits of the Ghanzi Ridge, Kalahari Copperbelt in Botswana. Geology is inferred from known geology and geophysics. The insert is a sub-continental Precambrian geology map of southern Africa showing the location of the Kalahari Copperbelt within which the focus (Ghanzi Ridge). The blue dotted line represents an arbitrary outline of the Kahalari Craton (after Keeditse et al., 2022). 28

Figure 4.2: (A) Left image shows the schematic lithostratigraphy of the Ghanzi-Chobe zone illustrating lithologic descriptions and ages of the basal volcanic suite and the overlying Ghanzi group as well as mineralization ages. (A) Right image shows the stratigraphic column of Zone 5 with its distinctive units and ore interval. (B) Sample assay results from the drill core section that

represented the Zone 5 ore interval and lithologies and mineral abundances. Bn, bornite; Cc, chalcocite; Cpy, chalcopyrite; Sp, sphalerite (after Keeditse et al., 2022).	30
Figure 4.3: Photomicrographs of diagenetic pyrite and associated sulfides at Khoemacau. (a) Backscattered electron image of fine-grained spheroidal-subhedral pyrite concentrated along laminations. (b) Framboidal pyrite coated by sphalerite (Keeditse et al., 2022).	32
Figure 4.4: Drill core samples are cut, without polishing, with minimal sample preparation. The red rectangles show the mapped areas (bottom, sample HD-1050D).	33
Figure 4.5: Photographs of the drill core samples from Zone 5 deposit, including: (a) HA-967D-01 (both sides): strongly sheared quartz-calcite-bornite-chalcocite vein at 7.2 % Cu; 68 ppm Ag. Veins associated with the ore are boudinaged because of shearing. (b) HA-1015b-03: boudinaged quartz-calcite-bornite-chalcocite vein at 15% Cu; 249 ppm Ag (Keeditse et al., 2022)	34
Figure 4.6: Micro-X-ray fluorescence image of sample HD-1050D showing the spatial distribution of single element maps of Si, Ca, K, Mn, S, Fe, Cu, and Al.	35
Figure 4.7: (A) Photograph of drill core of sample HD-1050D showing bedding parallel and crenulation cleavage-controlled mineralization. (B, C, D) Show the spatial distribution of Cu, K, Ca, Al, Si, Mn, and sulfide mineralization (bornite, chalcocite, chalcopyrite) along crenulation cleavages and in carbonate veins. Green mica layers are distinguished by their K and Al content (red and pink in B-D). Silicification (precipitation of hydrothermal quartz; bright green in C and D) is observed emanating from the vein that was later filled by rhodochrosite and calcite	36
Figure 4.8: (Left) is a spectrum showing sulfide minerals present (Cu, Fe, S) which corresponds to the μ XRF image on the right showing the object location of interest selected for spectrum collection.	37
Figure 4.9: Elemental maps of Ca, Si, Mn, S, Cu, Fe, As, Ti, and Ag (HA-715D-04).	38
Figure 4.10: Left: a spectrum showing the presence of native Ag. Right: a map showing the presence of native Ag within hotspots identified readily in the maximum pixel spectrum.	38
Figure 4.11: Elemental maps of Ca, Si, Mn, S, Cu, Fe, As, Ti, and Ag (HA-715D-04).	39
Figure 4.12: Top: Image of sample HA-1058D -04 showing sulfide mineralization along foliation. Bottom: Combined Cu, Si, S, Ca, Fe elemental map.	39
Figure 4.13: Elemental maps of Ca, Si, Mn, S, Cu, Fe, As, Ti, and Ag (HA-967D-01).	40
Figure 4.14: False map showing Ag, while the spectrum at the top shows no Ag peak.	40
Figure 4.15: Micro-X-ray fluorescence image of sample HA-1015b showing elemental map distribution of As, Fe, Ca, S, Si, Cu, Ti, and Mg.	41

Figure 4.16: Zone 5 Cu-Ag deposit paragenetic sequence observed in ore samples. As sphalerite is associated with pyrite and copper mineralization, another generation may occur during late hydrothermal activity (Keeditse et al., 2022).....	43
Figure 4.17: (A and B) host rock and μ XRF images showing traces of Ag in the sample selected from the maximum pixel spectrum; (C) Back-scattered electron image (BSE) showing native Ag around chalcocite.	43
Figure 5.1: Metamorphic rock belts and gold deposits by type in Eastern Indonesia (Harjanto and Meyer, 2015).....	47
Figure 5.2: Location map of the Awak Mas mesothermal gold deposit, Sulawesi Island, Indonesia (Harjanto and Meyer, 2015).	48
Figure 5.3: Geological map of the study area (White et al., 2017).....	49
Figure 5.4: Geological map showing mineralized zones with a north-south trend (modified from PT Masmindo Dwi Area). The position of section line AA' is shown in Figure 5.5.	51
Figure 5.5: Mineralized zones (orebodies) on the Salu Bulu prospect have steep east-dipping dips (modified from PT Masmindo Dwi Area).	52
Figure 5.6: Photographs of host rocks which consist of(a), carbonaceous mudstone (b), meta-(red) hematitic mudstone (c), chloritic meta volcanic (d), meta volcanic (e), carbonaceous metapelite (f), meta-volcanic (g), chlorite schist.	54
Figure 5.7: Mineral alteration and paragenetic sequence of the Salu Bulu prospect showing the three stages of hydrothermal activity and base- and precious-metal mineralization in the Awak Mas deposit (Renaldi Suhendra, Akita University; pers. comm. 2021). The details of Au mineralization with respect to three stages are not understood in detail. This is the objective of the study with a μ XRF study instrument.	55
Figure 5.8: Photographs of the main stages of vein mineralization.....	56
Figure 5.9: (left), host rock (right), micro-XRF maps showing the chemical and mineral variations of stage 1 vein (milky quartz) and the locations of elements of interest.....	56
Figure 5.10: (left), host rock (right), μ XRF maps showing the chemical and mineral variations of Stage 2 carbonate-albite vein with a small amount of hematite.	58
Figure 5.11: (left), host rock (right), μ XRF maps showing the chemical and mineral variations of Stage 3 vein (transparent quartz).	59
Figure 5.12: (left), host rock (right), μ XRF maps showing native Au in veins.....	59
Figure 5.13: Micro-XRF elemental maps showing gold (Au) in pyrite (FeS ₂) inclusion.....	60

Figure 5.14: (a,b) Host rock and photomicrograph showing native Au in strongly altered meta-hematitic mudstone, (c, d)Host rock and photomicrograph native Au along the contact between the vein and host rock.	61
Figure 5.15: Correlation heat map of elements from strongly altered zones.....	62
Figure 5.16: An analysis of the correlation between Au and other elements. The samples were taken from a zone of the strongly altered host rocks.	62
Figure 5.17: Photograph of carbonaceous mudstone representing zones of least and most altered as an example.....	64
Figure 5.18: Major elements oxide of least altered and intensely altered host rocks for six samples.....	65
Figure 6.1: (a) Location of Adatara Volcano; (b) view of Numanotaira crater looking southeast. The crater lake sediments studied here are the light gray units at the base and in the margins of the Numanotaira crater.....	66
Figure 6.2: Types of hydrothermal alteration of alteration at the.Numanotaira crater of Adatara volcano (see text for mineral abbreviations; Imura et al., in preparation).....	67
Figure 6.3: Field photographs of samples studied. (a) Large-platy block of the layered clay sediment in Locality. 16 of Numanotaira crater. (b): Large block of layered clay sediment in terrace deposit at Locality. 15 (Imura et al., in preparation).....	68
Figure 6.4: Sample of crater lake sediments from Adatara volcano (20180815-6).....	69
Figure 6.5: Micro-XRF elemental images of Adatara crater lake sediment: Fe, S (previous page), K, Ca and Si (above).....	71

Chapter 1: Micro-XRF and applications to economic geology

1.1. INTRODUCTION

In economic geology research, such as the study of the origin of hydrothermal mineral deposits, an in-depth understanding of the temporal and spatial relationships among alteration and ore minerals using optical or electron microscopy is vital to decipher the genesis and evolution of the mineralization. Advances in X-ray optics, energy dispersive X-ray detectors and computerized scanning (motorized) systems over the past decades have enabled a new generation of benchtop scanning micro-X-ray fluorescence (μ XRF) instruments capable of analyzing large samples with an X-ray spot size of 25 microns or less and detection limits of tens to hundreds of parts per million.

The analysis of geological samples from representative mineral deposits with the use of a state-of-the-art commercial μ XRF instrument is the main mission of this MSc research. The objective is to discover and illustrate the capabilities and limitations of these instruments applied to economic geology and, by extension, other geoscience applications. The qualitative analytical process of an μ XRF instrument allows the production of detailed elemental maps over large sample surfaces that have the potential to reveal key chemical, structural and textural features, including mineral zoning and distribution. Importantly, minimal sample preparation is required to identify mineral phases in different sample types.

In recent years, mineral mapping technologies have shown great value for large-scale mineralogical studies, such as infrared spectrographic imaging and quantitative scanning electron microscopy (qSEM; Gottlieb, 2008). This thesis focuses on scanning μ XRF, a well-proven analytical tool commonly used for the chemical mapping of rock samples at a very fine mm and submillimeter scale. When X-rays focus on a surface, the elemental composition can determine the spatial distribution of major, minor, and abundant trace elements (Fritz et al., 2016; Hoehnel,

2018). A wide range of geological applications can be achieved with μ XRF techniques on various sample types (e.g., drill core, pulps, thin sections).

The large sample chamber (600 x 350 mm²) and internal stage (190mm x 160mm) of the μ XRF instrument used in this research, a Bruker M4 Tornado can accommodate samples of different shapes and sizes. Rock samples up to 125 mm in length can be measured without reorienting. Measurements are taken at speeds of millimeters per second for precision. These measurements provide a qualitative overview of elemental distribution in large samples in either single-point or multipoint line scanning. As the sample stage moves, data is collected, allowing measurements to be performed "on-the-fly" and reducing analysis time. Elemental distribution in large samples can be qualitatively assessed through either single-point or multipoint line scanning. For accurate chemical quantification, a point scanning process with a defined dwell time is required.

Some examples of previous applications of geochemical analyses using μ XRF are discussed below and include studies of volcanogenic massive sulfide deposits (Genna et al., 2011), shale-hosted uranium deposits (Xu et al., 2015) and greenstone-hosted Cu-Co-Au mineralization (Fox et al., 2019). Applications in the environmental sciences include Croudace & Rothwell (2015) and Flude et al. (2017). Micro-XRF is used in these studies to visualize and, in some cases, quantify the elemental distributions (Flude et al., 2017). Through software, it is also possible to interpret the elemental chemical data obtained in terms of mineral species although this application is subject to limitations not observed with elemental maps generated with electron beams instead of X-ray radiation.

Benchtop μ -XRF is capable of (i) providing a geochemical signature for a large number of minerals and rocks, including light elements that cannot be analyzed with other methods in the

field, (ii) supporting exploration decision-making by conducting low-cost and real-time geochemical analyses, and (iii) providing microanalytical geochemistry and textural analysis in support of mineral identifications to unravel the rock record for complex, multiple-overprinting hydrothermal histories. The μ XRF instrument typically uses a theoretical quantification procedure. This process is known as fundamental parameterization. Fundamental parameters are derived from Sherman's equation (Sherman, 1955) and utilize the atomic parameters of individual elements (e.g., an X-ray intensity calculation is performed using the absorption, scattering, and emission parameters).

A fundamental parameter model also enables the collection of quantitative data from heterogeneous samples. This method calibrates XRF data and corrects matrix effects and can calculate the weight percent concentration of each element and then normalize it to 100%. A large selection of well-characterized reference materials comparable to project lithology and matrix densities is required (Kanngieser, 2003). Due to the larger spot size (3 to 8 mm) in these instruments, heterogeneity and grain size issues arise, especially in diamond drill core, so for quantitative analysis, good practices include pulverizing, sieving, and homogenizing. In this study, however, we have focused on qualitative analyses to investigate mineralogical and textural relations within the geologic context existing for each deposit. Thus, no quantitative analyses were conducted.

1.2. RESEARCH PROBLEM

The motivation for this research is to reach a better understanding of ore forming processes through the visualization of key geologic parameters such as, among others:

- 1) mineralogical and chemical composition,
- 2) textures and textural relationship among ore and gangue minerals, and

3) timing of mineralization, including post-mineralization events

Observation with the petrographic microscope is limited by the lack of chemical information, and the study with the scanning electron microscope equipped with energy-dispersive X-ray detector (SEM-EDS) is best applied to the micron scale. An analytical tool such as the μ XRF, which can provide cm to submillimeter scale chemical and textural information on a large (20 x 16 cm) sample, appears ideally suited to understand ore-forming processes.

1.3. RESEARCH OBJECTIVES

This study's objectives are to collect μ XRF data from hand specimens and split diamond drill core samples to identify mineralogy and the geochemical characteristics, sources, transport mechanisms, and depositional controls on mineralization, including post-mineralization modifications. In order to test a range of applications of the μ XRF system, samples were collected for study from four different types of deposit or ore-forming environment: i) epithermal Au-Ag-(Sn-Se-Te) mineralization of Miocene age from the Rodalquilar deposit in Spain, ii) sediment-hosted Cu mineralization of pre-Cambrian age from the Khoemacau-Zone 5 deposit, Botswana, iii) metamorphic-rock hosted orogenic Au mineralization of uncertain age from Awak Mas, Indonesia, and iv) shallow geothermal and magmatic-hydrothermal alteration in crater lake sediments and altered volcanic rocks of the Adataro volcano in central Japan. The study of these four projects should result in a better understanding of the genetic processes at a micron scale while analyzing hand-size specimens. Because of the different physical characteristics of the samples and deposit types the results should help inform the value and efficacy of μ XRF to applications in economic geology.

Chapter 2: Experimental Methods

2.1. ANALYTICAL INSTRUMENTATION

This study was conducted with a benchtop scanning μ XRF instrument, the M4 Tornado Plus, manufactured by Bruker Nano. The M4 Tornado has an Rh X-ray tube, Be window, and polycapillary optics that produce an X-ray beam of $\sim 25\ \mu\text{m}$ diameter on the sample (Fig. 2.1). The X-ray tube operating conditions can reach 50 kV and 600 μA ; however, their transmission function is low for higher energies, limiting the range available to excite high-energy lines (for example, Ba K-lines at 32 keV cannot be detected). A dual silicon drift detector (30 mm^2) measures X-rays with a resolution $<145\ \text{eV}$ at 250,000 cps (measured on $\text{MnK}\alpha$).

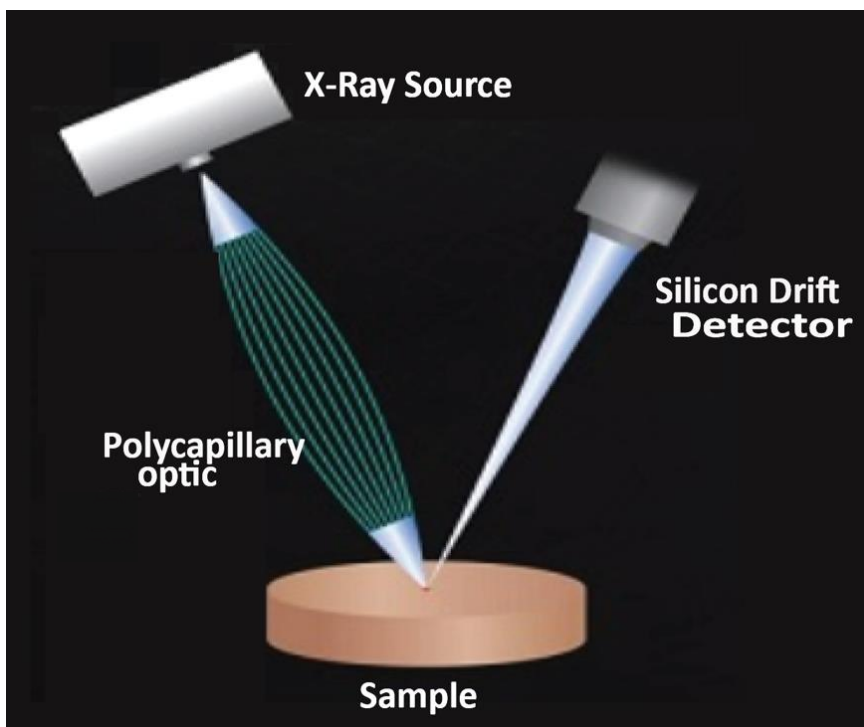


Figure 2.1: Schematic configuration of the Bruker M4 Tornado μ XRF system

A characteristic advantage of the M4 Tornado is that it has a large sample chamber (600 mm x 350 mm x 260 mm) that allows the study of relatively large samples. A pressure-controlled diaphragm pump enables analysis under atmospheric pressure and under vacuum (Fig. 2.2). A

sample can be analyzed without repositioning it on the stage if its dimensions are 200 x 160 mm and a height up to 125 mm (Fig. 2.3). The maximum sample weight load is 5 kg. For radiation protection and evacuation, the sample chamber must be closed. A three-camera system helps ensure the sample is positioned accurately: an overview camera is located in the door and allows a view into the sample chamber like a fisheye, and two additional cameras display the sample surface with different magnifications. A low magnification (x10) camera displays an area of approximately 15 x 11 mm², whereas the high magnification (x100) camera displays approximately 1.5 x 1.1 mm². The stage can be moved to adjacent sample positions and images captured from the sample are automatically stitched together to create a mosaic image for a brief orientation on large samples and as a optical reference for the sample spatial analysis. A graphic user interface displays simultaneously two of the images (e.g., mosaic, low magnification, high magnification, overview), facilitating the orientation of the sample and determining its final position.

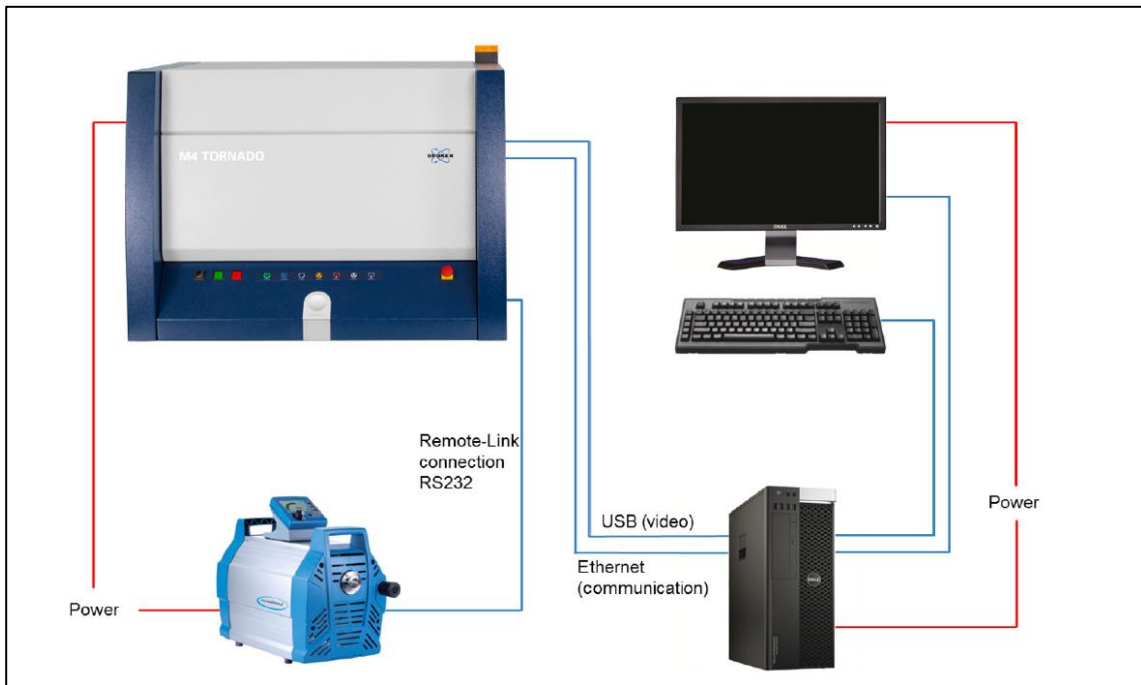


Figure 2.2: Main components of the M4 Tornado



Figure 2.3: Sample chamber of the M4 Tornado

An X-ray beam cannot be deflected to different positions unlike the electron beam in a scanning electron microscope; therefore, the stage must move the sample into position before measuring it. As a result, a motorized X-Y-Z stage operates with joysticks, mouse movements, or automatic functions such as autofocus. The stage in an M4 Tornado is powered by DC motors for rapid (200 mm/s) and smooth movement. Based on the displayed image, there is a 10x difference in speed between high and low magnifications.

For analysis of a sample, it is crucial to consider the beam spot size for exact sample positioning and optimal step size. The M4 Tornado measures "on-the-fly," i.e., the stage is continuously moving, and the detector is continually collecting data. During on-the-fly measurement, the stage must move at a stable, controlled speed to ensure high reproducibility. Before data acquisition can begin, the stage must accelerate to a fixed velocity. On-the-fly measurements produce ellipses rather than true circles, which is irrelevant for distribution analysis.

Analyzing these measurements provides a qualitative view of the sample's elemental distribution. For quantitative results, it is necessary to measure single points. The quantitative analysis only performs after the X-ray tube has been on for at least 1.5 hours to reduce errors caused by beam instability.

All analyses in this study were conducted under a vacuum of 20 mbar. The instrument was used in two modes: spot and area mapping (see below). An X-ray spectrum was collected for each pixel in a grid using the map function to create two-dimensional compositional maps; these maps are used to visualize elemental distributions and enable post-collection data processing, including, if required, semi-quantitative and standardless quantification of the map or parts of it. An algorithm based on fundamental parameters automatically corrects for detector artifacts such as pileups, escape peaks, and elements that are present in the spectrum but not in the sample (e.g., Rh from the tube radiation).

2.2. QUALITATIVE ANALYSIS WITH MXRF

An X-ray fluorescence instrument such as the M4 Tornado is most effective at producing large geochemical maps (up to 20 x 16 cm) with minimal sample preparation (Fig. 2.4). It is more suitable for analyzing large-scale samples with rough surfaces than SEM-EDS, and its excitation beam is larger than that of electron beams.

In many ways, this spatial distribution analysis is the same as SEM-EDS elemental mapping, except that no sample charge neutralization is required (conductive coating/neutralizing gas in the sample chamber) and larger samples (>0 cm) can be analyzed. For each pixel of a map, an entire x-ray spectrum is collected, which allows maps to display all elements that can be detected. Different rock and mineral phases can be easily identified by displaying multiple elements on the same map and selecting appropriate colors (Fig. 2.5).

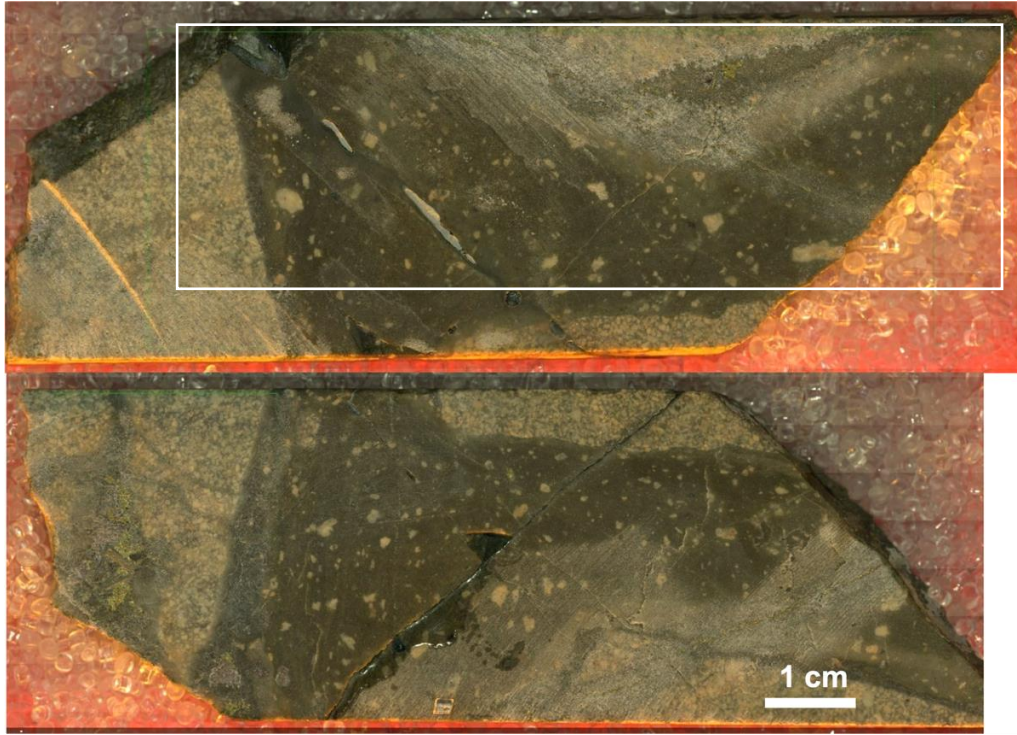


Figure 2.4: Example of drill core sample of porphyry copper ore ready for analysis.

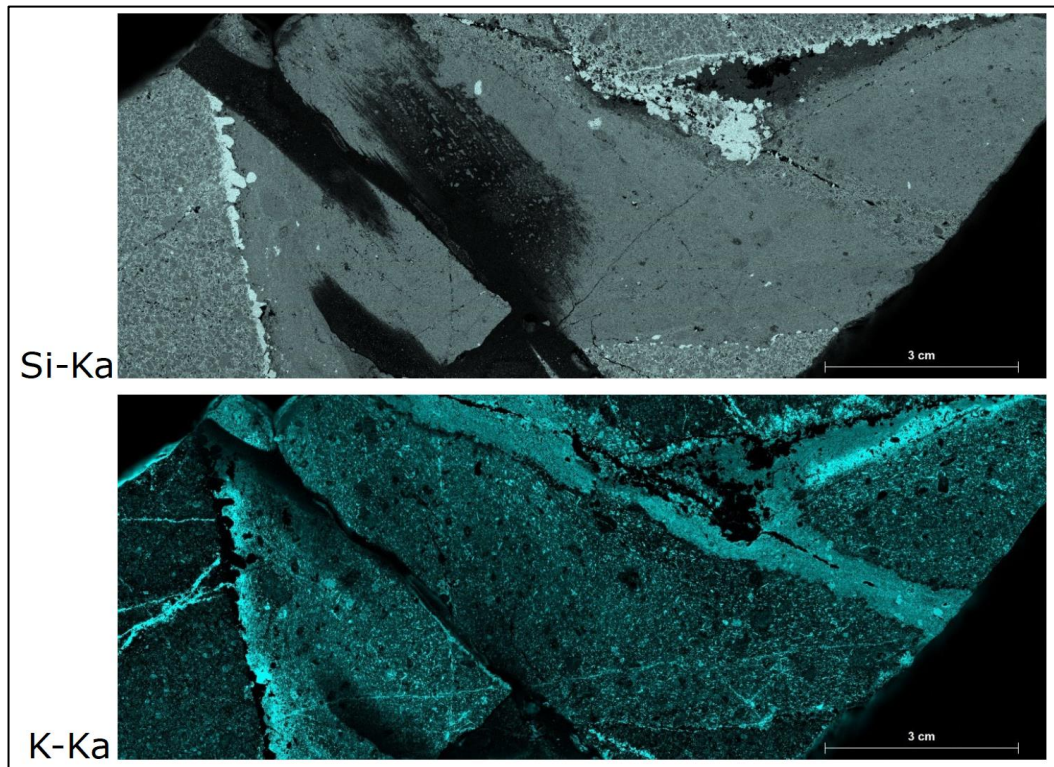


Figure 2.5: Elemental map for same sample for Si ($K\alpha$) and K ($K\alpha$).

Semi-quantitative analysis for single areas in an x-ray map is possible by selecting an area of the map and quantifying the spectrum that results from summing the individual pixels within the selected area. For element maps, the intensity of each pixel is dependent on the spectrum intensity in a pre-defined energy range (region of interest) corresponding to a given element. During X-ray analysis, elements that are difficult to separate, like Ba and Ti, can appear as a combination, although a map can be calculated based on any energy range. By minimizing the interference, this map gives a more accurate representation of the elements' distribution by minimizing the interference (for instance, the L- or M- lines).

The mapping of low-abundance elements can also be affected by interferences from spectral background or artifact peaks, such as pile-up and escape peaks from high-abundance elements. When analyzing crystalline material, special peaks can form in the spectrum due to the crystal lattice's diffraction of the polychromatic tube spectrum. Identifying these peaks can be hindered by changing the diffraction angle for a single crystal – e.g., by rotating or tilting it or moving it from one part of the crystal to another if it contains multiple domains with different crystallographic orientations. A map of these diffraction peaks may provide orientation contrast imaging in which qualitative differences in crystallographic orientation may be determined within and between minerals (cf. Prior et al. 1996).

2.3. MAXIMUM PIXEL SPECTRUM PROCESSING

The identification of minerals or features present in very small abundances or concentrations in a sample (e.g., identification of scattered gold particles) is aided greatly by processing a software function termed ‘maximum pixel spectrum’ (Bright and Newbury, 2004). To test and illustrate the value of the maximum pixel spectrum and the overall qualitative analytical capability of the M4 Tornado μ XRF instrument, a sample of complex Au-Ag-(Cu-Te-Se-Sn) ore

from the Rodalquilar deposit was used. This sample is particularly useful to illustrate the potential of this software routine because it contains a very diverse chemical composition, with a wide variety of minerals present. The sample contains rock forming minerals which contain elements of relatively low atomic number (Al, Si, K, Ca, Na, Mg) as well as ore minerals with elements in the high energy part of the spectrum (e.g., Au, Pb, Ag, Sn, etc.).

A comparison of the regular spectrum with the maximum pixel spectrum (Fig. 2.6 vs. Fig. 2.7) illustrates well the effective of this software tool in identifying elements such as Sr, Zr, Ni, and Mo that otherwise are invisible or barely visible in the regular (summation) pixel spectrum. The individual mineral particles can then be readily identified in the large sample surface.

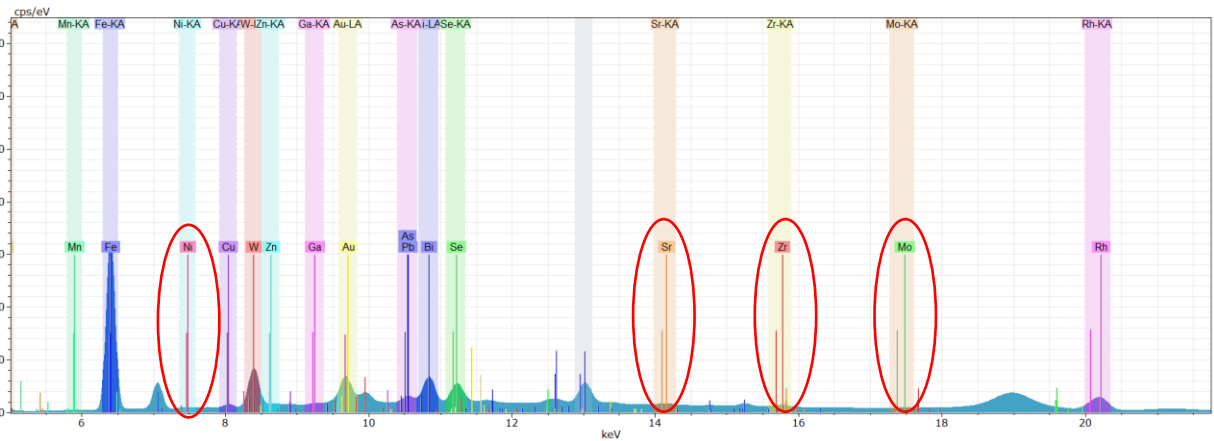


Figure 2.6: A regular spectrum of sample ROD-340

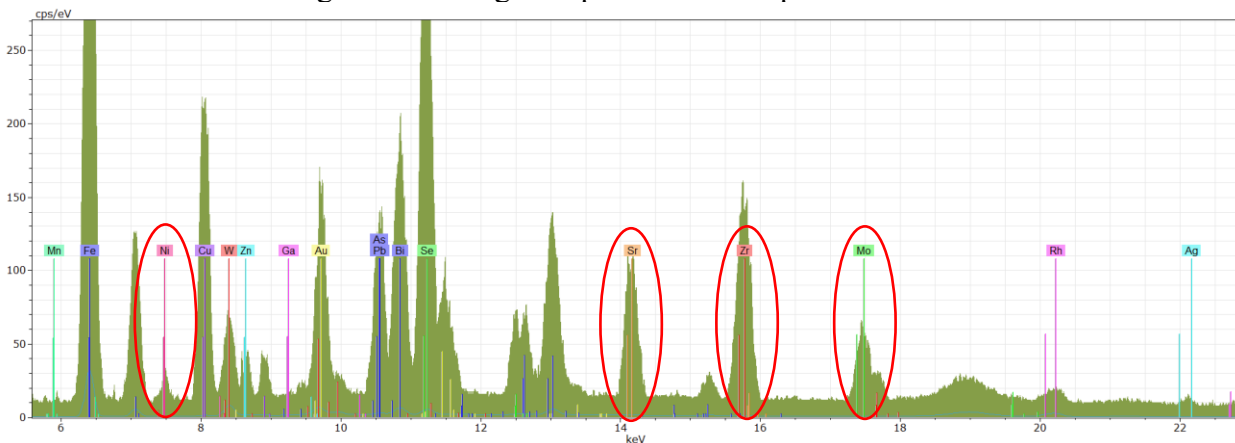


Figure 2.7: Maximum pixel spectrum of sample ROD-340.

2.4. EXAMPLES OF PREVIOUS ORE-FORMING STUDIES USING μ XRF

Using an μ XRF system, Genna et al. (2011) characterized hydrothermal alteration in the subaqueous Noranda-Cap d'Ours felsic volcanogenic massive sulfide complex in Quebec (Canada). They detected two distinct hydrothermal events: i) an early alteration zone consisting of proximal silica and distal chlorite-sericite resulting from the convection of seawater within the dome-flow complex, and ii) a late discordant sericitization event that resulted from the emplacement of quartz- and feldspar-phyric endogenous lobes and is associated with Au mineralization. This technique was successfully applied to map volcanic hydrothermal alteration in a highly fragmented and porous dome-flow complex, demonstrating its potential for understanding volcanogenic massive sulfide-style mineralization.

A scanning μ XRF was used by Potter et al. (2019) to acquire qualitative and quantitative geochemical and mineralogical data and produced elemental maps that provide information on spatial variation and concentration of major, minor, and trace elements, which may not be visually distinguishable but are essential for understanding paragenesis and mineralization.

Barker et al. (2021) used fundamental parameters standardless analysis to quantify μ XRF data. They compared the results with those of standardized wavelength-dispersive spectrometry to show that the fundamental parameters method in general produced high-quality results ($R = 0.98$ – 0.97). They found that the fundamental parameters method overestimated Fe and K abundances but underestimated Mg abundances. Their findings indicate that XRF maps can determine the mineral composition, abundance, and mineralogical textures in fine-grained sedimentary rocks associated with Carlin-type gold deposits. Ore and gangue minerals often occur at fine grain sizes, making it difficult to distinguish them in hand specimens in sedimentary-hosted ore deposits. However, this approach applies to any ore deposit.

Wang et al. (2022) investigated variation in S levels at trace levels along a stalagmite growth axis using benchtop μ XRF. They could detect trace concentrations of sulfur in calcite-rich samples by optimizing the instrument parameters. For the accuracy of trace sulfur quantification analysis, synthetic matrix-matched standards were calibrated with a low detection limit. Analysis of a point-by-point transect of the same sample showed a good correlation with an equivalent wavelength-dispersive XRF analysis. Using sub-annual data to capture seasonal variations, Wang et al. (2022) found that S could be detected in fast-growing stalagmites with narrow laminae of the type usually found at low latitudes.

Chapter 3: Gold-Ag-(Cu-Te-Se-Sn) mineralization, Rodalquilar deposit, Spain

3.1. INTRODUCTION

For this study on applications of a μ XRF instrument, it was hypothesized that an ideal sample to work with at the early stages of the study would contain an abundance of chemical elements, both heavy metals such as those commonly concentrated in a metallic ore deposit (e.g., Cu, Ag, Pb, Zn, Sn, Au, Ba), as well as lighter chemical elements, such as the major elements present in rock-forming and hydrothermal alteration minerals (e.g., Si, Al, K, Ca, Na). The Rodalquilar epithermal Au-Ag deposit in SE Spain presents samples with these characteristics. The Rodalquilar deposit was studied in detail by Arribas et al. (1995) and a summary description of the deposit was published by Hedenquist et al. (1996), from which the following section is borrowed.

3.2. THE RODALQUILAR CALDERA COMPLEX AND AU-AG DEPOSITS

The relatively small but well-exposed Rodalquilar high-sulfidation epithermal Au deposit (10 t Au produced) is located on the Mediterranean coast of southeastern Spain and is the first example in Europe of epithermal mineralization related to a caldera (Fig. 3.1; Arribas, et al., 1995). Ore deposits within the Rodalquilar caldera complex occur within intracaldera ash-flow and ash-fall units and rhyolite domes (Fig. 3.2).

Volcanic rocks in the vicinity of the Rodalquilar deposit range in composition from pyroxene andesite to rhyodacite and in age from about 15 to 7 Ma. The gold-alunite deposits are located within the Rodalquilar caldera complex and are closely associated with an extensive zone (over 25 km²) of argillically and advanced argillically altered rocks (Fig. 3.3).



Figure 3.1: View of the Rodalquilar deposit located in the eastern wall of the Lomilla caldera (arcuate scarp). Gold was extracted from open pits and underground workings in caldera wall.

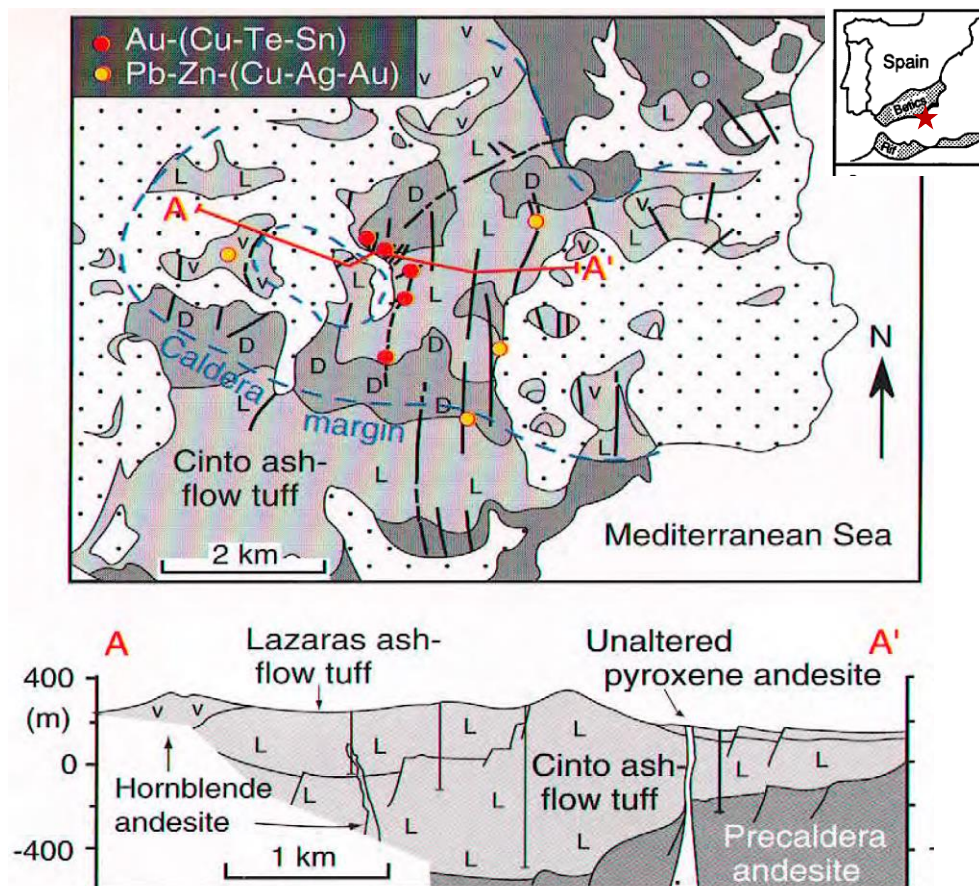


Figure 3.2: (top) Geologic map of the Rodalquilar caldera complex in the Cabo de Gata volcanic field, SE Spain (inset map), showing the margins of the Rodalquilar and Lomilla calderas, major faults, and location of epithermal base metal and Ag-Au deposits. (bottom) Section through the Rodalquilar district (from Arribas et al., 1995, in Hedenquist et al., 1996).

Mineralization consists of low-sulfidation base- metal veins and the economically more important high-sulfidation Au-Ag (Cu-Te-Sn) deposit. The latter is related temporally to andesite porphyry intrusion and is localized preferentially along ring and radial faults in the eastern wall of the nested Lomilla caldera. Advanced argillic alteration with alunite-kaolinite-diaspore-pyrophyllite-zunyite envelopes (Fig. 3.4) the ore zone and extends to 300 m depth, about 200 m below the extent of Au mineralization (Fig. 3.3) Deep drilling shows a gradation to a quartz-sericite-pyrite assemblage which changes laterally to a propylitic alteration.

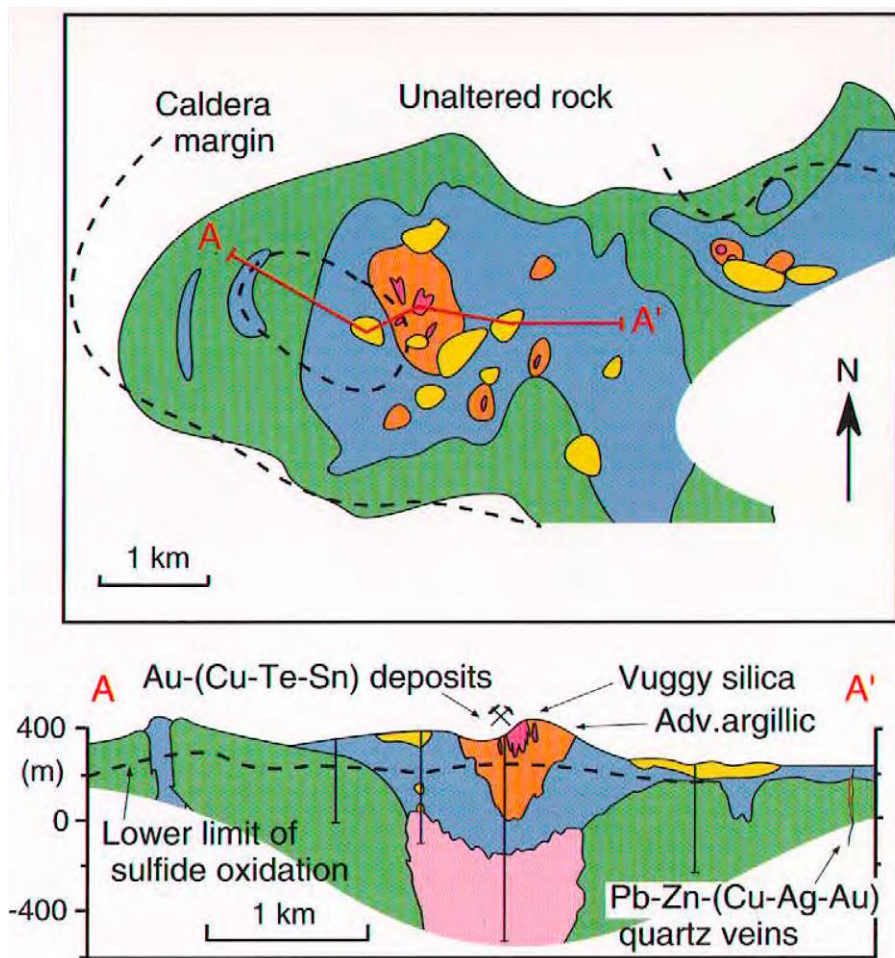


Figure 3.3: (top) Alteration map of the Rodalquilar caldera; (bottom) Section A-A' showing generalized alteration pattern, based on drill hole samples (drill holes shown). The vuggy quartz core that hosts ore has outward and downward halos of advanced argillic and argillic alteration; the argillic alteration pinches out downward at depths >350 m and gives way to quartz-sericite alteration typical of porphyry systems (from Arribas et al., 1995, in Hedenquist et al., 1996).

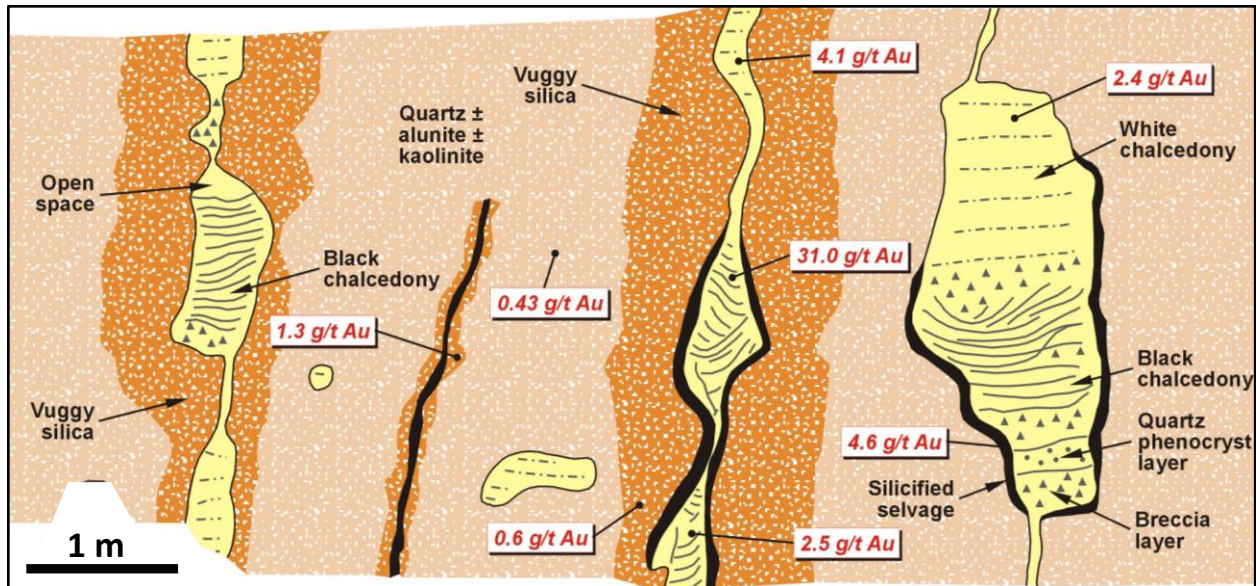


Figure 3.4: Schematic illustration of the relation between wall rock and chalcedonic quartz Au ore filling fractures and open spaces. Early acid wall rock alteration was followed by open space filling by breccia layers and mineralized/barren amorphous silica (Arribas et al., 1995).

Potassium/Ar dating of alunite and sericite indicates an average age of about 10.4 Ma for the mineralization, less than 1.0 M.y. younger than the age of the Rodalquilar caldera (age of precaldra dome = 11.1 Ma; Arribas et al., 1995).

Zones of vuggy quartz are structurally controlled and related spatially to Au mineralization. Hypogene Au ore is hosted by hydrothermal breccias (Fig. 3.5) and horizontally banded black (pyrite-rich) chalcedony which occurs in veins and as open-space fillings (Figs. 3.4 and 3.6) average grade was 2 to 8 g/t Au). Calaverite, native Te, and pyrite are common hypogene minerals, which have been weathered at 3-4 Ma to produce native Au, Fe hydroxides and secondary Te minerals, in addition to a widespread supergene alunite-kaolinite overprint (Fig. 3.3, tan color).

Geochemical studies indicate two hypogene alteration-mineralization stages: acidic wallrock alteration and leaching followed by Au mineralization under less acidic and more reduced conditions. A significant magmatic component was present in the fluid during both stages, with salinities attaining 40 wt% NaCl equiv. at the depth of sericitic alteration (Fig. 3.7).

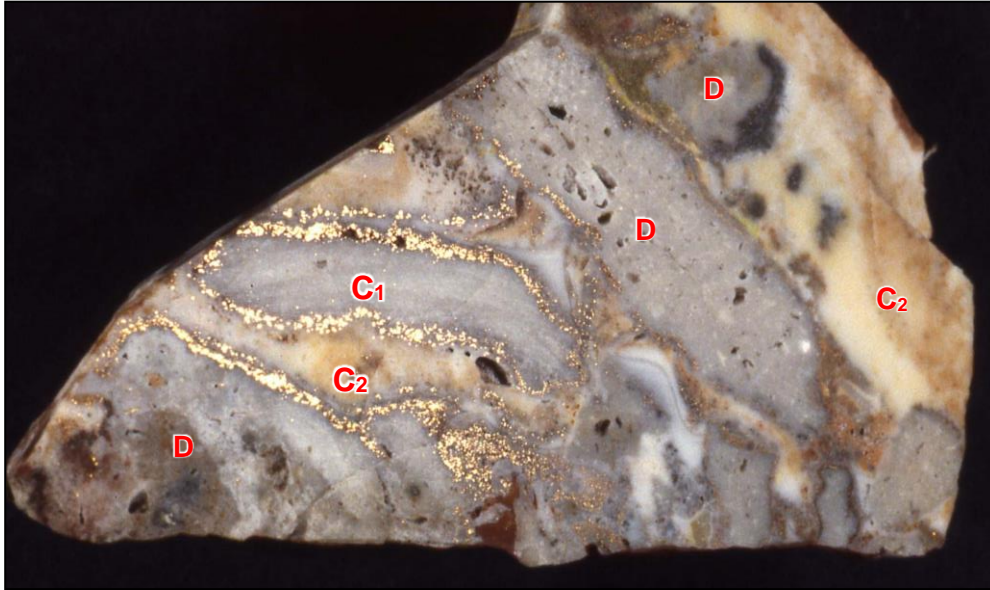


Figure 3.5: Sample of hydrothermal vein breccia consisting of altered (vuggy quartz and advanced argillic) rhyolite (D) and earlier vein clasts (C₁) in a chalcedony matrix (C₂). Hypogene Au occurs as dark calaverite (AuTe₂)-bearing chalcedony.



Figure 3.6: Banded chalcidonic ore at Rodalquilar: fracture filled with Au-bearing black, horizontally banded chalcidonic quartz. Some layers appear light in color due to weathering of sulfides. Average Au grade for the vein is 15 g/t; the Au content of the vuggy silica envelope is 1.3 g/t (Arribas et al. 1995).

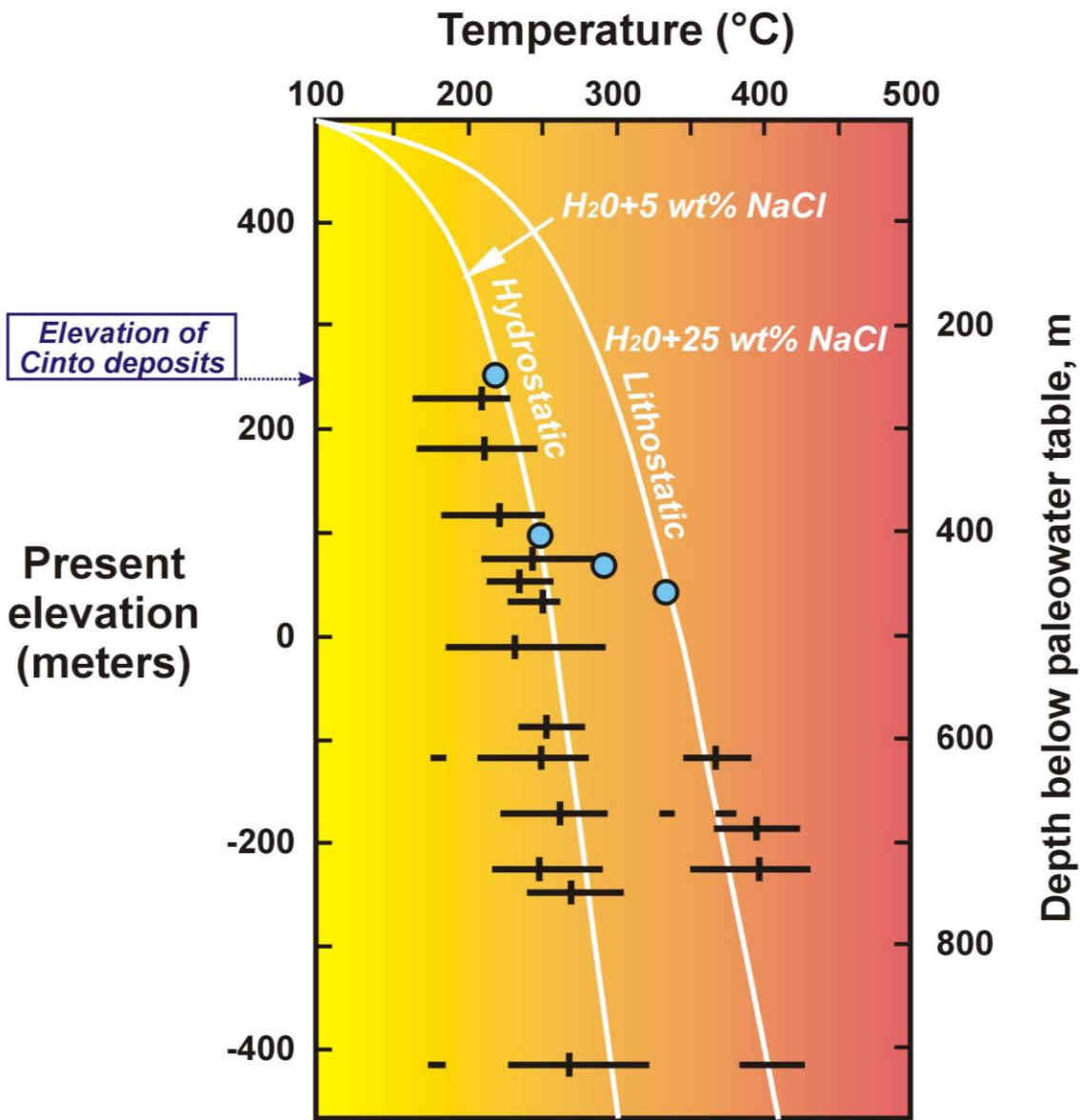


Figure 3.7: Elevation vs. temperature diagram showing range and average of fluid inclusion homogenization temperatures from Rodalquilar (Cinto) high-sulfidation deposit and the S-isotopic fractionation temperatures (circles) for coexisting pyrite-alunite pyrite. Hydrostatic boiling-point curve (for 5 wt% NaCl solution) and lithostatic pressure curve (for 25 wt% NaCl) are fitted to the data, suggesting low-salinity fluids were at hydrostatic pressures, whereas the younger higher temperature, higher salinity fluids (at a given depth) associated with quartz-sericite alteration were at lithostatic pressures, perhaps at paleodepths of only 600m. The present surface is 200-300 m beneath the paleosurface (from Arribas et al., 1995, in Hedenquist et al., 1996).

3.1. SAMPLES AND ORE EVOLUTION

In a 1995 study, Arribas et al. completed a comprehensive identification of the minerals present in the Rodalquilar deposits including their main form of presence (in the ores vs in altered wall rock), likely origin (hypogene vs supergene origin) and abundance (Fig. 3.8). The study also defined a broad evolution for the deposit: from an early stage of acid hydrothermal alteration formed at temperatures of 320 to 250°C from the condensation of acid sulfate-chloride magmatic volatiles, to a base- and precious-metal mineralization stage formed at lower temperature and under less acidic conditions. Based on the presence of banded chalcedonic quartz (Fig. 3.6), which was interpreted as original amorphous silica which recrystallized to quartz, the temperature of the main stage of Au mineralization was interpreted to be <180°C.

Native elements					Oxides				
Gold	✓	R	H and S	V	Goethite	✓	C	S	W
Tellurium	✓	R	H	V	Hematite	✓	C	H and S	V and W
Sulfides, sulfosalts, arsenides, antimonides					Magnetite	✓	S	H	W
Bismuthinite	●	R	H	V	Quartz	✓	C	H	V and W
Bornite	✓	R	H	W*	Rutile	✓	S	H	W
Chalcopyrite	✓	R	H	V and W	Tellurite	●	R	S	V
Cinnabar	●	R	H	V	Carbonates				
Colusite	●	R	H	V	Azurite	✓	R	S	V
Covellite	✓	R	H and S	V	Calcite	✓	R	H	W
Digenite	●	R	S	V and W	Malachite	✓	R	S	V
Emplectite (?)	●	R	H	V	Cerussite	●	R	S	V
Enargite	✓	R	H	V and W	Silicates				
Galena	✓	R	H	V	Adularia	✓	R	H	W
Idaite	○	R	H	W*	Chlorite	✓	C	H	W
Marcasite	○	R	H	W*	Epidote	✓	S	H	W
Pyrite	✓	C	H	V and W	Illite	✓	C	H	W
Pyrrhotite	✓	R	H	V and W	Kaolinite	✓	C	H and S	W
Sphalerite	✓	R	H	V and W	Smectite	✓	C	H and S	W
Tennantite	✓	R	H	V and W*	Muscovite	✓	S	H	W
Tetrahedrite	●	R	H	V	Pyrophyllite	✓	R	H	W
Iodide					Zunyite	●	S	H	W
Iodargyrite	●	R	H?	V	Sulfates, phosphates				
Tellurides, tellurates, tellurites, selenides					Alunite	✓	C	H and S	V and W
Calaverite	✓	R	H	V	Barite	✓	R	H	V
Emmonsite	✓	R	S	V	Crandallite	●	R	H	W
Blakeite (?)	●	R	S	V	Florencite	●	R	H	W
Rodalquilarite	✓	R	S	V	Gypsum	✓	R	S	V and W
Naumannite	●	R	H	V	Jarosite	✓	S	S	W
Oxides					Svanbergite	●	R	H	W
Cassiterite	●	R	H	V	Woodhouseite	●	R	H	W
Diaspore	✓	S	H	W	Arsenate				
					Scorodite	✓	R	S	V

Symbols: status: ✓ = previously reported, confirmed in present study, ○ = previously reported, unconfirmed in present study, ● = newly reported in present study; abundance: C = common, S = sparse; R = rare; origin: H = hypogene, S = supergene; presence: V = found chiefly in lodes, W = found chiefly in altered wall-rock (* as inclusions in pyrite)

Figure 3.8: Minerals present in the Rodalquilar deposit (Arribas et al. 1995). While many minerals were identified, the details of the paragenetic sequence of the mineralization were incompletely defined.

A representative sample from the 340 hydrothermal breccia vein within the Cinto ore body in the Rodalquilar deposit was selected for study (Fig. 3.9). The sample contains fragments of altered wall rock that show variable degrees of silicification, more intense in the margins of the lithic fragments inside the breccia. The open space between lithic fragments is filled by a hydrothermal sediment that has geopetal structure (Fig. 3.9, arrow pointing up) of amorphous silica precipitating out of solution.

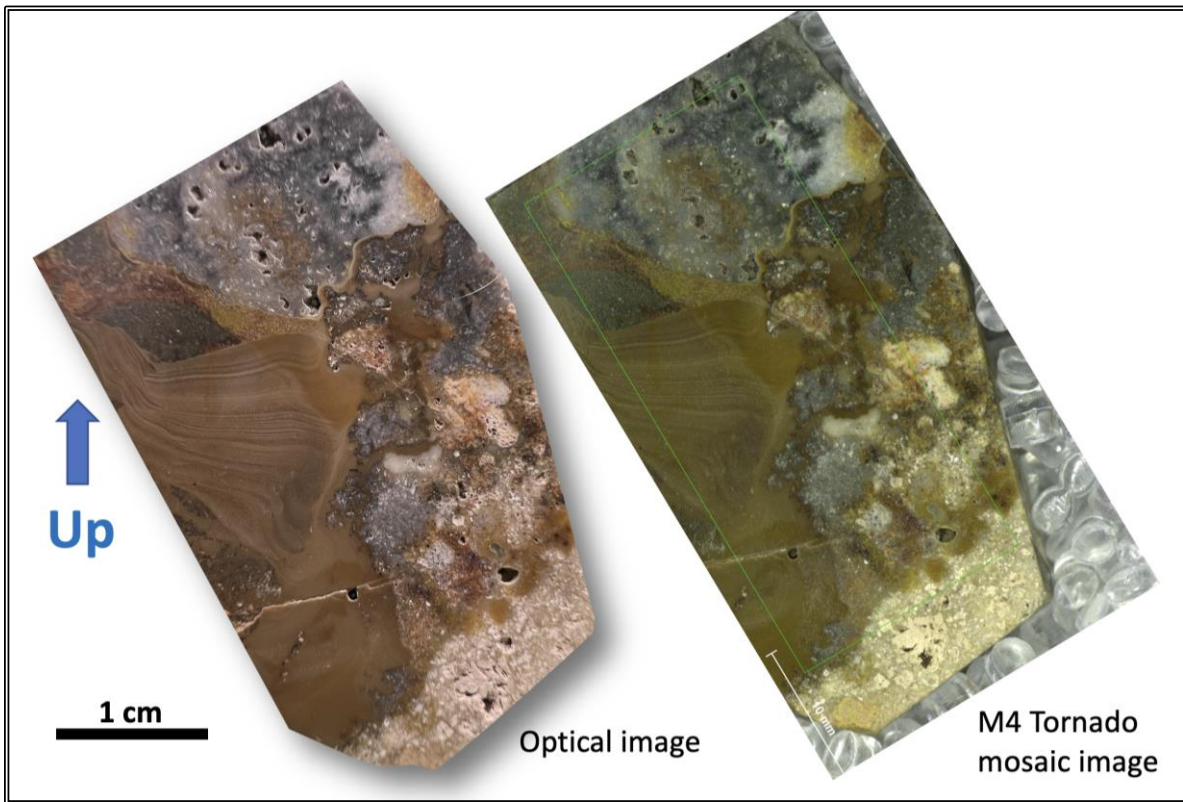


Figure 3.9: Sample selected for study from the Rodalquilar Cinto deposit (ROD-1). Image on the right is the mosaic image from the M4 Tornado; green outline indicates area analyzed.

The spectrum collected from Sample ROD-1 (Figs. 3.10-11) and the corresponding elemental maps are shown in Figs. 3.12-15, grouped by the evolution of the mineralization in four stages. Fig. 3.16 shows two composite elemental maps that illustrate the chemical evolution, and Fig. 3.17 summarizes the evolution of the 340 breccia from white mica alteration of the wall rock

(Stage 1) through three stages of hydrothermal alteration of decreasing temperature and complex chemistry (Stage 2-4). These stages are interpreted to be the result of individual pulses of magmatic-hydrothermal fluid emanating from crystallizing magma at depth.



Figure 3.10: Screen image of the Bruker M4 Tornado showing spectrum collected from sample ROD-1 (green outline in Fig. 3.9, right)

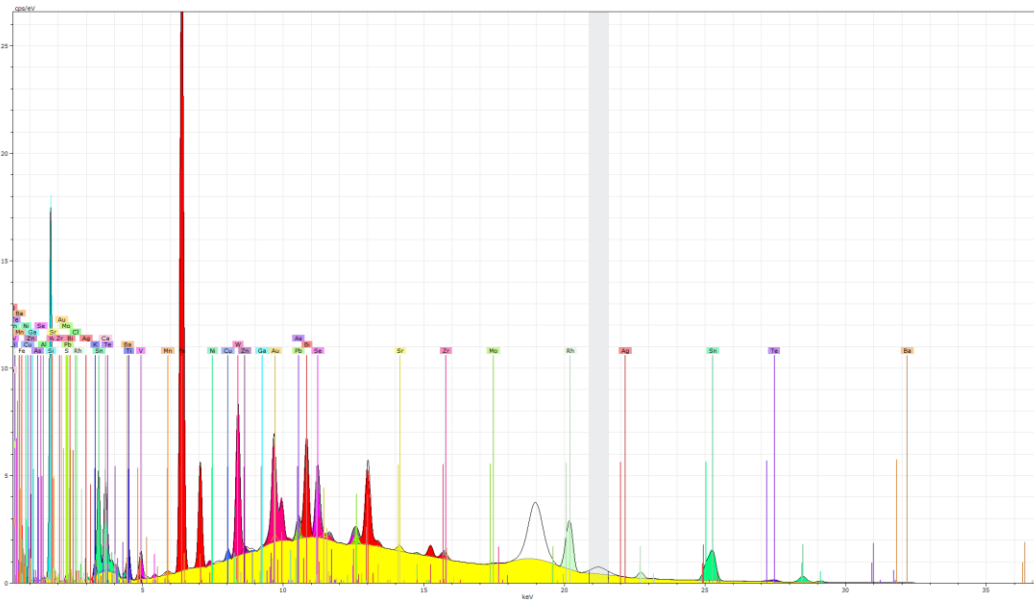


Figure 3.11: Complete spectrum with peaks and background identified.

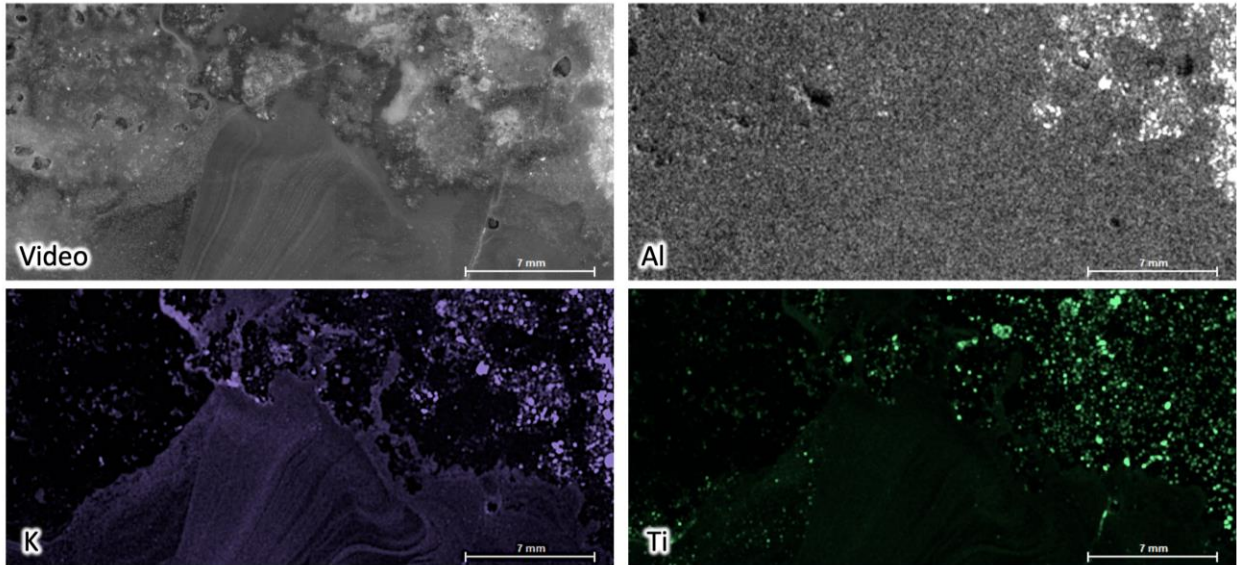


Figure 3.12: X-ray maps of elements corresponding to Stage 1 of wall rock alteration.

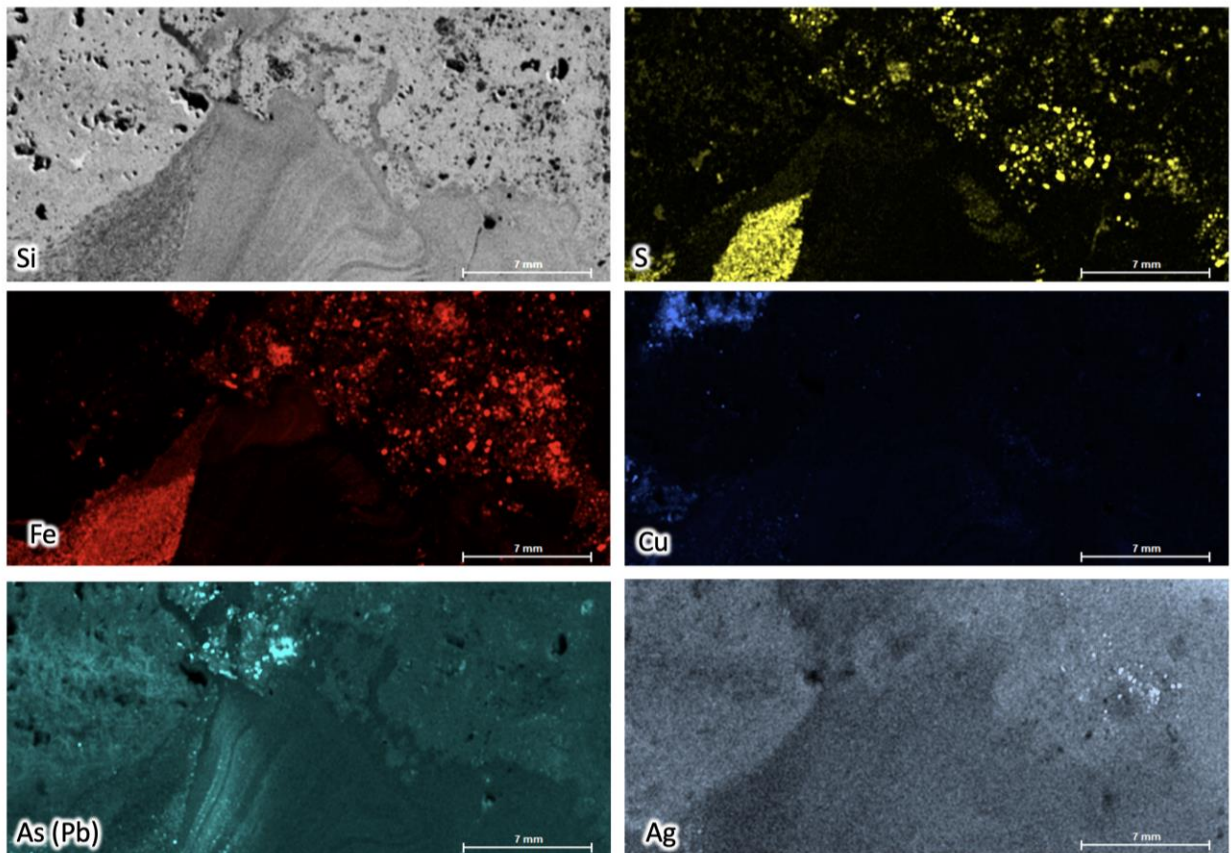


Figure 3.13: X-ray maps of elements corresponding to Stg. 2 of wall rock alteration, with strong silicification, pyrite and low-grade Zn-Cu-Ag-Au mineralization (ROD-1).

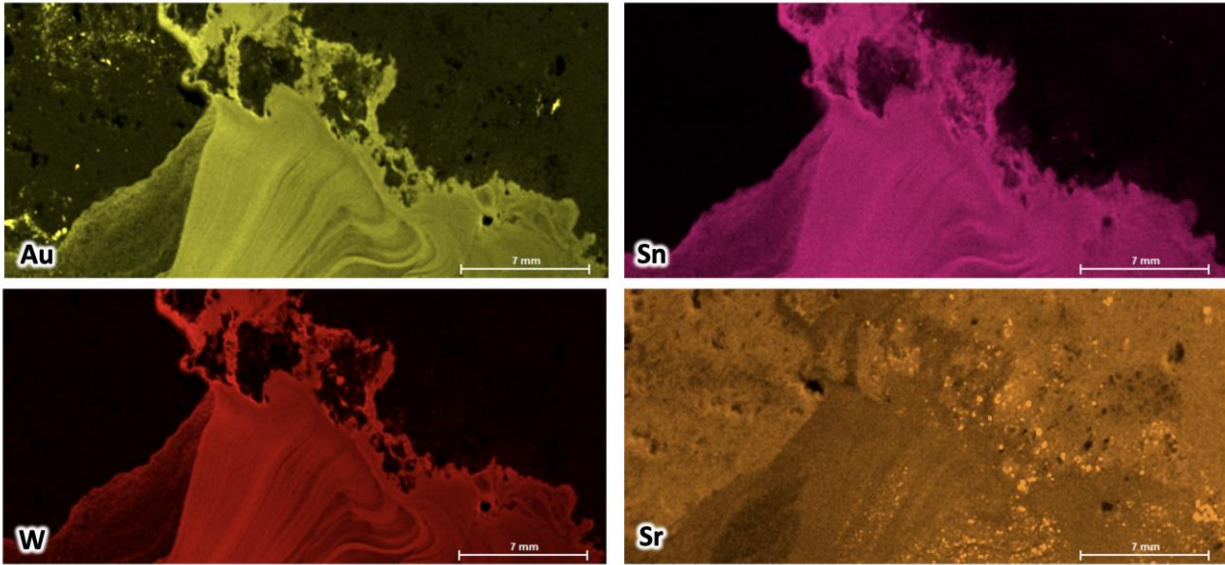


Figure 3.14: X-ray maps of elements corresponding to Stage 3, fine grained amorphous silica cavity fill with high-grade Au and Sn-W. The presence of Sr is not well understood (ROD-1).

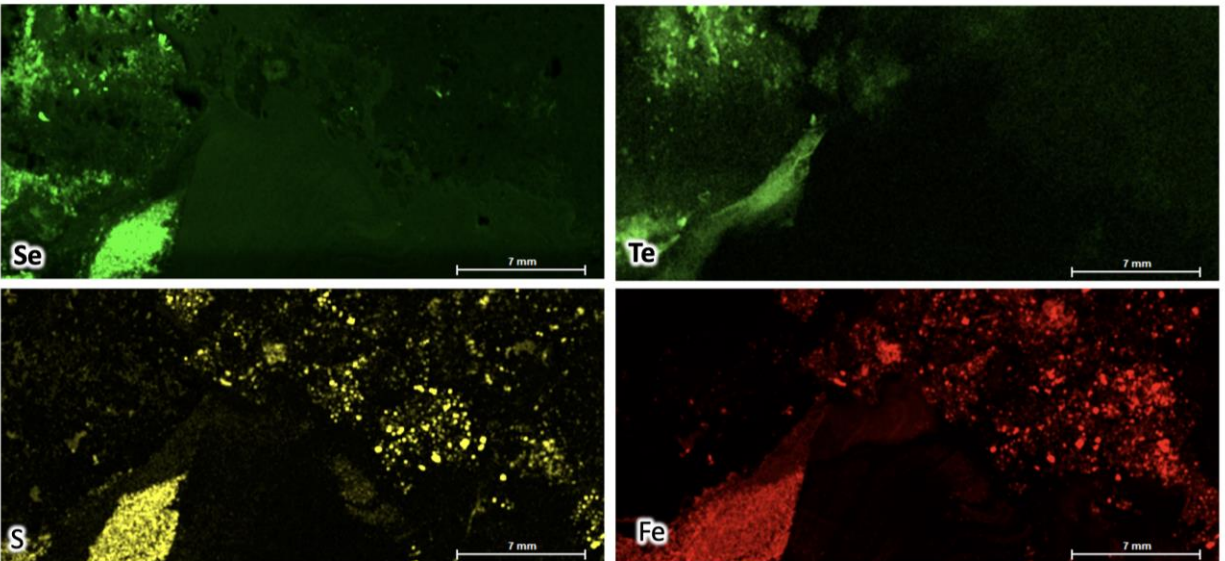


Figure 3.15: X-ray maps of elements corresponding to Stage 4, Se following Au-Sn-W, followed by Te. Pyrite (FeS_2) is present both in Stage 2 and Stage 4 (ROD-1).

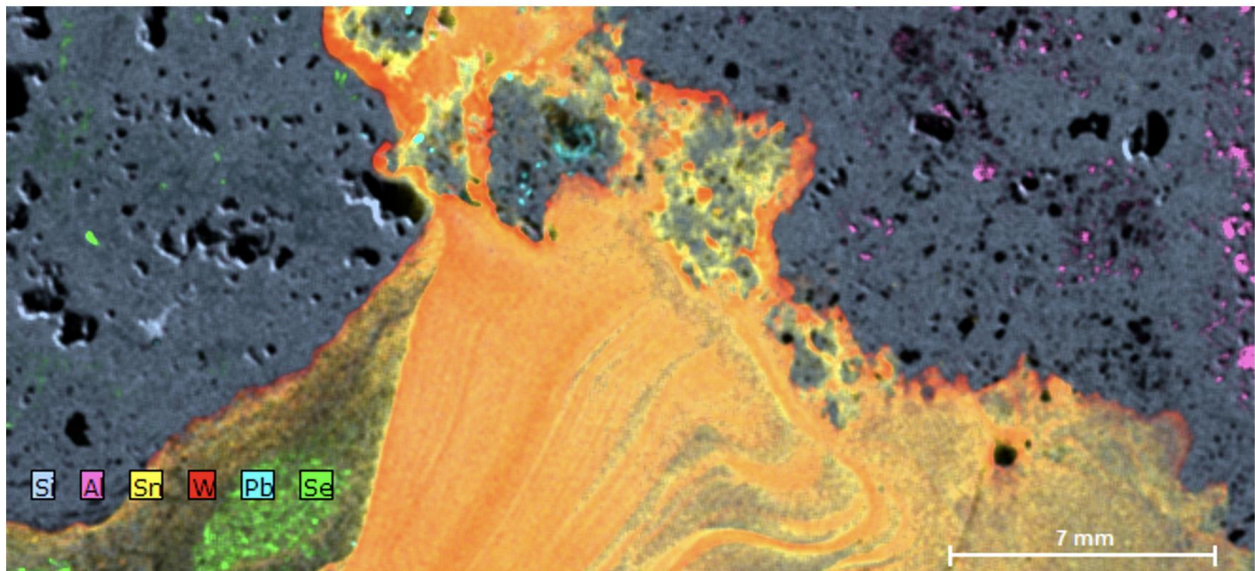
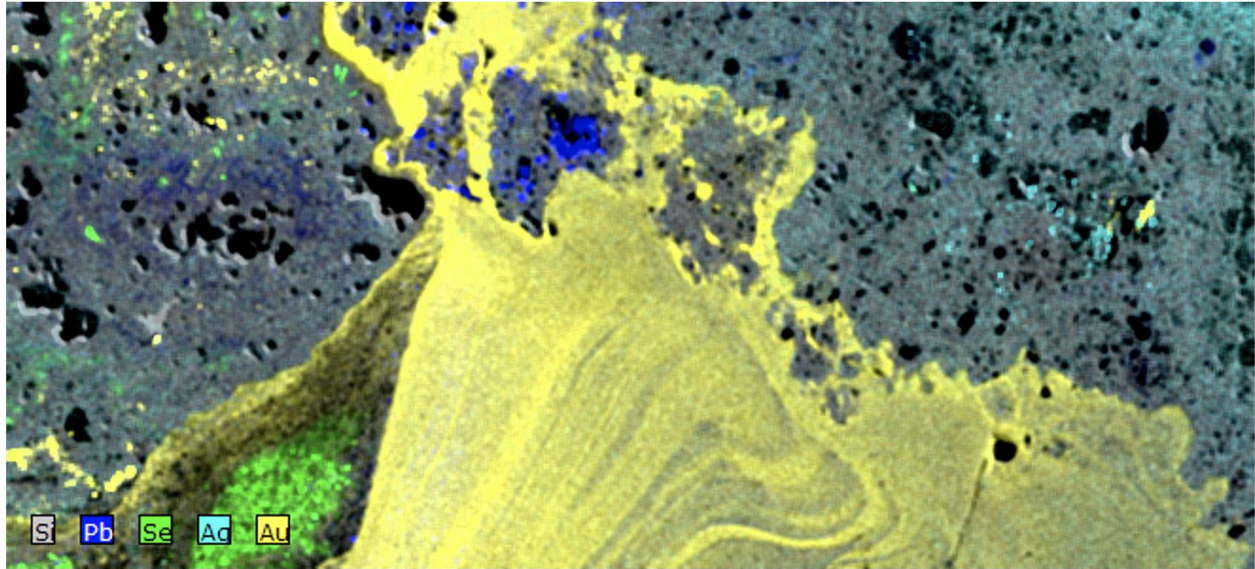


Figure 3.16: Composite elemental maps showing two selections of elements that characterize the four stages of mineralization in sample ROD-1. Top image: Si (light gray), Pb (dark blue), Se (bright green), Ag (cyan), Au (yellow); bottom image: Si (light gray), Al (pink), Sn (light yellow), W (red), Pb (cyan), Se (bright green)

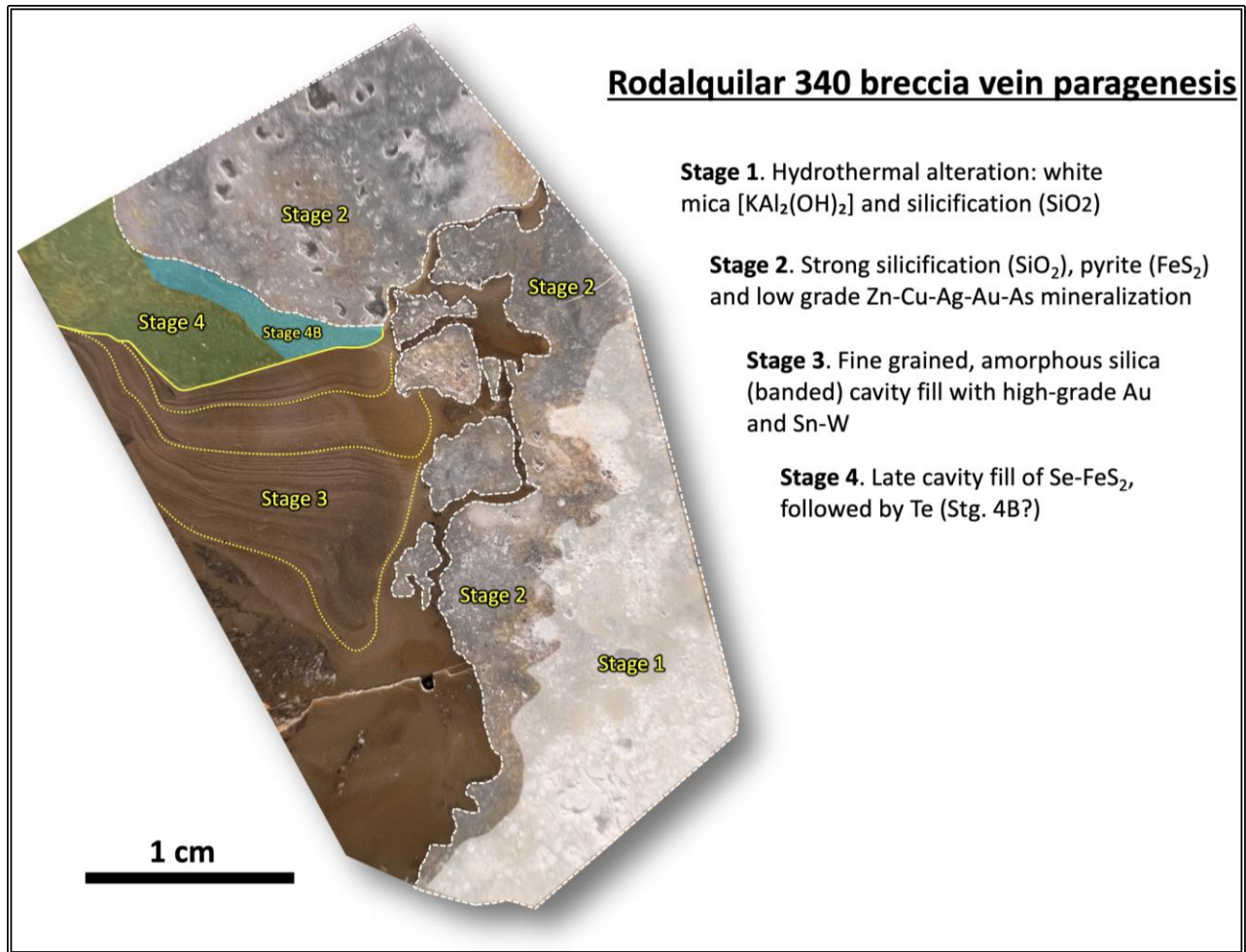


Figure 3.17: The entire chemical and mineralogical evolution of the high grade 340 hydrothermal breccia at Rodalquilar identified in a single sample with the help of the μ XRF.

Chapter 4: Sediment-hosted Cu-Ag mineralization, Khoemacau Zone 5, Botswana

4.1 INTRODUCTION

The Kalahari Copperbelt in Botswana (Fig. 4.1, inset) has been studied extensively to understand its geology and origin, including the regional- to deposit-scale structural setting (e.g., Morgan, 2013; Lehmann et al., 2015; Hall et al., 2018b), depositional environment and geochronology (e.g., Modie, 1996; Hall et al., 2021), and provenance and distribution of metals (e.g., Schwartz et al., 1995; Modie et al., 2000; Hall et al., 2018a). All studies agree that litho-structural control, permeability, metal and S sources, and a reductant (in-situ or mobile) are crucial elements for the precipitation of the Cu-Ag ores. Additionally, Cu-Ag mineralization has been shown to occur along regional fold limbs and hinges, making the structural setting a key feature in the identification of ore mineralization traps. However, metallogenic models proposed for Cu-Ag mineralization in the Kalahari Copperbelt remain controversial.

For the Kalahari Copperbelt a variety of genetic scenarios exist, including syngenetic-diagenetic models (Ruxton, 1986; Schwartz et al., 1996), epigenetic models (Sillitoe et al., 2010; Hall et al., 2018b, 2021), and two-stage models requiring overprinting and remobilization of diagenetic precursors or early hydrothermal base metal sulfides (Borg and Maiden, 1989; Borg, 1988, 1995; Walraven and Borg, 1992). Documenting detailed mineral parageneses at the deposit scale is challenging, contributing to the disagreement between these models. According to Hall et al. (2021), the Kalahari Copperbelt in Botswana contains two discrete mineralizing events that date back to the Neoproterozoic (more than 400 million years ago).

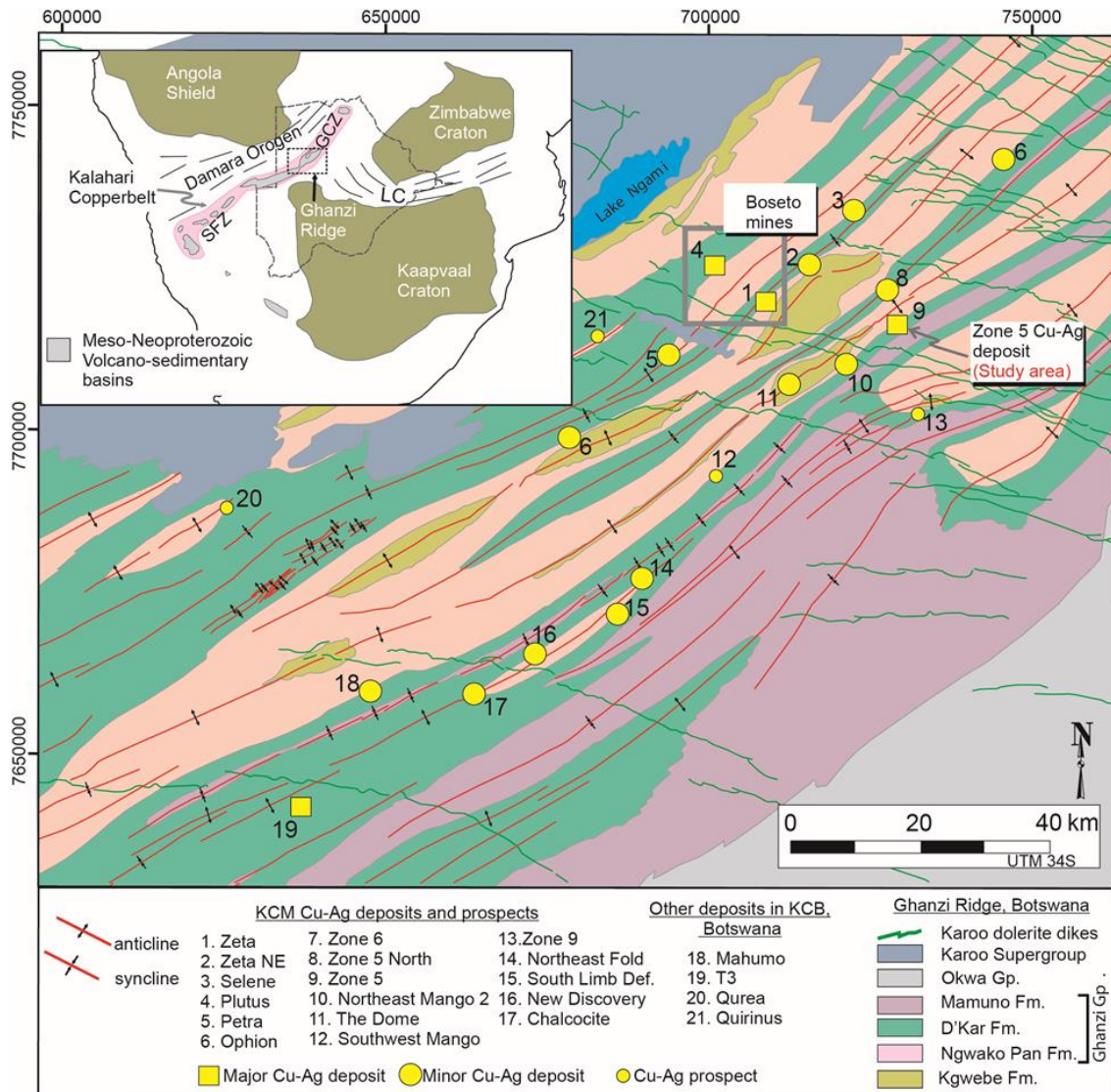


Figure 4.1: Generalized geologic map and Cu-Ag deposits of the Ghanzi Ridge, Kalahari Copperbelt in Botswana. Geology is inferred from known geology and geophysics. The insert is a sub-continental Precambrian geology map of southern Africa showing the location of the Kalahari Copperbelt within which the focus (Ghanzi Ridge). The blue dotted line represents an arbitrary outline of the Kalahari Craton (after Keeditse et al., 2022).

The Khoemacau Zone 5 deposit is the third Cu mine in the Kalahari Copperbelt after Klein Aub in Namibia and Boseto in Botswana (Fig. 4.1). The Zone 5 deposit is located 35 km southeast of Boseto and contains 91 million tonnes (Mt) with 2 percent (%) Cu and 21 grams per tonne (g/t) Ag resources. A soil anomaly led to the discovery of the deposit in 2012. Zone 5 is located on a regional-scale anticline limb beneath 40 m of a sedimentary cover of Kalahari Sands (Fig.4.1).

Here, we examine the distribution and textural characteristics of the sulfide mineralization in drill-core samples on a submillimeter scale from the Zone 5 Cu-Ag deposit to better understand the origin of Cu mineralization (diagenetic vs. epigenetic) as well as to find the department of Ag mineralization.

4.2. GEOLOGIC SETTING

The Kalahari Copperbelt is in the Neoproterozoic Damara fold-and-thrust belt (Schwartz et al., 1995; Hall et al., 2018) at the northwestern margin of the Kalahari Craton (Maiden & Borg, 2011; Lehmann et al., 2015). The Kalahari Copperbelt consists of a series of sedimentary rock-hosted Cu-Ag deposits extending intermittently from Namibia to Botswana (Fig. 8) and geophysically connected with NE-trending volcanic-sedimentary basins that are 1,000 km long and 250 km wide (Lehmann et al., 2015). The Copperbelt descriptor was previously attributed to stratabound and structurally controlled Cu-Ag deposits deposited within rift-related volcano-sedimentary basins (e.g., Borg and Maiden, 1989; Schwartz et al., 1996). The fold belt is called the Ghanzi-Chobe Zone in Botswana and the Southern Foreland Zone (SFZ) in Namibia (Fig. 8; Lehmann et al., 2015).

The geologic column in the Ghanzi-Chobe Zone starts with evidence of bimodal magmatism at 1106–1085 Ma (Fig. 4.2) accompanied by an inversion period at 600–480 Ma (Schwartz et al., 1995, Modie, 1996; Gray et al., 2008). A Pan-African Damara orogenesis led to the current structural configuration of the Kalahari Copperbelt, which is characterized by a steeply dipping axial plane and upright to slightly inclined fold systems (Fig. 4.1). Following regional folding, the rocks metamorphosed into lower greenschist facies (muscovite-chlorite-epidote-clinozoisite- calcite-rutile), locally approaching amphibolite facies (Carney et al., 1994; Schwartz

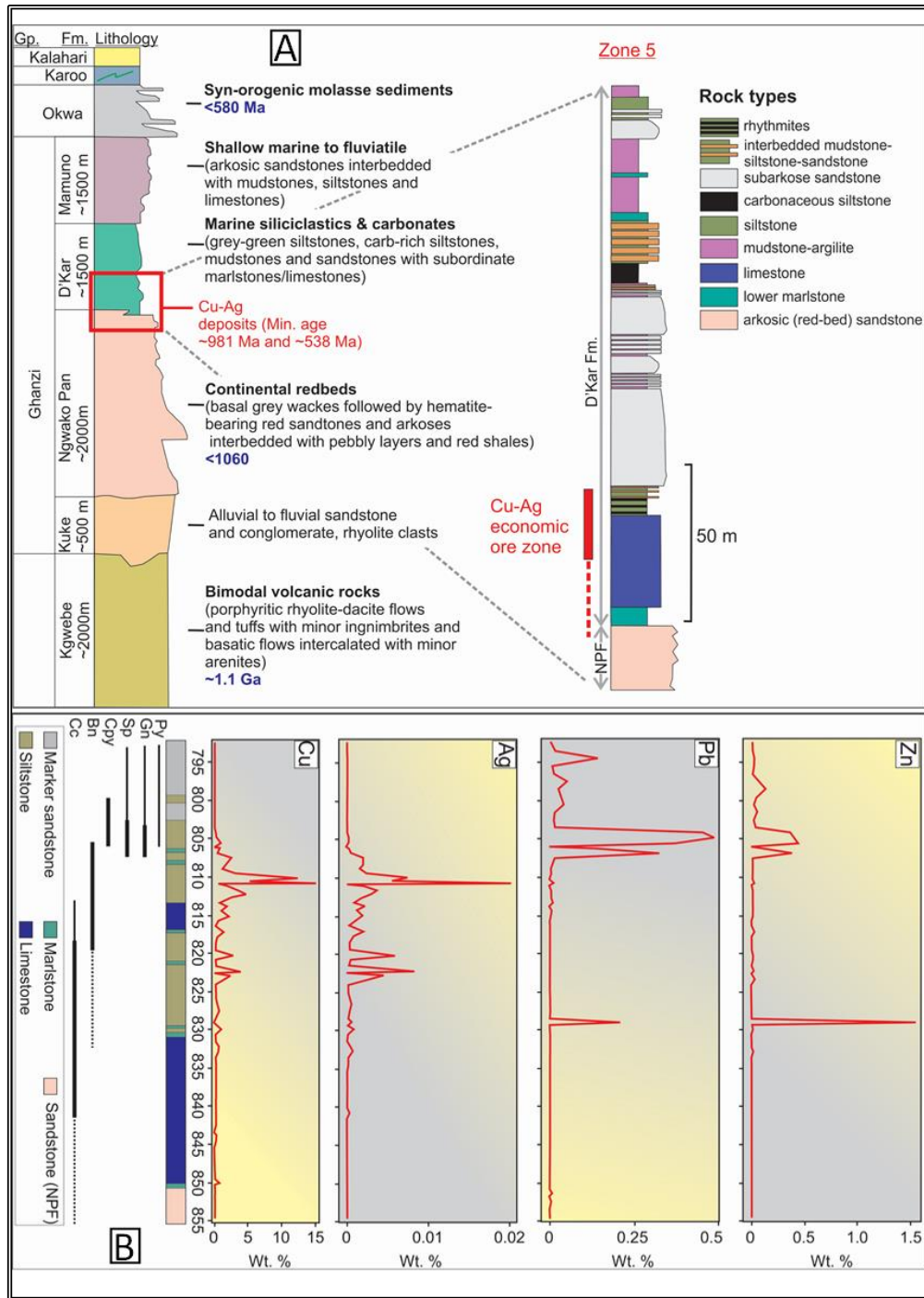


Figure 4.2: (A) Left image shows the schematic lithostratigraphy of the Ghanzi-Chobe zone illustrating lithologic descriptions and ages of the basal volcanic suite and the overlying Ghanzi group as well as mineralization ages. (A) Right image shows the stratigraphic column of Zone 5 with its distinctive units and ore interval. (B) Sample assay results from the drill core section that represented the Zone 5 ore interval and lithologies and mineral abundances. Bn, bornite; Cc, chalcocite; Cpy, chalcopyrite; Sp, sphalerite (after Keeditse et al., 2022).

et al., 1995; Lehmann et al., 2015). It is unclear when metamorphism occurred in the Ghanzi-Chobe Zone. According to Ahrendt et al., 1978; Gray et al., 2008; Miller, 2008, the Damara belt of Namibia experienced peak metamorphism at ~530 Ma, which is close in age to the minimum age of mineralization (Fig. 4.2).

4.3 COPPER-SILVER DEPOSITS OF KHOEMACAU DISTRICT

Numerous researchers have described the Cu-Ag deposits of the Ghanzi-Chobe Zone as structurally controlled, stratabound deposits (e.g., Schwartz et al., 1996; Kelepile et al., 2017, 2020). Additionally, Piestrynski et al. (2015) found that the Neoproterozoic Ghanzi Group of the Ghanzi-Chobe Zone could host precious metals mineralization, like those in other sections of the Kalahari Copperbelt (Kampunzu et al., 1998; Sillitoe et al., 2010).

As shown in Figure 4.2, the lowermost carbonate-siltstone package of the D'Kar Formation hosts most of the metal deposits, which are unconformably overlain by hematite-bearing red sandstone. Mineral zones are characterized by vertical mineralization and ore body thickness between 10 and 20 meters (Hall et al., 2018b). There are several styles of Cu-Ag mineralization within the Ghanzi-Chobe Zone, including dissemination, aggregates along bedding/foliation planes, coarser sulfides within quartz-carbonate veins, and cleavage-controlled mineralization. Hall et al. (2018b) identified regional-to-deposit-scale variations in sedimentary facies and stacking patterns for the lowermost D'Kar Formation, which hosts most of the Cu-Ag mineralization.

It has been proposed by various authors that the deposits in the Khoemacau district and the Kalahari Copperbelt may have two origins: a) Diagenetic, characterized chiefly by fine-grained framboidal pyrite as well as minor ore minerals (Fig. 4.3) and (b) Hydrothermal, characterized by main stage of Cu-Ag mineralization. As for the source of Cu, two lithologic horizons have been

proposed: a) the red bed sandstone of the Ngwako Pan Formation, which forms the footwall of mineralization; b) basaltic rocks in the Kgwebe Formation and Umkondo Igneous Province located south of the KCB. The main aim of our study is to find evidence in support of the much older (~1000-900 Ma) diagenetic origin vs the younger (~550-480 Ma) hydrothermal orogenic origin.

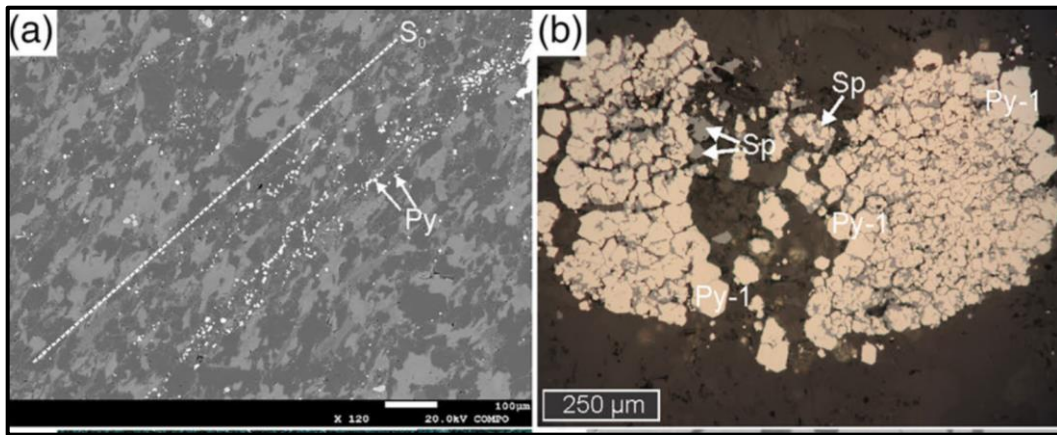


Figure 4.3: Photomicrographs of diagenetic pyrite and associated sulfides at Khoemacau. (a) Backscattered electron image of fine-grained spheroidal-subhedral pyrite concentrated along laminations. (b) Framboidal pyrite coated by sphalerite (Keeditse et al., 2022).

4.4. ANALYTICAL PARAMETERS

A semi-quantitative and modal analysis of Khoemacau samples is demonstrated using two-quarter drill core samples. The samples are highly mineralized quartz-calcite-chalcocite-bornite-hematite samples containing 17% Cu and 168 ppm Ag.

The samples were scanned by a single scan using beam conditions of 50 kV and 600 μA and analytical conditions, as shown in Table 4.1. A multi-element map showing Si, K, Ca, Al, Cu, and Mn makes it easy to identify the different mineral phases and their distribution within the sample. A selection of map areas (Fig. 4.4) and a quantification of the resulting spectra allowed semi-quantitative geochemical data to be determined. Silver was not visible with the naked eye in sample HA 715D-04, but its chemical signature was detected using the maximum pixel spectrum software tool.

Table 4.1: Analytical conditions for the Khoemacau Zone 5 deposit.

Sample ID	Pixel Spacing	Total Pixels	Dwell time measured	Detectors	Map time
HD-1050D	50 μm	844,552	35ms	1SDD	~11hrs
HA-715D-04	30 μm	1,018,920	35ms	1SDD	~12hrs
HA-1058D-04	50 μm	1,050,280	35ms	1SDD	~11hrs
HA_967D-01	50 μm	1,255,634	35ms	1SDD	~13hrs
HA_1015b-03	50 μm	708,724	35ms	1SDD	~8hrs

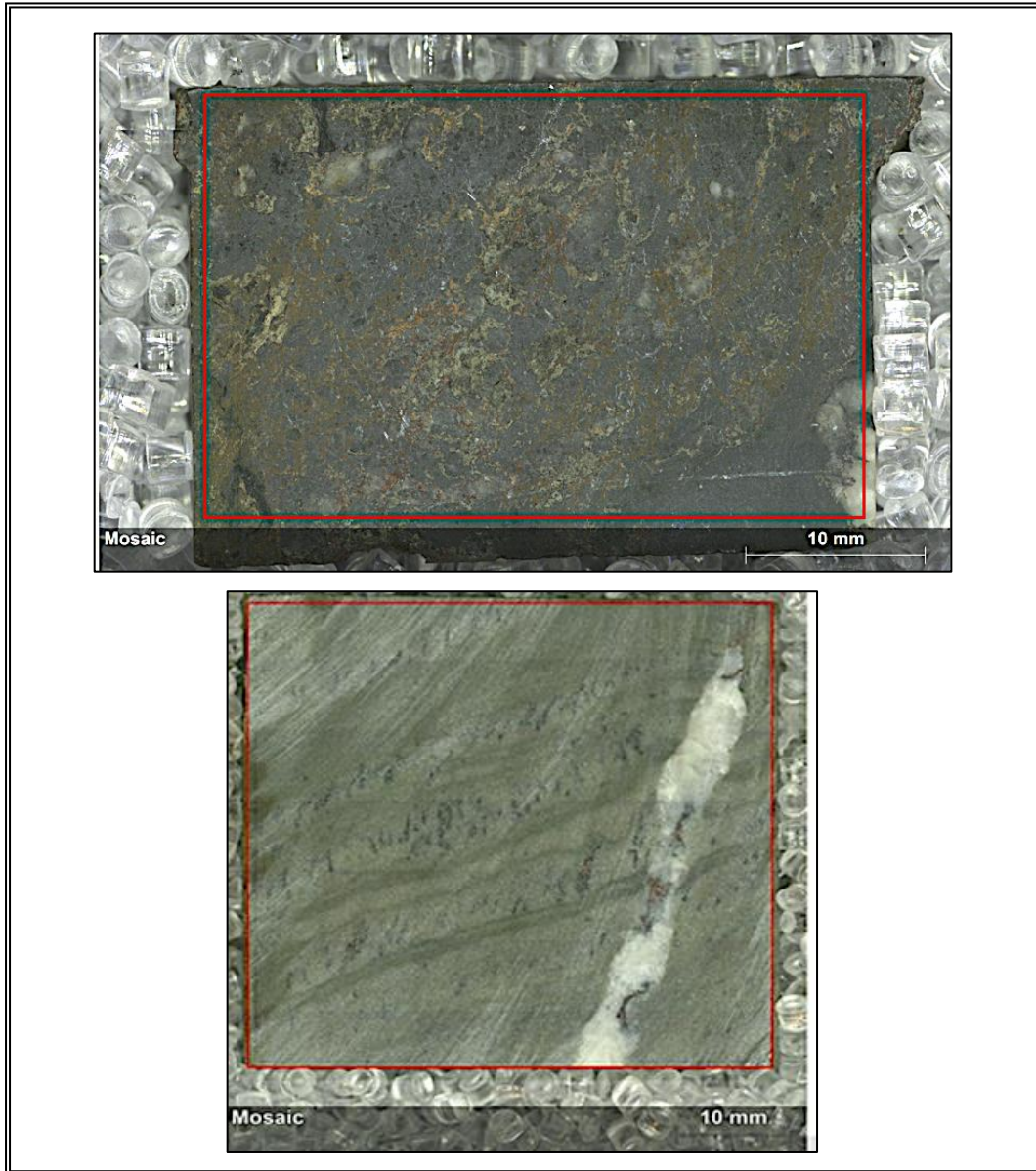


Figure 4.4: Drill core samples are cut, without polishing, with minimal sample preparation. The red rectangles show the mapped areas (bottom, sample HD-1050D).

4.5. RESULTS

To obtain elemental maps, we spatially mapped a series of drill core samples (Figs. 4.4 and 4.5) for chemical and mineral distributions. The elemental maps for Si, Ca, K, Mn, S, Fe, Cu, and Al obtained on Sample HD-1050D (Fig. 4.6) reveal a clear textural relationship and shows that the veins have been emplaced along and subparallel to the metamorphic cleavage. These relationships suggest a hydrothermal syn-cleavage (orogenic) timing of the vein formation and Cu mineralization. The cleavage is best-developed adjacent to the veins due to ongoing deformation and strain accumulation at the vein margins. This indicates that deformation outlasted vein emplacement. The vein is interpreted as syn-tectonic to the fold- and cleavage-forming event.

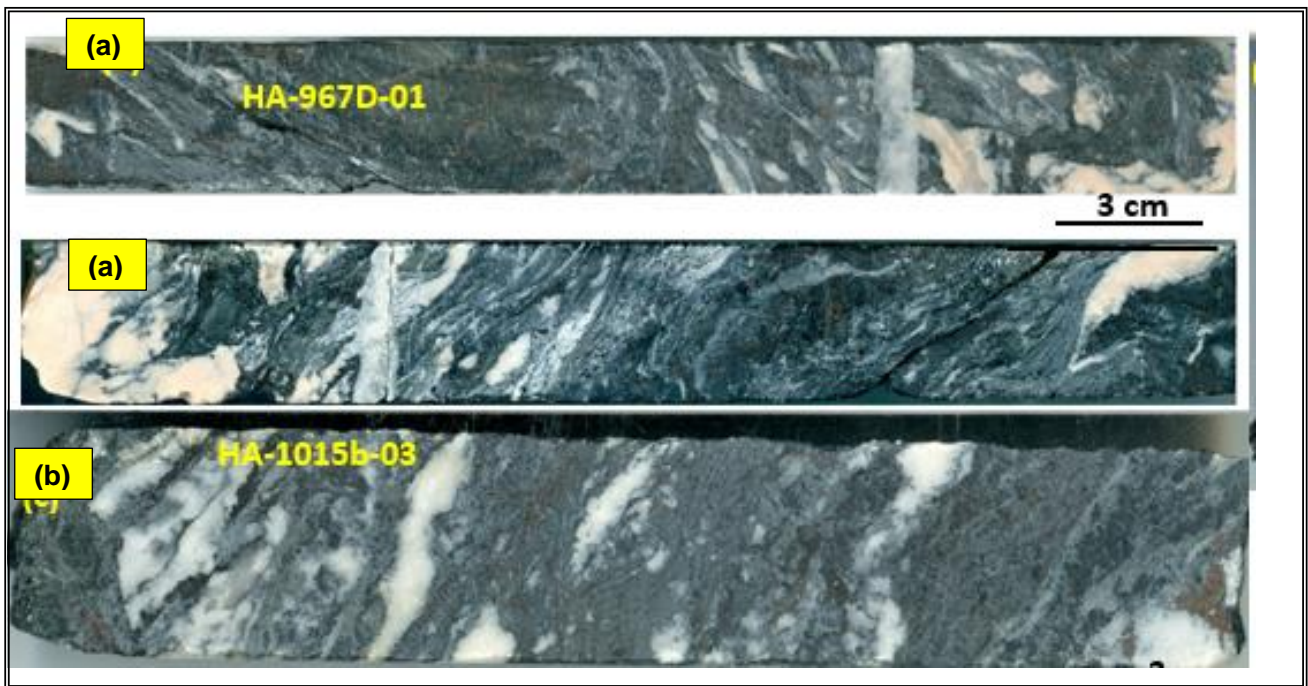


Figure 4.5: Photographs of the drill core samples from Zone 5 deposit, including: (a) HA-967D-01 (both sides): strongly sheared quartz-calcite-bornite-chalcocite vein at 7.2 % Cu; 68 ppm Ag. Veins associated with the ore are boudinaged because of shearing. (b) HA-1015b-03: boudinaged quartz-calcite-bornite-chalcocite vein at 15% Cu; 249 ppm Ag (Keeditse et al., 2022)

A combined map of K, Al, and Si relative derived concentrations in the same sample (Fig. 4.7) also reveals a sericite concentration in the wall rock, with more silicification in the sample's upper part (closer to the fracture, brighter green) and the vein is a calcite-manganese (Ca-Mn) with minor quartz (Si). The cleavage fabric displays two distinct geometries: a penetrative cleavage sub-parallel to the bedding and a crenulation cleavage at an angle to the bedding (Fig. 4.7).

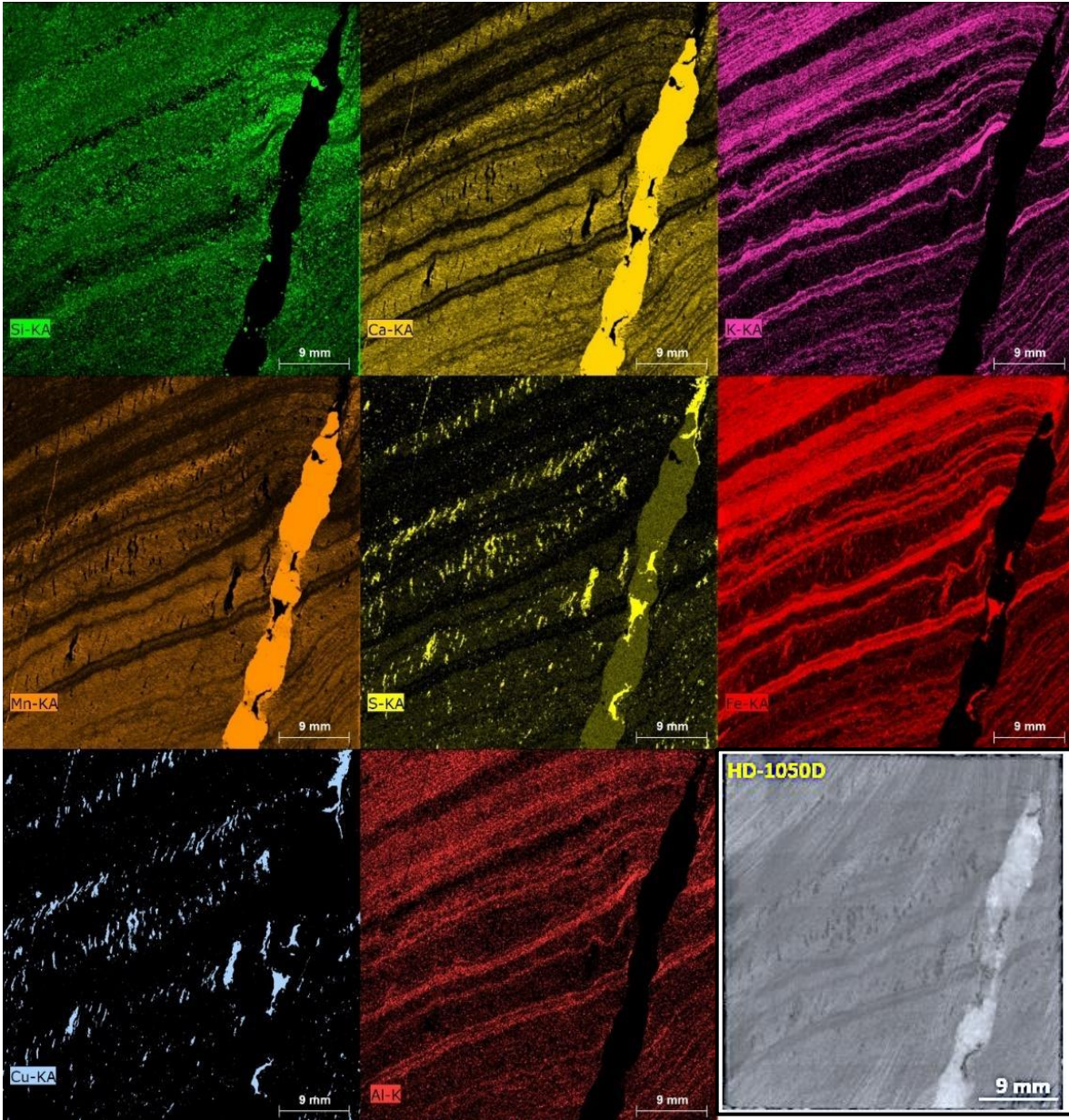


Figure 4.6: Micro-X-ray fluorescence image of sample HD-1050D showing the spatial distribution of single element maps of Si, Ca, K, Mn, S, Fe, Cu, and Al.

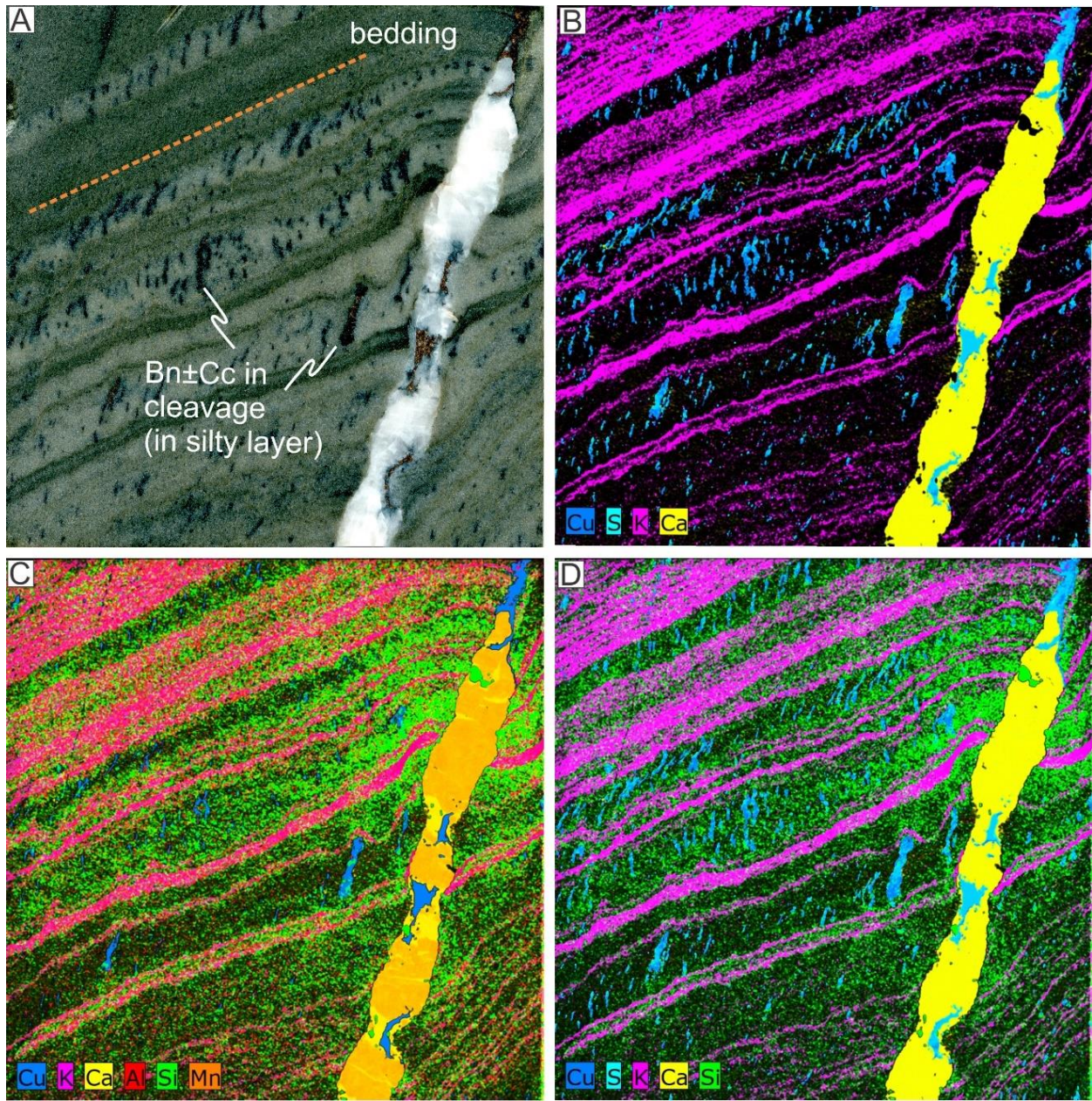


Figure 4.7: (A) Photograph of drill core of sample HD-1050D showing bedding parallel and crenulation cleavage-controlled mineralization. (B, C, D) Show the spatial distribution of Cu, K, Ca, Al, Si, Mn, and sulfide mineralization (bornite, chalcocite, chalcopyrite) along crenulation cleavages and in carbonate veins. Green mica layers are distinguished by their K and Al content (red and pink in B-D). Silicification (precipitation of hydrothermal quartz; bright green in C and D) is observed emanating from the vein that was later filled by rhodochrosite and calcite

Typically, Cu ore lenticles found along crenulation cleavages occur in silty/sandy layers of the host rock, indicating that mineralization is controlled by the porosity and permeability of the host rock. Additionally, sulfide mineralization can be observed in crenulation cleavages as well as in carbonate veins (bornite, chalcocite, chalcopyrite). As evidence of mineralization, Figure 4.8 shows the spectrum of sulfide mineralization.

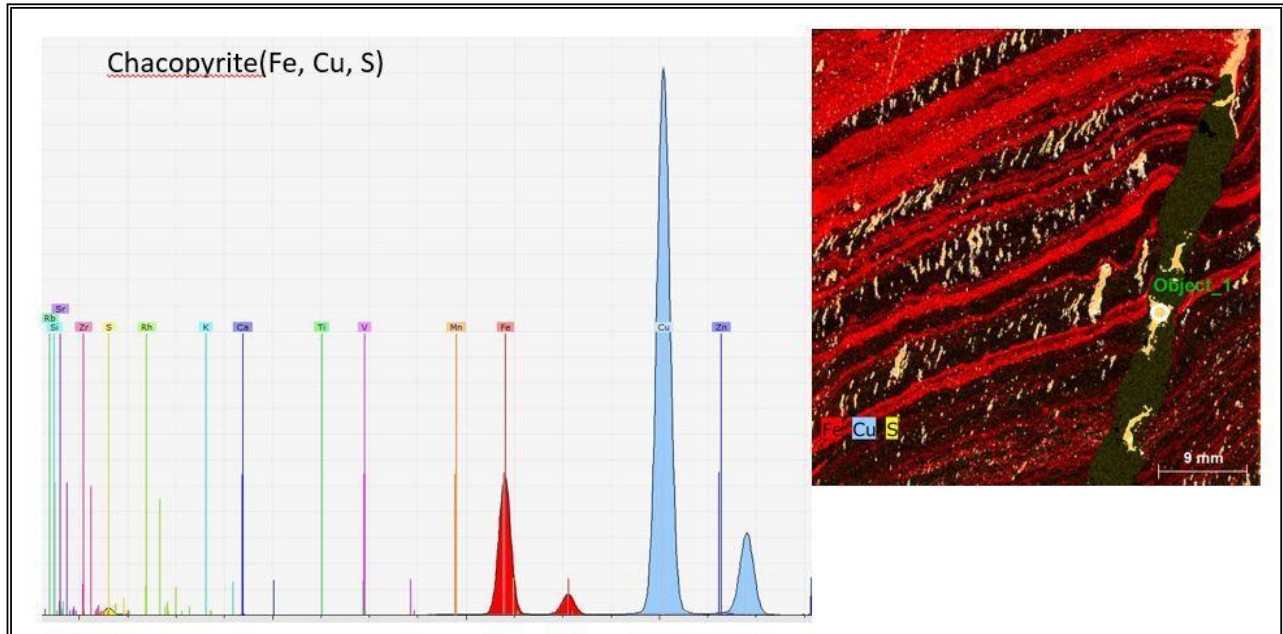


Figure 4.8: (Left) is a spectrum showing sulfide minerals present (Cu, Fe, S) which corresponds to the μ XRF image on the right showing the object location of interest selected for spectrum collection.

Figure 4.9 shows the spatial distribution of Ca, Si, Mn, S, Cu, Fe, As, Ti, and Ag in sample HA-715D-04. The map indicates that the quartz (Si) vein contains very little sulfide mineralization, and that hematite alters the intergrowths of sulfide mineralization. Silver is concentrated in the host rock as hot spots (Fig. 4.10), which is attributed to the rock's primary mineralogy rather than a later hydrothermal process.

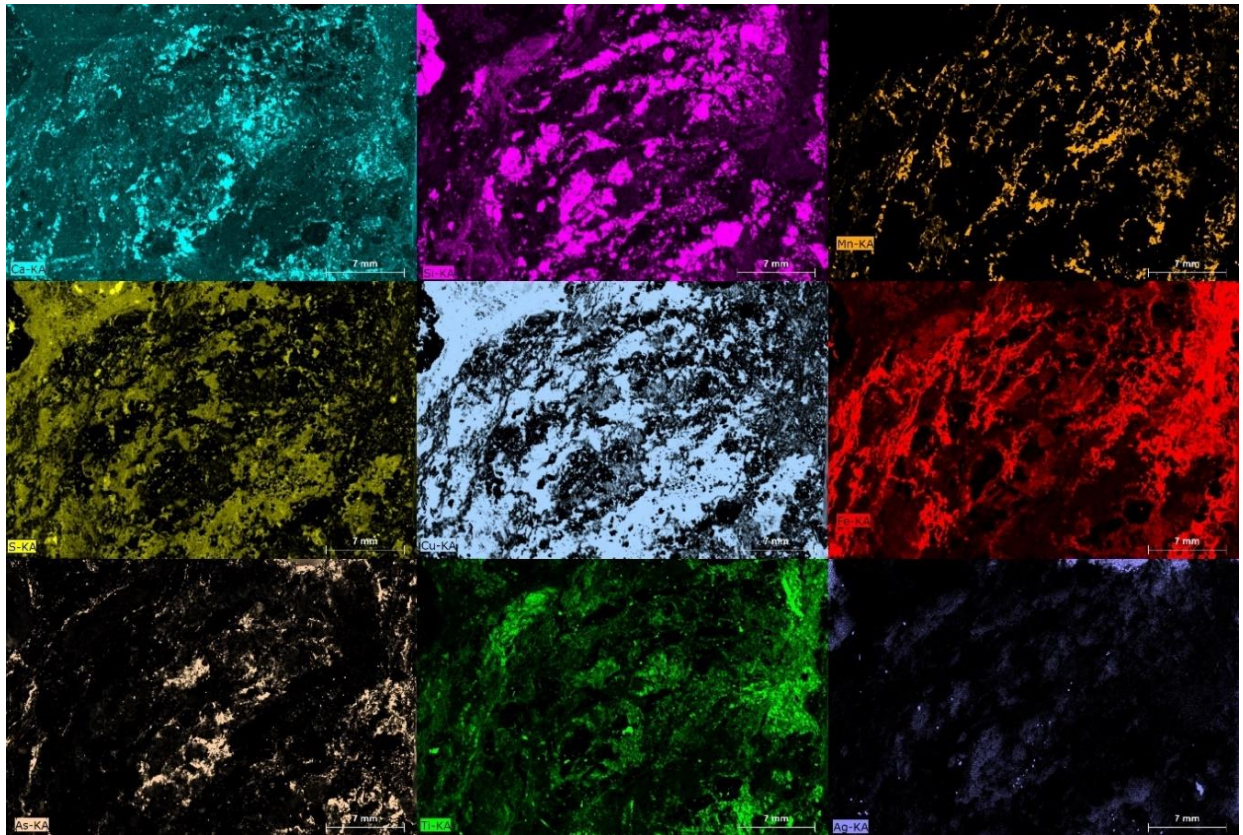


Figure 4.9: Elemental maps of Ca, Si, Mn, S, Cu, Fe, As, Ti, and Ag (HA-715D-04).

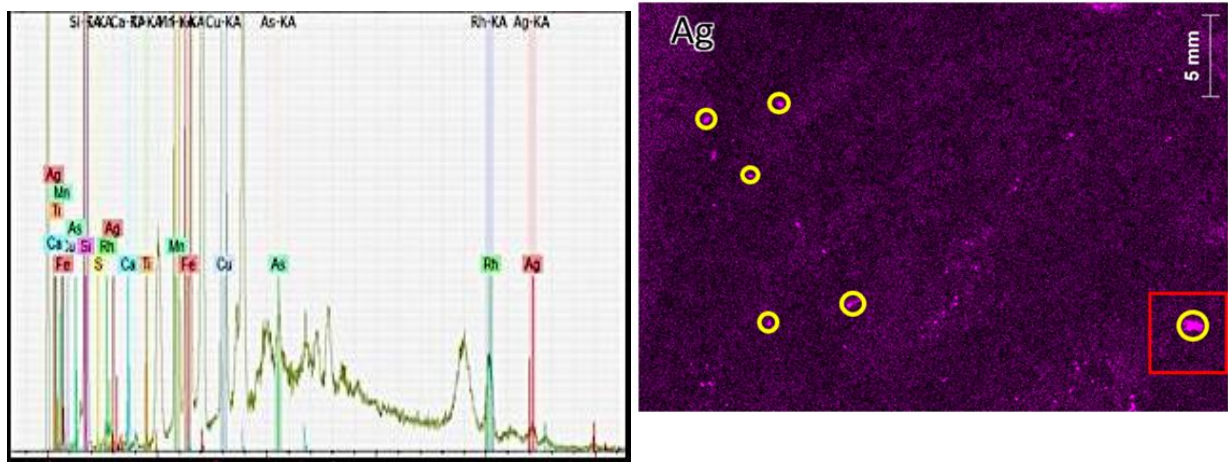


Figure 4.10: Left: a spectrum showing the presence of native Ag. Right: a map showing the presence of native Ag within hotspots identified readily in the maximum pixel spectrum.

Sample HA-1058D-04 (Fig. 4.11) shows maps of individual elemental distributions, while (Fig. 4.12) shows combined elemental distributions. In this sample, the concentrations of Cu, Si, S, Ca, and Fe correlate well, which is interpreted to reflect chalcopyrite and bornite along foliation, as well as quartz-calcite-chalcopyrite/bornite veinlets in the host rock.

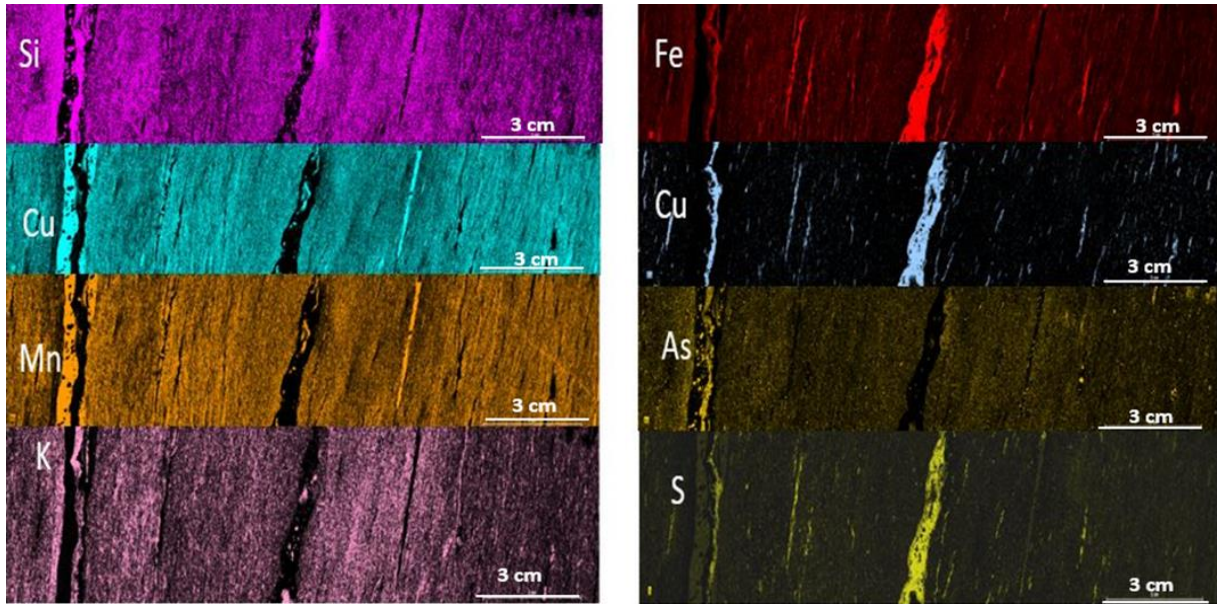


Figure 4.11: Elemental maps of Ca, Si, Mn, S, Cu, Fe, As, Ti, and Ag (HA-715D-04).

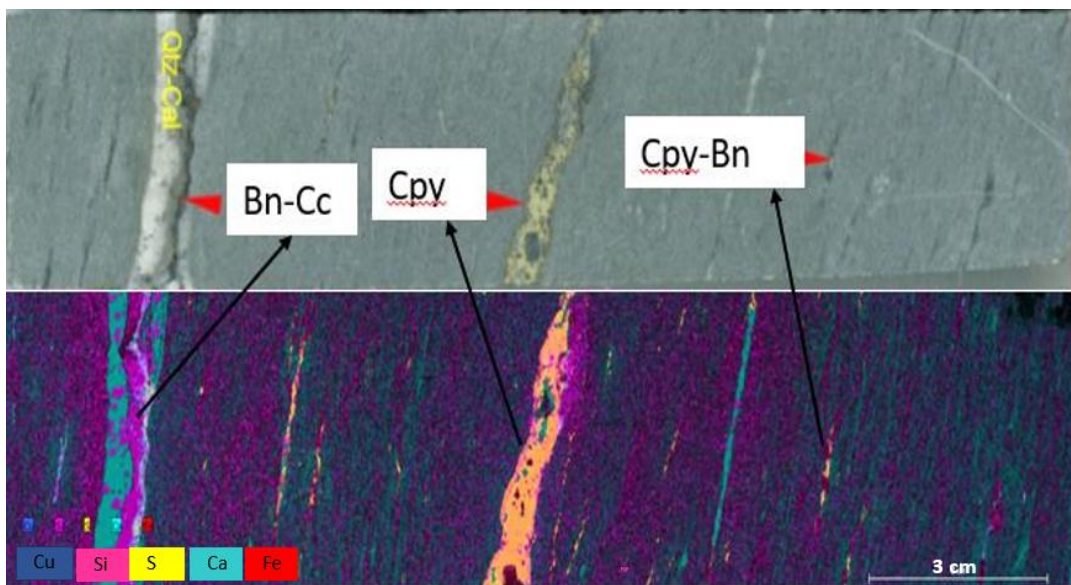


Figure 4.12: Top: Image of sample HA-1058D -04 showing sulfide mineralization along foliation. Bottom: Combined Cu, Si, S, Ca, Fe elemental map.

Figure 4.13 illustrates the concentration of Ca, Si, K, Mn, Mg, Al, S, Fe, Cu, As, Co, and Ti in sample HA-967D-01. The μ -XRF image shows dolomite and Mg-Mn-Ca carbonate veins. No Ag concentration exists in the samples, as shown in the spectrum of Figure 4.14. The circled false concentration of Ag results from scattering of the X-rays from the Rh tube.

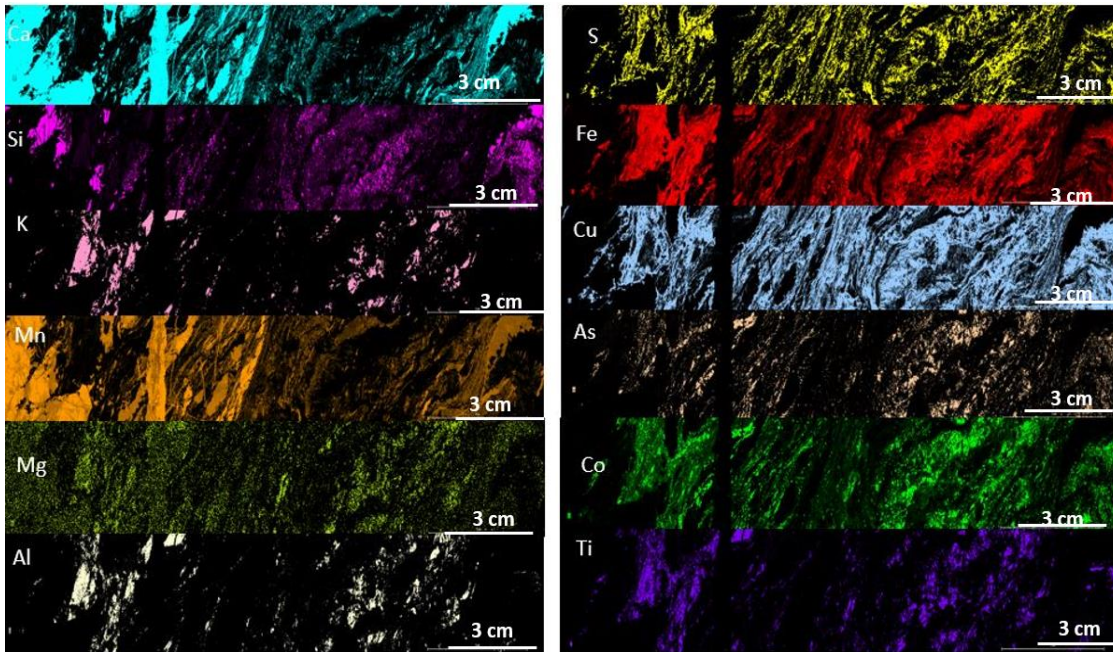


Figure 4.13: Elemental maps of Ca, Si, Mn, S, Cu, Fe, As, Ti, and Ag (HA-967D-01).

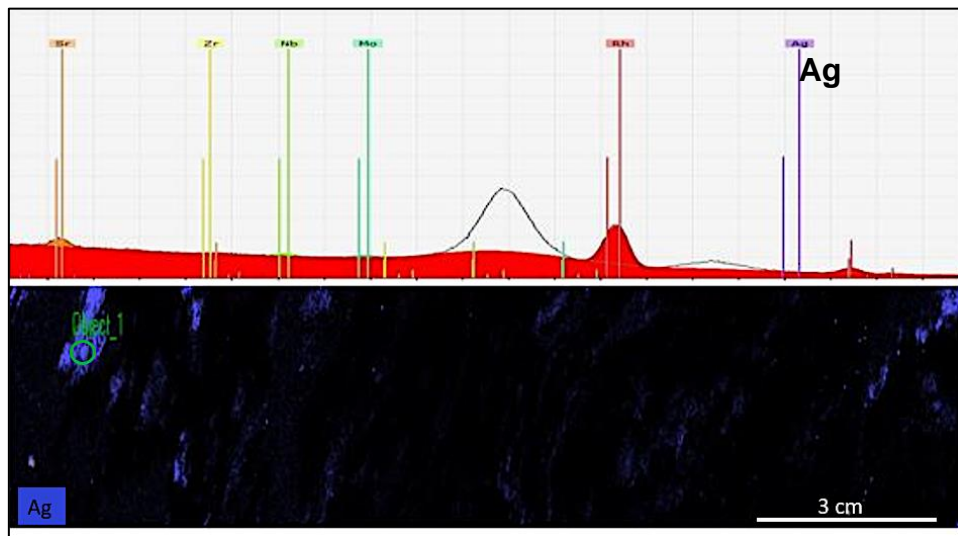


Figure 4.14: False map showing Ag, while the spectrum at the top shows no Ag peak.

Figure 4.15 shows Ca, Si, K, Mn, Mg, Al, S, Fe, and Ti distributions of sample HA-1015b-03. The vein is a boudinaged dolomite-calcite quartz vein with bornite-chalcocite crystals.

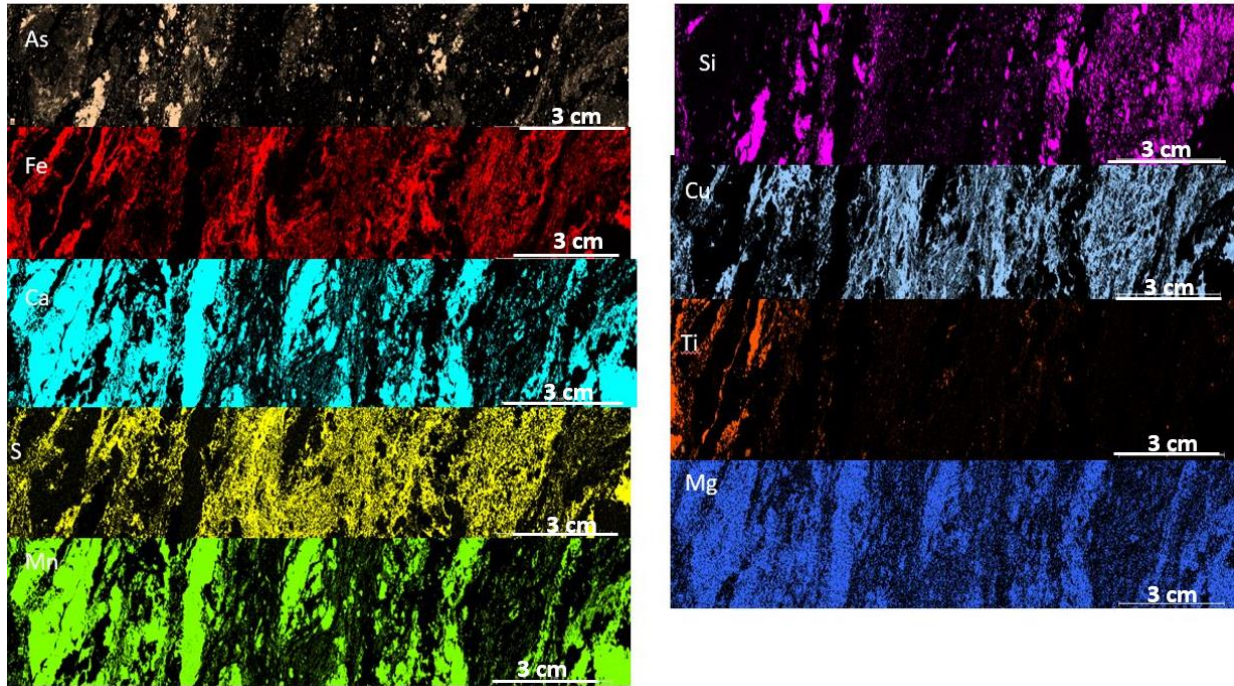


Figure 4.15: Micro-X-ray fluorescence image of sample HA-1015b showing elemental map distribution of As, Fe, Ca, S, Si, Cu, Ti, and Mg.

The mineralization of Zone 5 is characterized by a redox-buffered sulfide zonation that evolves from specular hematite to chalcocite to bornite to chalcopyrite to pyrite-galena-sphalerite. Most of the sulfides and minor Ag mineralization are concentrated in quartz-carbonate veins and structural fabrics such as foliation, crenulation cleavage, and shear zones. In crenulation cleavages, mineralization occurs concurrently with fold-related shearing, and the mineralizing fluid may have been derived from quartz calcite veins parallel to cleavages (Fig. 4.6) A correlation between assay data and drill core examination suggests that high copper grades are associated with vein and cleavage-hosted ores. Results from assays show a positive correlation between Cu and Ag (Fig. 4.2).

For vein-type mineralization, quartz-calcite veins host the majority of high-grade Cu mineralization. There are quartz-calcite veins throughout the stratigraphic succession; however, mineralized veins of centimeter- to meter-scale occur primarily in finely laminated and deformed metasedimentary rocks.

Pyrite, galena, arsenopyrite, sphalerite, chalcopyrite, bornite, and chalcocite are among the vein-hosted ore minerals, while quartz and calcite are gangue minerals. A high degree of deformational overprinting occurs in mineralized veins parallel to the bedding and foliation planes (Figs. 4.7 and 4.12). The layer-parallel sulfide-bearing veins are sometimes laminated, probably due to post-depositional deformation. A detailed petrographic study (Keeditse et al., 2022) identified distinct mineralizing events at Zone 5. In general, the paragenesis of the ore-stage sulfides described in Figure 4.16 corresponds with previous descriptions (e.g., Schwartz et al., 1996; Gorman, 2013; Walsh, 2014; Kelepile et al., 2020; Hall et al., 2021). The individual stages are described in terms of the relative timing of sulfide precipitation.

According to the μ XRF analysis, initially disseminated foliation-parallel bornite-chalcocite intergrowths are stretched and remobilized as axial cleavage after ductile shearing. The deformational overprinting of chalcopyrite alone and chalcopyrite-bornite-chalcocite intergrowths is also the same. Despite positive correlations between Cu and Ag (average 22 g/t Ag for the deposit), Ag minerals are not common at Zone 5. However, μ XRF and SEM-EDS analysis revealed the occurrence of rare native Ag around chalcocite grain boundaries (Fig. 4.16), suggesting later precipitation.

Mineral	Diagenetic	Main Cu-Ag hydrothermal (Damaran Orogeny)
Quartz	_____	_____
Calcite	_____	_____
Pyrite	_____	_____
Galena	_____	_____
Sphalerite	_____	_____
Arsenopyrite	_____	_____
Ni-Co-Fe sulfarsenide	_____	_____
Cobaltite	_____	_____
Glaucodot	_____	_____
Chalcopyrite	_____	_____
Chalcocite	_____	_____
Bornite	_____	_____
Silver	_____	_____
Covellite	_____	_____
Hematite	_____	_____
Rutile	_____	_____

Figure 4.16: Zone 5 Cu-Ag deposit paragenetic sequence observed in ore samples. As sphalerite is associated with pyrite and copper mineralization, another generation may occur during late hydrothermal activity (Keeditse et al., 2022).

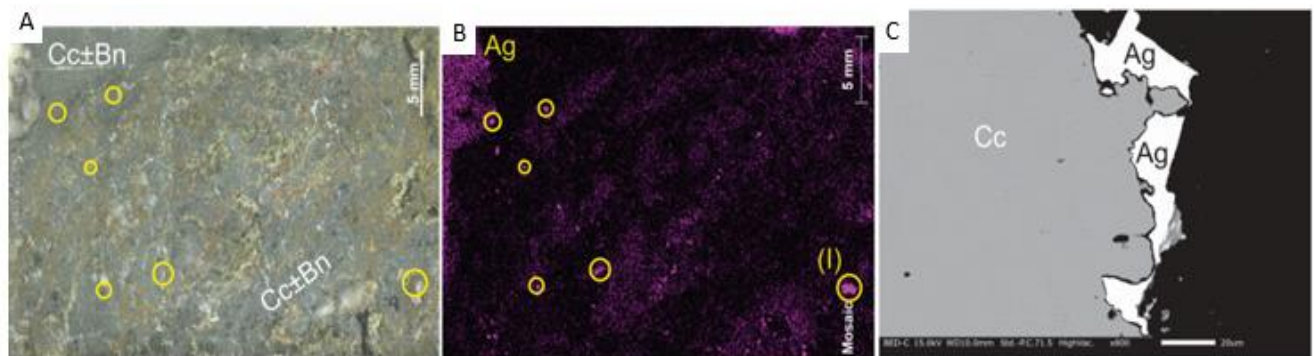


Figure 4.17: (A and B) host rock and μ XRF images showing traces of Ag in the sample selected from the maximum pixel spectrum; (C) Back-scattered electron image (BSE) showing native Ag around chalcopyrite.

4.6. DISCUSSION

A key strength of μ XRF is that it can scan large core samples relatively quickly, revealing chemical and mineralogical textures that are invisible to the naked eye (Ryan et al., 2018). An example is shown in Figure 4.7, which shows a micro-XRF chemical map of Ca, Mg, and Mn in a hydrothermally altered rock sample next to a true-color image of the same sample.

As summarized in Keeditse et al. (2022), in the Khoemacau district, most Cu-Ag deposits occur on the limbs and hinges of major folds (e.g., Hall et al., 2018b). At Zone 5, metallic mineralization is hosted preferentially by the carbonate-siltstone metasedimentary rock material of the lower D'Kar Formation, within 70 m of the continental redbeds of the Ngwako Pan Formation in the footwall. In the drill core examination of this deposit, it has been revealed that the ore is distributed along bedding, foliation, and crenulation. This implies a close spatial and temporal relationship between two cleavages, a close spatial and a combination of chemical and rheological controls on mineralization.

Zone 5 is characterized by the presence of hematite, chalcocite, bornite, and chalcopyrite, ascending in order, surrounded by a halo of pyrite, galena, and sphalerite in an outer halo (Keeditse et al., 2022). The metal zonation may be related to the transition from oxidizing to reducing conditions and to the availability of reduced sulfur in the metasediment host, given the location of the ores at an oxidizing-reducing boundary. The mineralization in consists of both a low-grade disseminated ore body and a high-grade veinlet body consisting of a layer parallel to the surface. It has been demonstrated that zone-hosted metallic mineralization (layer-parallel) and vein-hosted metallic mineralization (cross-cutting layers) share a close spatial and temporal relationship (Figs. 4.2 and 4.7), indicating a close spatial and temporal relationship between vein-hosted disseminated (layer-parallel) metallic mineralization along bedding and foliation

planes (Keeditse et al., 2022). According to the findings of Maeder et al. (2014), all mineralization styles can be explained because of progressive folding, which caused flexural slip along bedding planes in incompetent layers and fan-shaped fractures and crenulation cleavages in competent layers centered around the fold hinge plane in competent layers.

A μ XRF examination of the drill cores, coupled with petrographic observations, indicated that some mineralized quartz-calcite veins had both brittle and ductile overprints during deformation, suggesting some metallic mineralization had been introduced prior to deformation. It is challenging to decipher the structural paragenesis and deformational history at Zone 5. However, the ore grade, structurally controlled mineralization results from a regional deformational event resulting from a structural paragenesis. A number of these local structural fabrics can be referred to as fold-limb environments, which indicate that flexural slip and crenulation cleavages have been the primary mechanisms responsible for regional progressive folding (e.g., Maeder et al., 2014; Hall et al., 2018b). Considering the rheological contrasts that exist at the redox interface, the strain has been localized in a package of carbonate-siltstone that is mechanically weaker than the carbonate-siltstone package (e.g., Hall et al., 2018b), leading to the formation of the structural permeability required during hydrothermal activity, when the rocks had already solidified. Various Cu-(Fe)-sulfide minerals are found in Zone 5 deposit. The most commonly occurring ones include chalcopyrite, bornite, and chalcocite, followed by minor amounts of pyrite, arsenopyrite, galena, and sphalerite.

A paragenetic analysis of hypogene mineralization data (Figure 4.16) reveals two main stages of hypogene mineralization: (1) the **Diagenetic Stage**, characterized chiefly by fine-grained framboidal pyrite as well as minor ore minerals, and (2) the **Hydrothermal Cu-Ag Stage**, characterized by the formation of early to late hydrothermal Cu-Ag sulfides as well

as accompanying hydrothermal alteration (Keeditse et al., 2022). There are two stages in the mineralization process: quartz and calcite are the main host rocks and gangue minerals.

The existence of the Zone 5 deposit and the development of other Cu-Ag deposits in the Khoemacau district and the KCB can be explained by an epigenetic hydrothermal Cu-Ag mineralization stage. The ore stage is dominated by Cu mineralization and is syn-orogenic and multi-stage, indicating that the ore stage has been formed over an extended period. Generally, the mineralization is characterized by a simple suite of Cu sulfides (chalcopyrite-bornite-chalcocite) that display a variety of intergrowth textures, which indicate a co-crystallization of the Cu sulfides.

It is noteworthy that Cu sulfides are coarse in grain size and preferentially grow along structural features like foliation, veins, crenulation cleavages, and shear zones, which indicates that it originated from a syn-orogenic source.

The assay data indicate a strong positive correlation between Cu and Ag (Fig. 4.2). However, Ag minerals are not widespread at Zone 5, which suggests that Ag is largely refractory within the Cu sulfide crystal lattice of Zone 5. Despite this, micro-XRF analyses reveal some native Ag present around the crystal margins of the chalcocite crystals, suggesting that some Ag mineralization was part of a late ore fluid (Keeditse et al., 2022).

Chapter 5: Gold mineralization, Awak Mas deposit, Sulawesi (Indonesia)

5.1 INTRODUCTION

Historically, the exploration and extraction of Au in Indonesia have been centered on volcanic rock-hosted deposits. The Indonesian Metallogenic Map (Harahap, 2014) illustrates that more than 90% of Indonesia's Au deposits are epithermal, volcanic rock-hosted deposits, 6.2% by porphyry and skarn, and the rest by volcanic-hosted massive sulfide and Carlin deposits. Presently, Au exploration activities focus on metamorphic rock-hosted deposits, particularly in the eastern part of the country (Fig. 5.1).

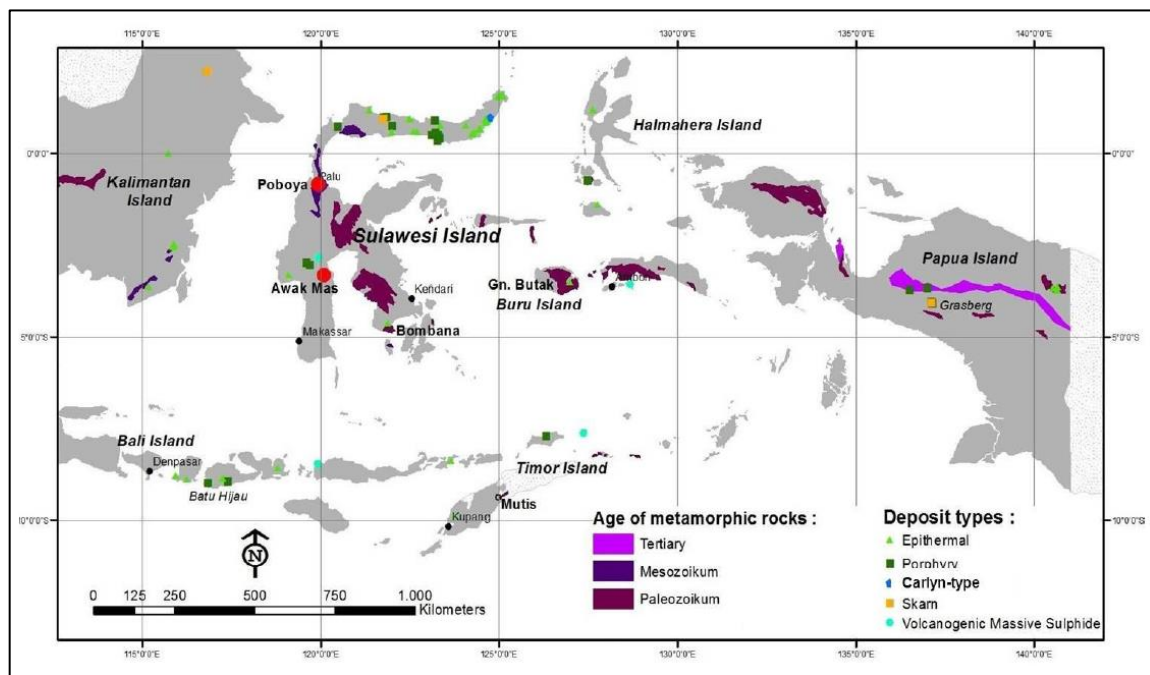


Figure 5.1: Metamorphic rock belts and gold deposits by type in Eastern Indonesia (Harjanto and Meyer, 2015)

In Indonesia, the Awak Mas deposit is one of many metamorphic rock-hosted Au deposits located within the Cretaceous Latimojong formation on Sulawesi Island (Fig. 5.2) Since 1987, more than 1000 holes have been drilled, resulting in 118081.30 m of drill core (Querubin & Walters, 2012). There are three gold orebodies in the Awak Mas deposit: Salu Bulu, Tara, and

Awak Mas (Fig. 5.3). Overall, Awak Mas has an estimated indicated and inferred resources of 38.4 Mt at 1.41 g/t Au, which is equivalent to 1.74 Moz gold (Company Report, 2017).

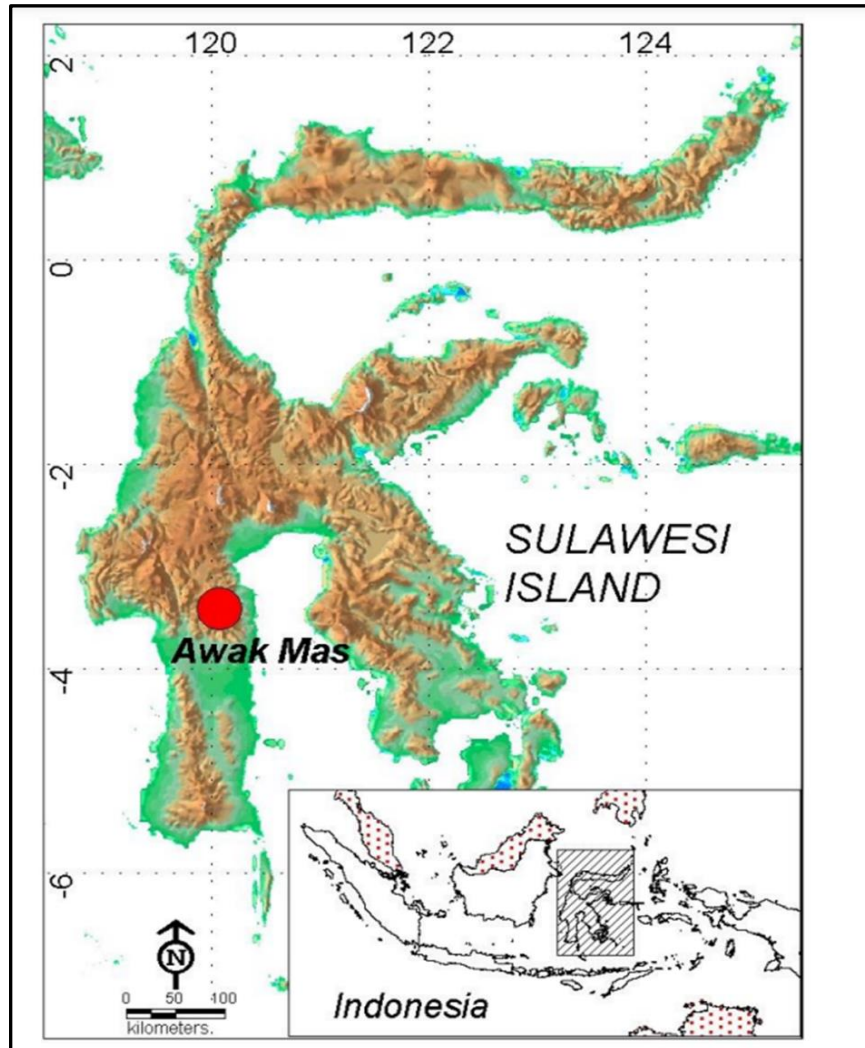


Figure 5.2: Location map of the Awak Mas mesothermal gold deposit, Sulawesi Island, Indonesia (Harjanto and Meyer, 2015).

Specifically, the samples studied on this project focus on the Salu Bulu ore body, which hosts Au mineralization in metasedimentary rocks. The precise timing of Au mineralization with respect to the alteration processes in the Salu Bulu deposit can be better understood. Micro-XRF analysis was used to visualize hydrothermal events during Au mineralization to improve the geologic understanding.

5.2 GEOLOGIC SETTING

The Indonesian archipelago includes the island of Sulawesi (Fig. 5.1). The basement sequence comprises Lower Cretaceous blueschist, diorite and ultramafic rocks, which have been tectonically interbedded. The Latimojong Metamorphic Complex hosts the Salu Bulu prospect. A series of meta-volcanic and volcanoclastic units surround the Latimojong Metamorphic Complex. This complex includes meta-dark (graphitic), green (chloritic), and red (hematitic) mudstone, siltstone, and sandstone. The foliation of the host rock is oriented northwest and dips northeast.

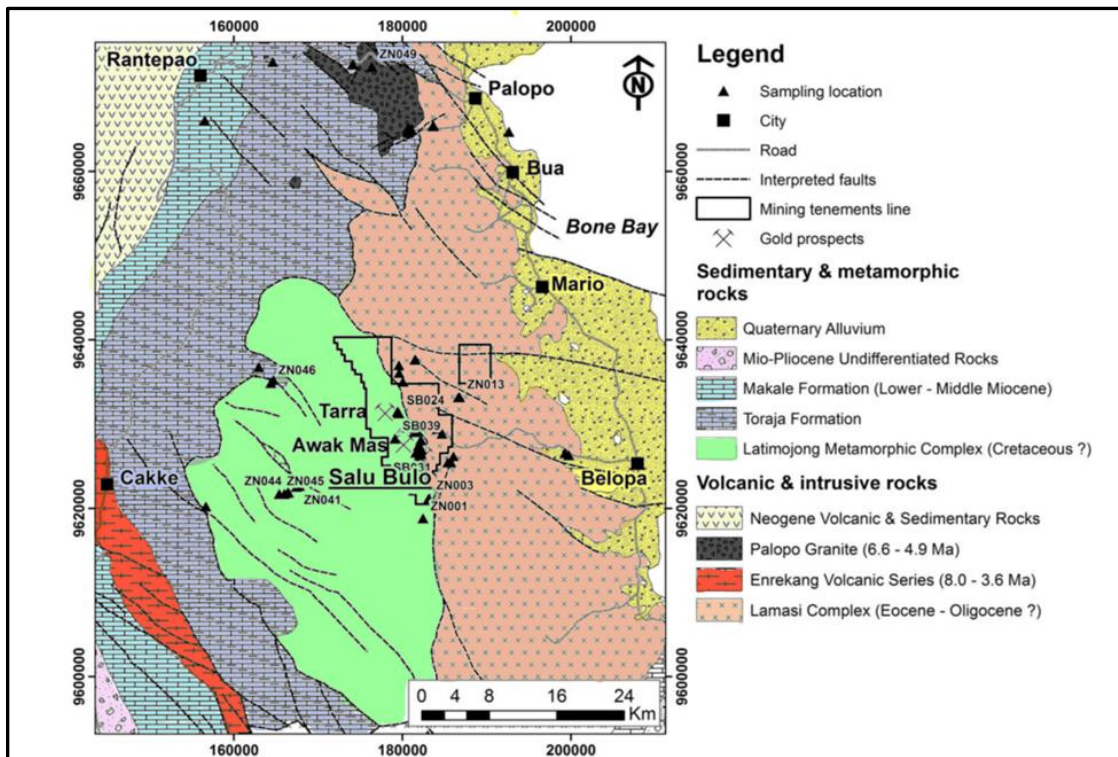


Figure 5.3: Geological map of the study area (White et al., 2017).

It is unclear how Au mineralization in Salu Bulu is controlled structurally. There is a potential Au deposit on the Salu Bulu prospect near the Kandeapi Suture, the boundary between

the Cretaceous and Cenozoic plates (Metcalf, 2011; Hennig et al., 2011). The four arms of the island illustrate the complex tectonic history of the island (Katili, 1978; Hamilton, 1979).

The Awak Mas project can be found in the Latimojong Mountain Region of the South Arm (Fig. 5.3). The Latimojong Metamorphic Complex is an accretionary complex made up of low- and high-grade metamorphic rocks derived from a mixture of siliciclastic, calcareous, and volcanic rocks. Tectonically, these metamorphic rocks are mixed with cherts and ophiolitic rocks (White et al., 2017). A clastic rock layer of the Eocene–Oligocene Toraja Formation and Lower-Middle Miocene Makale Formation unconformably overlies the western part of the complex, while an Eocene-Oligocene Lamasi Complex covers the eastern part (Bergman et al., 1996; Djuri et al., 1998; White et al., 2017).

The calc-alkaline or island-arc tholeiitic rocks, potassic calc-alkaline rocks, and shoshonitic rocks in western Sulawesi are the results of magmatism that occurred during the Eocene to Pleistocene. In an active subduction environment, crustal thickening and partial melting cause magmatism (Priadi et al., 1994; Bergman et al., 1996; Elburg & Foden, 1999; Maulana et al., 2016; White et al., 2017). As shown in Figure 5.3, the Mio-Pliocene Palopo Granite intruded the northern part of the Latimojong Metamorphic Complex. A potassium-rich calc-alkaline composition characterizes the Palopo Granite (Priadi et al., 1994; White et al., 2017). During plate collision, continental crustal melting formed the intrusion (Priadi et al., 1994; Bergman et al., 1996), or arc magmatism created it (White et al., 2017).

The Latimojong Metamorphic Complex is locally divided into the basement and the cover sequences. Deep marine turbidites and volcanic and volcanoclastic rocks are in the cover sequence, which was part of the Latimojong Metamorphic and Lamasi complex (Figs 5.3 and 5.4). In Figures 5.4 and 5.5, parallel faults trending northeast-southwest and northwest-southeast

categorized into two distinct types (Querubin & Walters, 2012). The first consists of sheeted, stockwork, and milky quartz veining and associated alteration that conforms to the shear fabric, whereas the second consists of quartz veining and breccias with steeper dips associated with high-angle faults and/or shear zones cutting both the flyschoid cover sequence and basement metamorphics. A typical hydrothermal alteration style is carbonation, represented by graphite banding. Several alteration types of graphitic, quartz-carbonate veins, and albitization-silicified breccias contain the pyrite ore mineral resulting in euhedral coarse-fine grains. The features listed above represent an epizonal type of orogenic Au deposit.

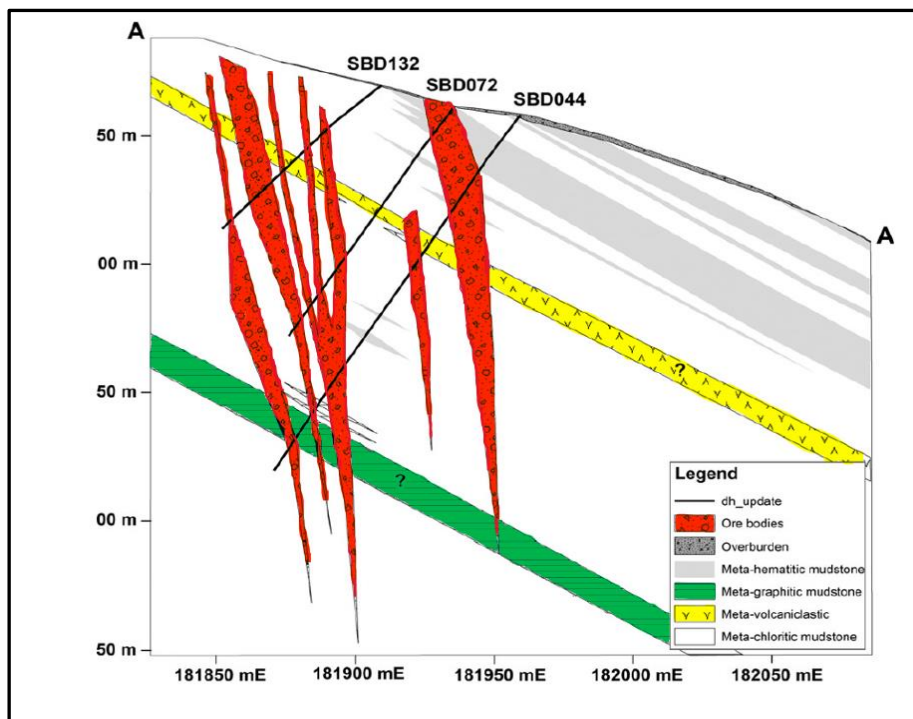


Figure 5.5: Mineralized zones (orebodies) on the Salu Bulu prospect have steep east-dipping dips (modified from PT Masmindo Dwi Area).

5.3. ANALYTICAL PARAMETERS

A drill core sample was studied from the Salu Bulu prospect for analysis. A total of seven samples of hydrothermally altered rocks were analyzed, and these analyses helped to characterize geochemical variations occurring in the different host-rock lithologies, alteration,

and mineralization zones. As shown in Table 5.1, the study was conducted under analytical conditions with a standard beam voltage and current of 50 kV and 600 μ A.

Table 5.1: Analytical conditions for Awak Mas Au deposit.

Sample ID	Pixel spacing	Dwell Time	Map time	Detectors
SBD047-79.18-79.28	50 μ m	35 ms	~16 hrs	1 SDD
SBD132-62.10-62.20	30 μ m	35 ms	~16 hrs	1 SDD
SBD044-45.20-45.40	50 μ m	35 ms	~20 hrs	1 SDD
SBD072-89.20-89.30	50 μ m	35 ms	~15 hrs	1 SDD
SBD132-59.20-59.25	50 μ m	35 ms	~12 hrs	1 SDD
AMD644-66.00-66.15	50 μ m	35 ms	~9 hrs	1 SDD
SBD008-29.15-29.30	50 μ m	35 ms	~15 hrs	1 SDD

5.4. RESULTS

Seven samples from the Salu Bulu prospect were mapped to obtain elemental maps.

Major and trace element analyses collected at Akita University are shown in Table 5.2.

Table 5.2: Major and trace element composition of host rocks and altered zones.

Lithology	Meta-mudstone			Meta-volcanics			Least altered host rock zone					Strongly altered host rock zone		
Sample ID	SBD047-79.18-79.28	SBD044-45.20-45.40	SBD132-62.10-62.20	SBD072-89.20-89.30	SBD132-59.20-59.25	SBD047-79.18-79.28	SBD132-62.10-62.20	SBD044-45.20-45.40	SBD072-89.20-89.30	SBD132-59.20-59.25	AMD644-66.00-66.15	SBD047-79.18-79.28	SBD132-62.10-62.20	SBD044-45.20-45.40
wt%														
SiO ₂	62.91	38.55	10.19	55.56	54.86	57.27	50.41	13.41	62.87	53.61	56.41	62.14	62.26	59.17
Al ₂ O ₃	15.93	7.52	3.05	16.25	12.83	20.60	11.88	4.20	16.50	16.39	18.14	21.37	11.74	18.11
Fe ₂ O ₃	3.33	13.42	0.85	5.23	7.52	7.06	19.00	24.22	5.22	10.44	11.41	1.88	7.31	2.74
MgO	2.01	5.67	8.92	3.99	3.99	0.83	9.26	8.39	1.46	2.14	0.57	0.91	9.78	1.43
CaO	5.25	21.75	1.10	7.56	11.11	1.76	7.29	38.98	2.99	8.07	0.12	1.91	8.00	6.94
Na ₂ O	9.23	6.67	75.39	9.83	6.86	9.92	0.00	1.74	8.64	5.24	11.12	9.98	0.10	9.39
K ₂ O	0.11	0.26	0.01	0.07	0.22	0.31	0.09	0.37	0.07	0.71	0.05	0.76	0.02	0.18
TiO ₂	0.54	1.59	0.09	0.61	0.74	0.75	1.22	1.41	0.83	0.88	1.75	0.58	0.15	1.11
P ₂ O ₅	0.05	1.44	0.04	0.16	0.33	0.11	0.00	1.66	0.03	0.06	0.00	0.02	0.01	0.21
MnO	0.25	1.75	0.02	0.20	0.20	0.16	0.29	4.19	0.15	0.16	0.02	0.11	0.40	0.47
Cr ₂ O ₃	0.01	0.02	0.00	0.01	0.02	0.02	0.02	0.03	0.01	0.02	0.06	0.01	0.02	0.01
Total	99.6	98.6	99.7	99.5	98.7	98.8	99.5	98.6	98.8	97.7	99.7	99.7	99.8	99.8
ppm														
Cu	266.32	2301.92	29.00	116.89	280.36	95.91	1253.38	66.25	49.63	253.25	1124.96	163.93	706.13	130.79
Zn	606.52	841.12	105.90	640.79	1397.94	121.44	957.23	616.85	240.99	615.59	389.19	178.90	197.14	98.39
Ni	86.20	230.54	6.64	84.88	24.40	37.61	230.02	351.51	63.98	5.61	1158.53	22.84	94.19	39.65
S	8633.14	79844.18	8372.91	29701.83	23669.47	1567.89	8446.38	4416.00	23386.66	11891.89	6900.52	24029.22	134671.08	21328.72
As	237.33	545.60	17.73	103.51	182.10	65.77	172.54	665.49	38.00	67.68	<0.001	76.00	190.62	75.90
Sr	1943.55	4427.26	182.64	1647.14	1951.39	953.89	4353.13	22289.51	873.20	1847.93	620.37	1944.03	3935.23	1104.06
Au	203.80	266.16	23.65	215.46	289.25	87.36	100.95	74.18	37.00	<0.001	72.14	<0.001	63.69	186.70
Ag	54.94	10.45	<0.1	40.93	<0.001	<0.001	<0.001	<0.001	<0.001	<0.001	<0.001	<0.001	<0.001	<0.001
Zr	476.48	898.43	18.97	243.98	129.77	288.70	590.37	1194.40	463.00	128.05	668.57	529.55	372.72	799.96

5.4.1 Description of the ores

Salu Bulu is characterized by orebodies trending north south that dip steeply eastward (Figs.5.4 and 5.5) and is associated with veins, stockworks, and breccias with an orientation subparallel and cut across the foliation of the host rocks. (Fig. 5.6). In the Salu Bulu prospect, multiple events resulted in veins that are visually indistinguishable from each other, and that can be identified using elemental maps. Observations of cross-cutting relationships on a micron scale allow the veins to classify into three stages: Stage 1, Stage 2 and Stage 3 (Figs. 5.7 and 5.8).

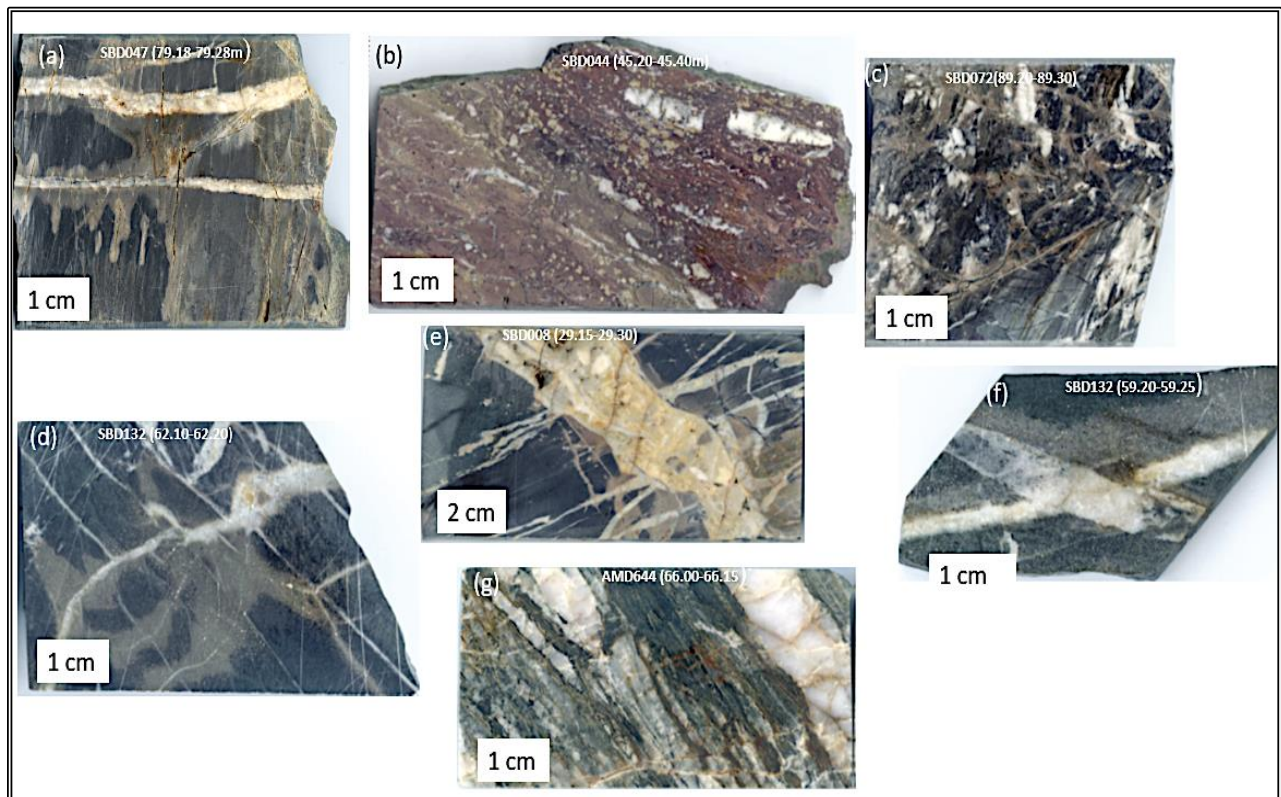


Figure 5.6: Photographs of host rocks which consist of (a), carbonaceous mudstone (b), meta-(red) hematitic mudstone (c), chloritic meta volcanic (d), meta volcanic (e), carbonaceous metapelite (f), meta-volcanic (g), chlorite schist.

Minerals		Stage-1	Stage-2		Stage-3
			Early	Late	
Mineral alteration	Albite	-----	████████████████████		-----
	Ankerite-dolomite-calcite	-----	██████████	-----	
	Apatite	-----	-----	-----	-----
	Baddeleyite	-----	-----	-----	-----
	Chlorite	-----	-----	-----	-----
	Dickite	-----	-----	-----	-----
	Goyazite	-----	-----	-----	-----
	Kaolinite	-----	-----	-----	-----
	Monazite	-----	-----	-----	-----
	Rutile	-----	-----	-----	-----
	Siderite	-----	-----	-----	-----
	Quartz	-----	██████████	-----	██████████
	Xenotime	-----	-----	-----	-----
	Zircon	-----	-----	-----	-----
	Ore Minerals	Bornite	-----	-----	-----
Carrollite		-----	-----	-----	-----
Chalcocite		-----	-----	-----	-----
Chalcopyrite		-----	-----	-----	-----
Chromite		-----	-----	-----	-----
Covelite		-----	-----	-----	-----
Enargite-Luzonite		-----	-----	-----	-----
Galena		-----	-----	-----	-----
Hematite		-----	-----	-----	-----
Ilmenite		-----	-----	-----	-----
Native gold		-----	-----	-----	-----
Pyrite		-----	████████████████████	-----	-----
Scheelite		-----	-----	-----	-----
Sphalerite		-----	-----	-----	-----
Tenantite-tetrahedrite		-----	-----	-----	-----
Wolframite	-----	-----	-----	-----	

Legend: ██████████ Abundant — Common --- Rare

Figure 5.7: Mineral alteration and paragenetic sequence of the Salu Bulo prospect showing the three stages of hydrothermal activity and base- and precious-metal mineralization in the Awak Mas deposit (Renaldi Suhendra, Akita University; pers. comm. 2021). The details of Au mineralization with respect to three stages are not understood in detail. This is the objective of the study with a μ XRF study instrument.

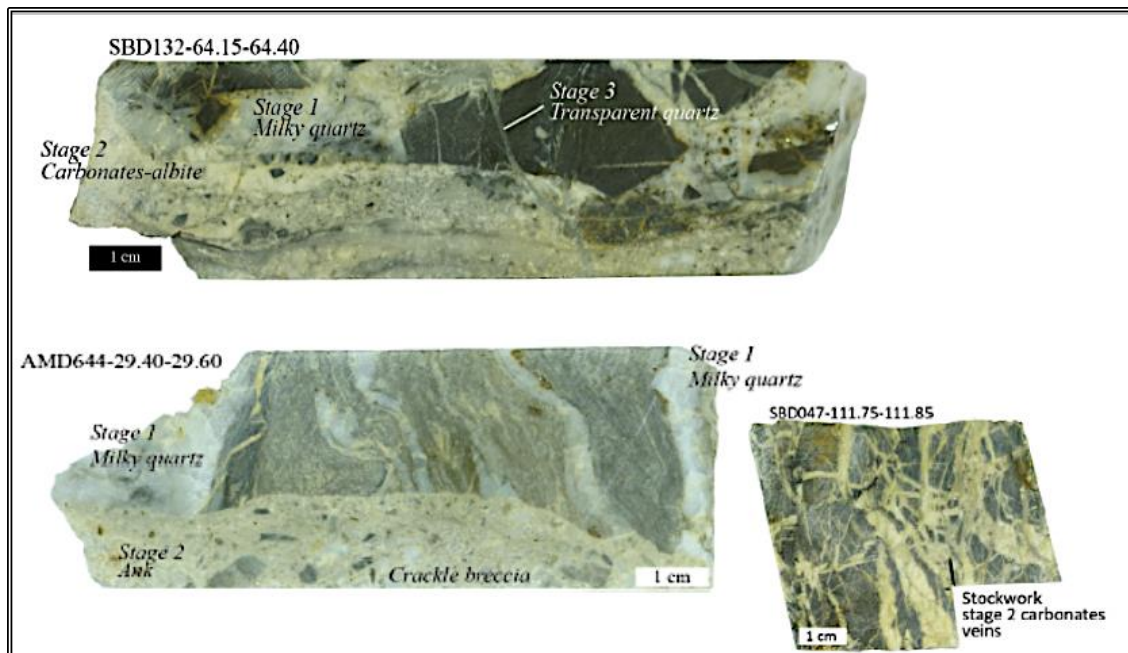


Figure 5.8: Photographs of the main stages of vein mineralization.

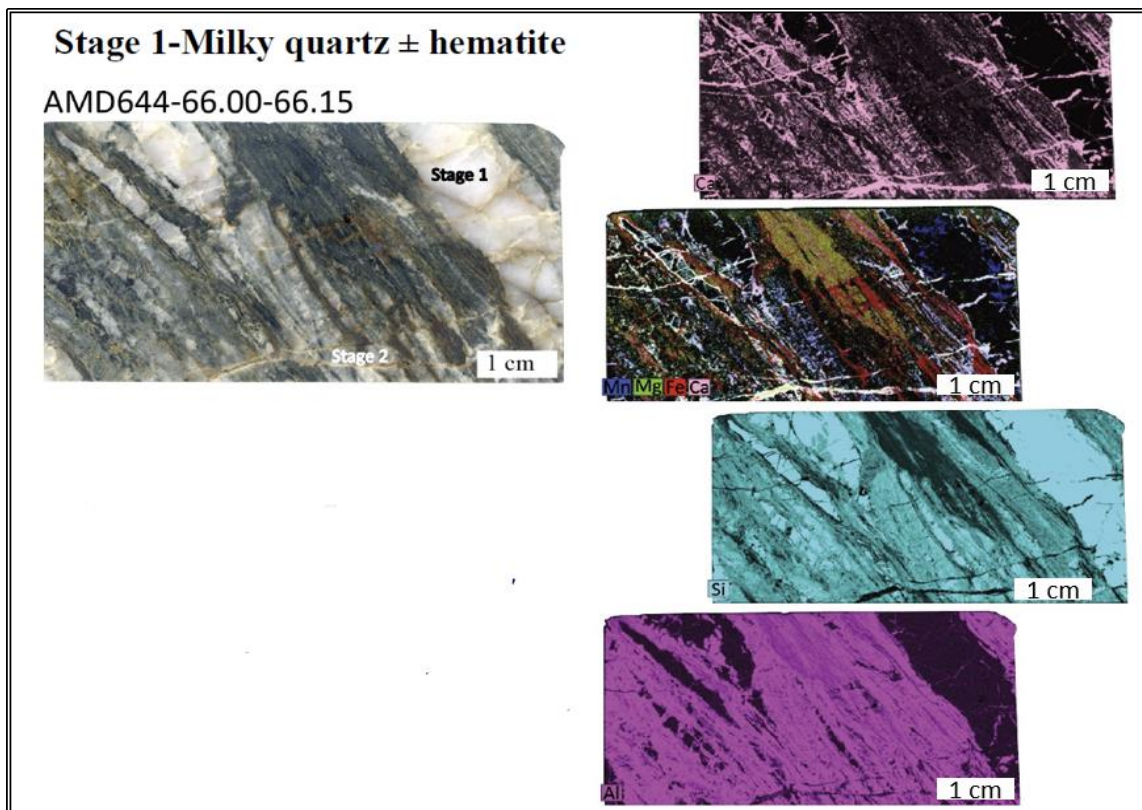


Figure 5.9: (left), host rock (right), micro-XRF maps showing the chemical and mineral variations of stage 1 vein (milky quartz) and the locations of elements of interest.

Although Stage-1 veins contain a small amount of hematite, they are generally composed of milky quartz, which runs parallel and subparallel to the foliation of the host rocks. Stage-1 veins are rarely found with albite and carbonates, whereas Fe-rich minerals dominated by sulfides and hematite replacing chlorite in (Fig. 5.9).

The Stage-2 vein consists primarily of carbonates-albite with minor amounts of quartz and hematite in the early stage and later cut by a vein rich in albite. There is also intense carbonatization (adding Ca, Mg, Fe, and Mn) and albitization (Fig. 5.10).

Stage-3 vein mainly consists of transparent quartz overprinting the earlier veins. The addition of Ca, Si, and Al and the loss of K and Fe from the host rocks are the common features in the alteration halo (Fig. 5.11). As is evident from alteration halo observations made in various host rocks, hydrothermal alteration is characterized by similar alteration assemblages, which are carbonates, albite, quartz, hematite, sulfides, and hematite with minor amounts of rutile. The veins are less abundant or do not contain sulfide minerals. In the Salu Bulo prospect, Au mineralization is associated with intense alteration such as carbonatization, albitization, silicification, and sulfidation.

Native Au is present in stage 3 transparent quartz veins but rarely occurs in Stage 2 carbonates albite veins (Fig. 5.12). Most of the Au in pyrite is found as micro-inclusions (Fig. 5.13). Photomicrographs and μ XRF analysis (Fig. 5.14) reveal native Au in strongly altered meta-hematitic mudstone. Also, in meta-volcanic rocks, native Au occurs at the contact between veins and host rock.

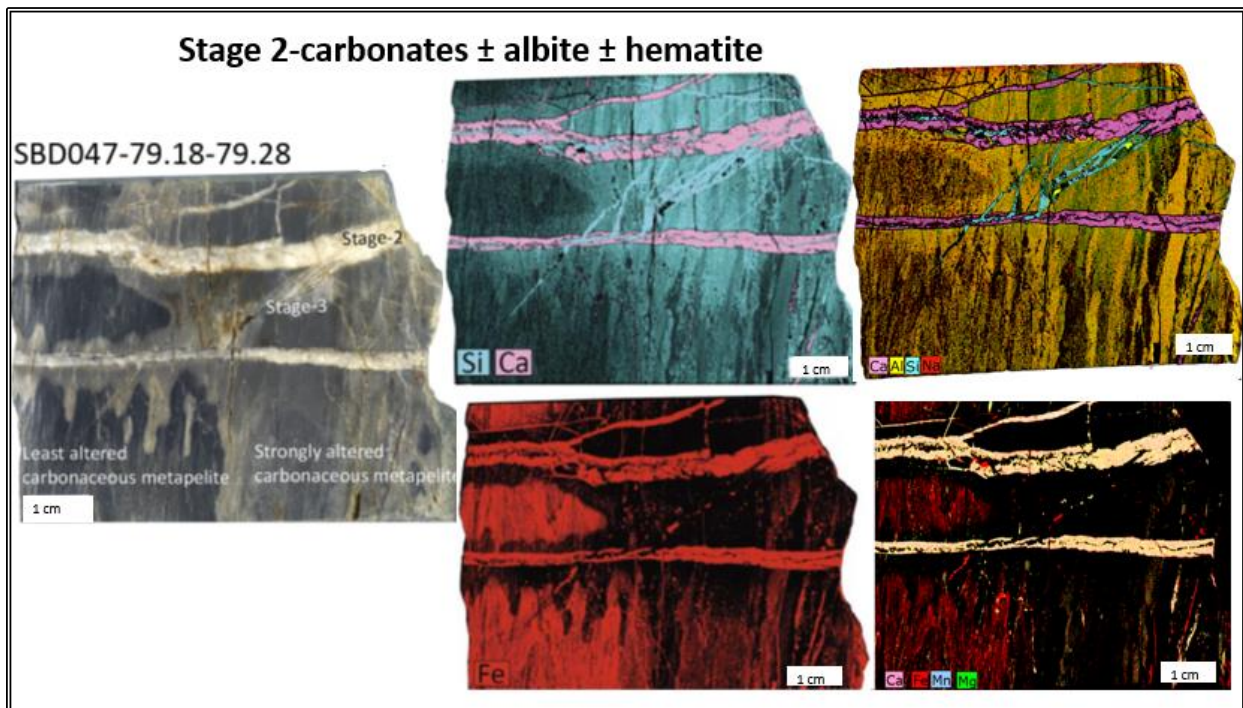
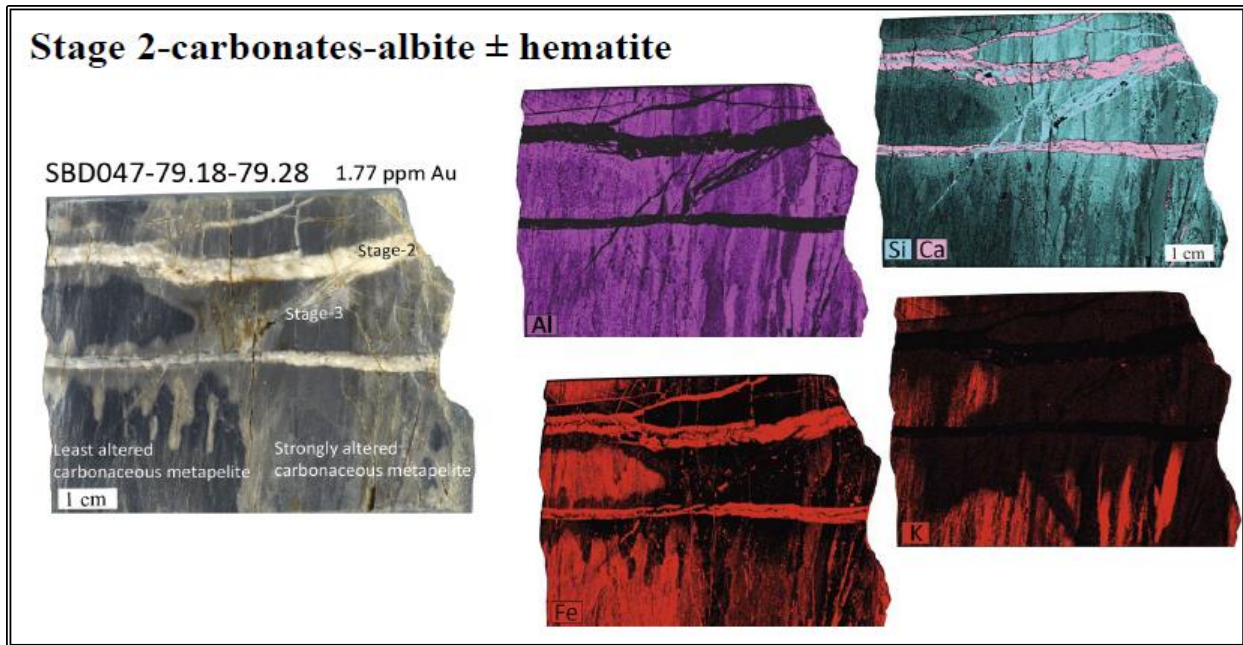


Figure 5.10: (left), host rock (right), μ XRF maps showing the chemical and mineral variations of Stage 2 carbonate-albite vein with a small amount of hematite.

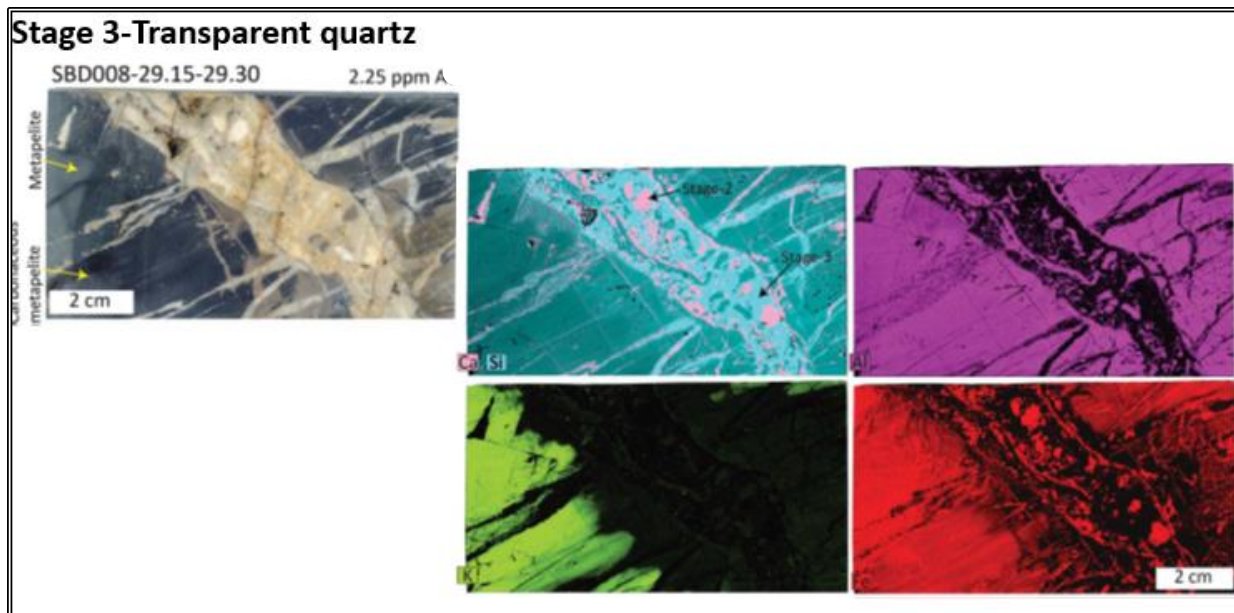


Figure 5.11: (left), host rock (right), μ XRF maps showing the chemical and mineral variations of Stage 3 vein (transparent quartz).

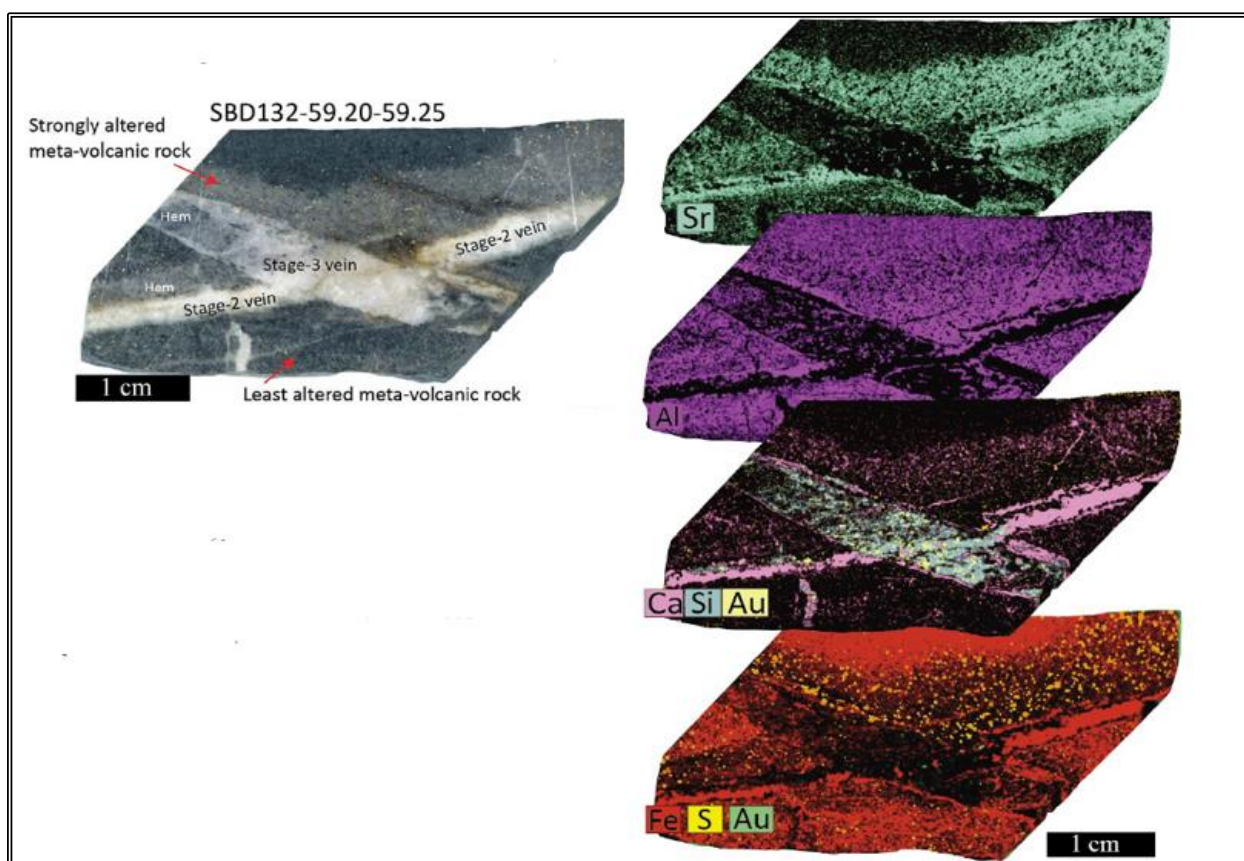


Figure 5.12: (left), host rock (right), μ XRF maps showing native Au in veins.

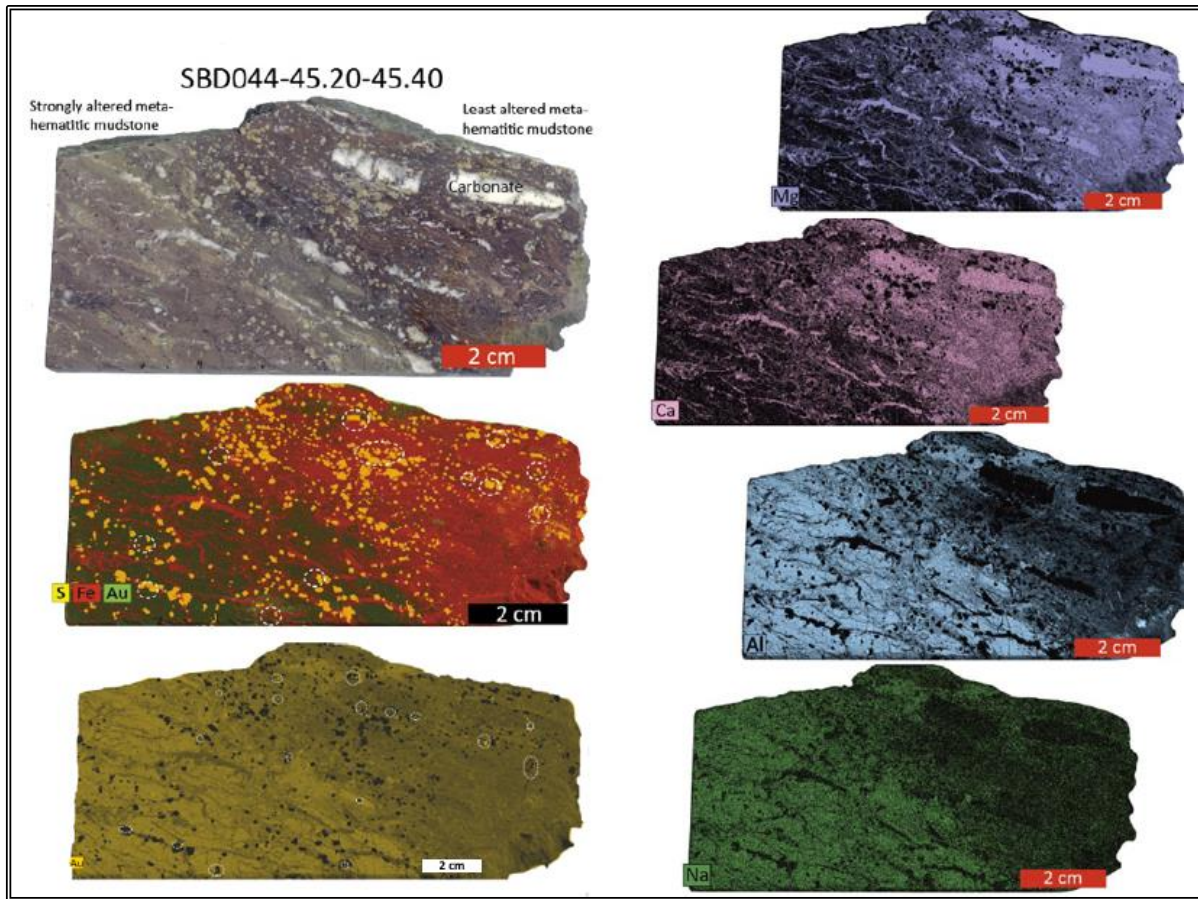


Figure 5.13: Micro-XRF elemental maps showing gold (Au) in pyrite (FeS_2) inclusion.

5.4.2 Mineral chemistry and bulk chemical composition

Five samples were selected for bulk composition and mineral chemistry because they exhibit unaltered, least altered, and strongly altered zones. The SiO_2 content of unaltered host rock ranges from 10.18 to 62.91 wt%, CaO ranges from 1.10 to 21.75 wt%, Na_2O 6.67 to 75.39 wt%, MgO 2.01 to 8.92 wt%, Fe_2O_3 0.85 to 13.42 wt%, and K_2O 0.01 to 0.26 wt% (Table 5.2).

In general, intense and least-altered host rocks have a higher K_2O content than unaltered host rocks, which range from 0.02 to 0.76 wt%. Unaltered host rocks have Ni contents ranging from 6.64 to 230.5 ppm, whereas strongly altered host rocks have Ni contents ranging from 0.00 to 210.3 ppm (Table 5.2). The Au content of strongly altered host rock zones is positively correlated with Ni and inversely correlated with Sr (Figs. 5.15 and 5.16).

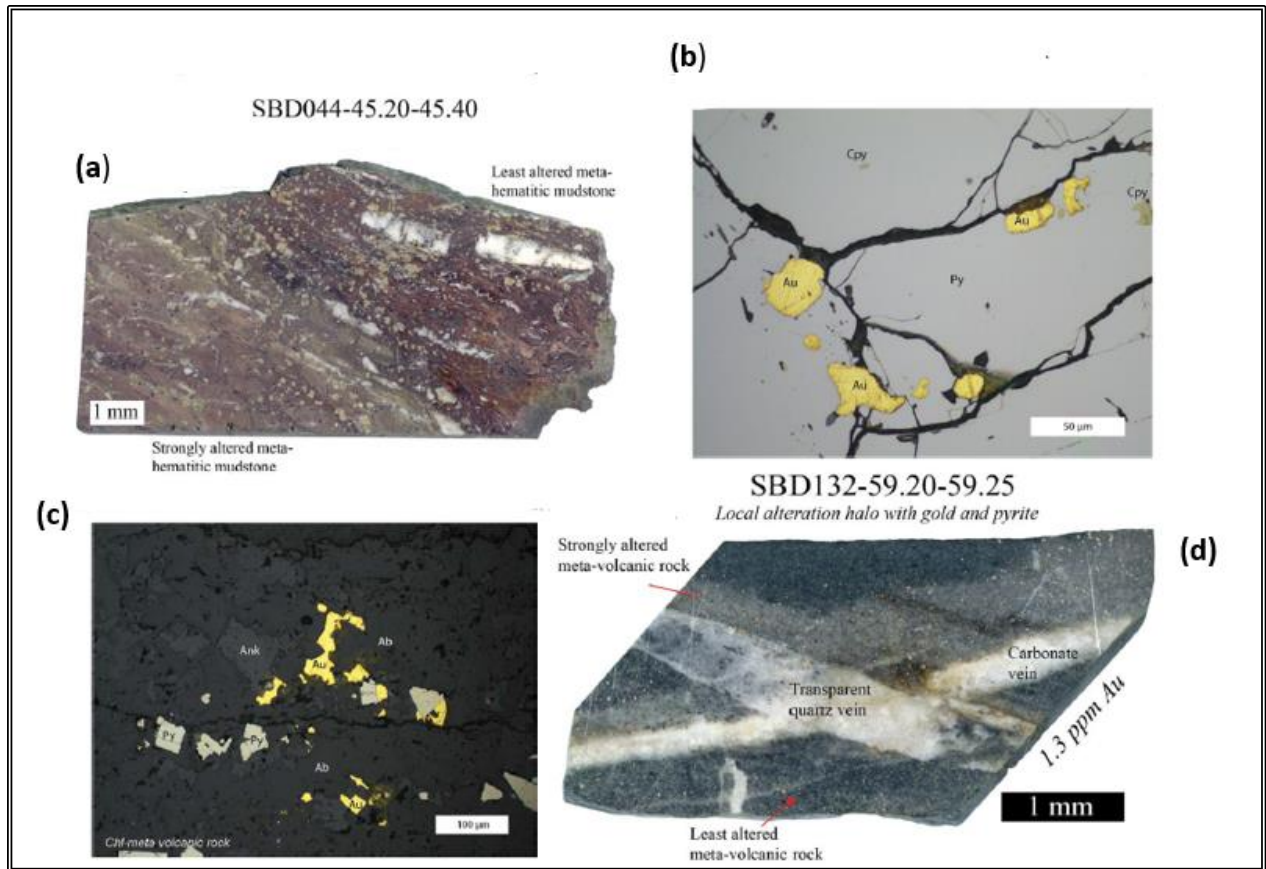


Figure 5.14: (a,b) Host rock and photomicrograph showing native Au in strongly altered meta-hematitic mudstone, (c, d) Host rock and photomicrograph native Au along the contact between the vein and host rock.

5.5 DISCUSSION

The μ XRF image shows many variations in the elemental composition of veins and host rock, which are not apparent in the true-color image. It may be useful in economic geology research and exploration when the stages of vein composition can provide vectors towards mineralization, associated with hydrothermal-type mineralization. Micro-XRF composite chemical maps can also indicate mineralogy such as albite, and pyrite (Figs. 5.10 and 5.12).

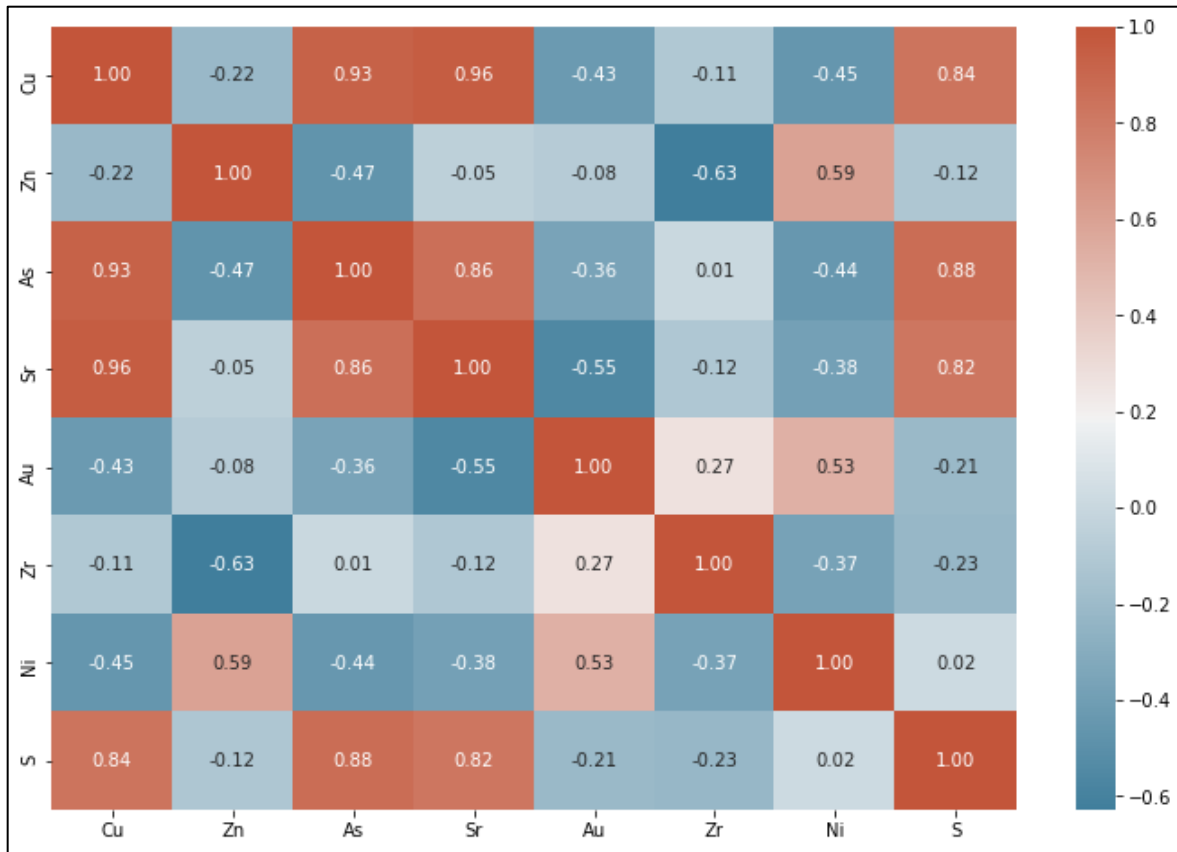


Figure 5.15: Correlation heat map of elements from strongly altered zones.

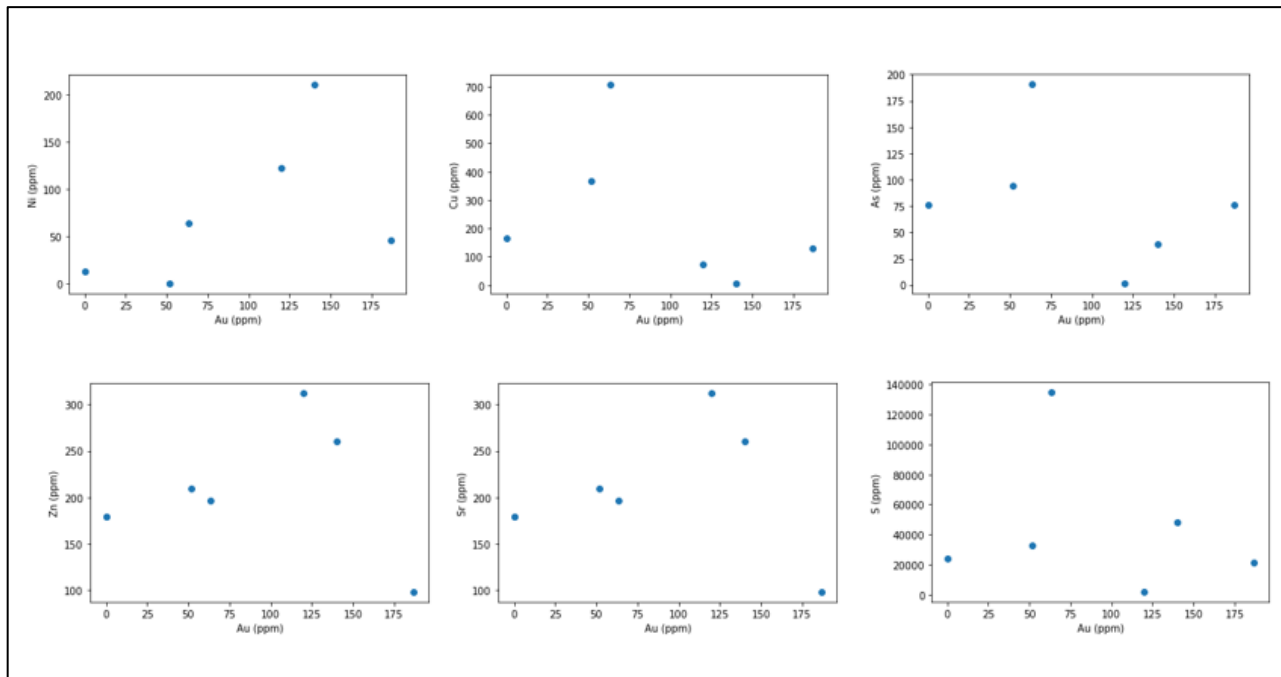


Figure 5.16: An analysis of the correlation between Au and other elements. The samples were taken from a zone of the strongly altered host rocks.

From the results, most of the strongly altered rocks, Ca, Mg, and Mn enriched in (carbonatization), Na and Si (albitization), S (pyritization), Sr (Sr-Al phosphate mineral, albite, and carbonates), and depleted in Al, Ti, Fe, and K as compared to the least altered host rocks, except for hematitic mudstone (Fig. 5.17). Pyrite is the most abundant sulfide, and the occurrence of gold is strongly related to sulfidation and albitization of host rocks and significantly higher in Fe-rich host rocks such as meta-hematitic mudstone and metavolcanic rock. In the Salu Bulu prospect, carbonate and albite alteration was probably caused by CO₂-bearing sodic mineralizing fluid, as confirmed by the albite alterations along the Stage 2 veins. A reaction between CO₂-bearing fluid and host rocks led to carbonate alteration. Hydrothermal activity added CaO and Na₂O to the altered host rock, resulting in carbonatization and albitization, respectively, while potassic alteration is absent (Fig. 5.18).

Ni content ranges from 6.64 to 230.5 ppm in the unaltered host rocks. This indicates that meta-mudstone and meta-volcanic rocks were likely to be the source of Ni in the ore-forming fluid that might have leached during hydrothermal activities.

Ni in intensely altered host rocks and the positive correlation between Au and Ni in the same rocks was probably caused by the deep circulation of meteoric water. A deep circulation of meteoric water might have enriched it with Na to form an albite alteration. In unaltered host rocks, Fe₂O₃ content ranges from 0.85% to 13.42 wt%. It is thought that the mafic host rocks interacted with the ore-forming fluid, causing the sulfidation and carbonation of the wall rock. As a result of this process, ankerite was the dominant carbonate mineral. In the ore-forming fluid, sulfur was consumed by the wall rock to form pyrite (Wilkinson, 2001; Phillips & Powell, 2010). During the formation of the albite-carbonate alteration in the Salu Bulu prospect, Au dissolves as an Au(HS)₂ complex in a near-neutral alkaline ore-forming fluid (Phillips & Powell,

2010). The sulfidation of wall rocks produced pyrite, destabilizing $\text{Au}(\text{HS})_2$ complexes in the ore forming fluid and precipitating native gold (Reed, 1997; Wilkinson, 2001; Phillips & Powell, 2010). A micro-inclusion of Au in pyrite suggests that Pyrite formed earlier and precipitated Au. Moreover, fluid boiling is a possible mechanism for precipitating native Au in the Salu Bulu prospect.

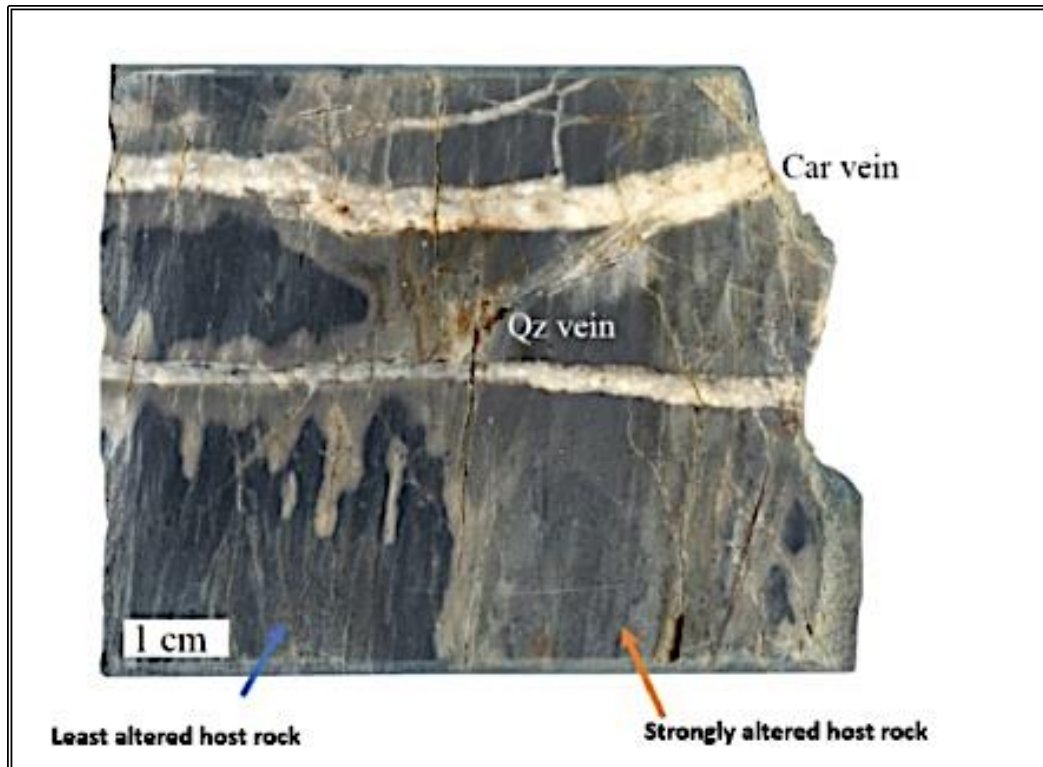


Figure 5.17: Photograph of carbonaceous mudstone representing zones of least and most altered as an example

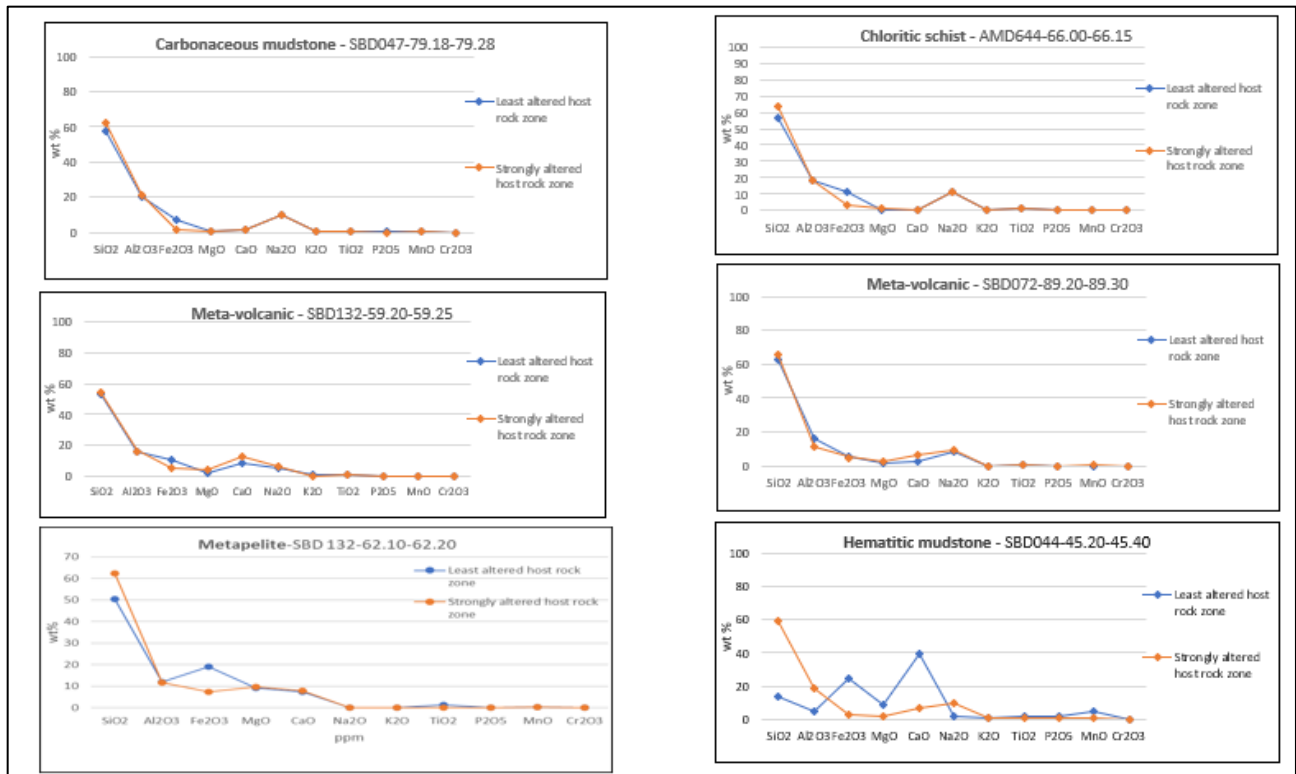


Figure 5.18: Major elements oxide of least altered and intensely altered host rocks for six samples.

Chapter 6: Hydrothermal alteration in a hot crater late, Adatarata volcano, Japan

Adatarata Volcano is a quaternary composite volcano located on north-east Japan Arc, northeastern Fukushima (Fig. 6.1). The western side of the volcanic edifice is dissected by the Iogawa River exposing an extensive zone of volcanic-hydrothermal alteration like that associated with epithermal gold deposits (e.g., Rodalquilar, see Chapter 3). This study was conducted in collaboration with Dr. Takumi Imura, who is investigating the evolution of hydrothermal alteration within Adatarata volcano and the potential for precious-metal mineralization in the exposed altered rocks of Iogawa valley and Numanotaira crater. The following paragraphs are borrowed from a collaborative manuscript in preparation.



Figure 6.1: (a) Location of Adatarata Volcano; (b) view of Numanotaira crater looking southeast. The crater lake sediments studied here are the light gray units at the base and in the margins of the Numanotaira crater.

Bulk-rock XRD analyses of the altered rocks in the western summit of Adatarata volcano show a change in mineral assemblage with elevation and with proximity to Numanotaira crater.

Combined with geological relations, the alteration lithology is classified into four domains which occur from east to west and from lower to higher elevation (Fig. 6.2).

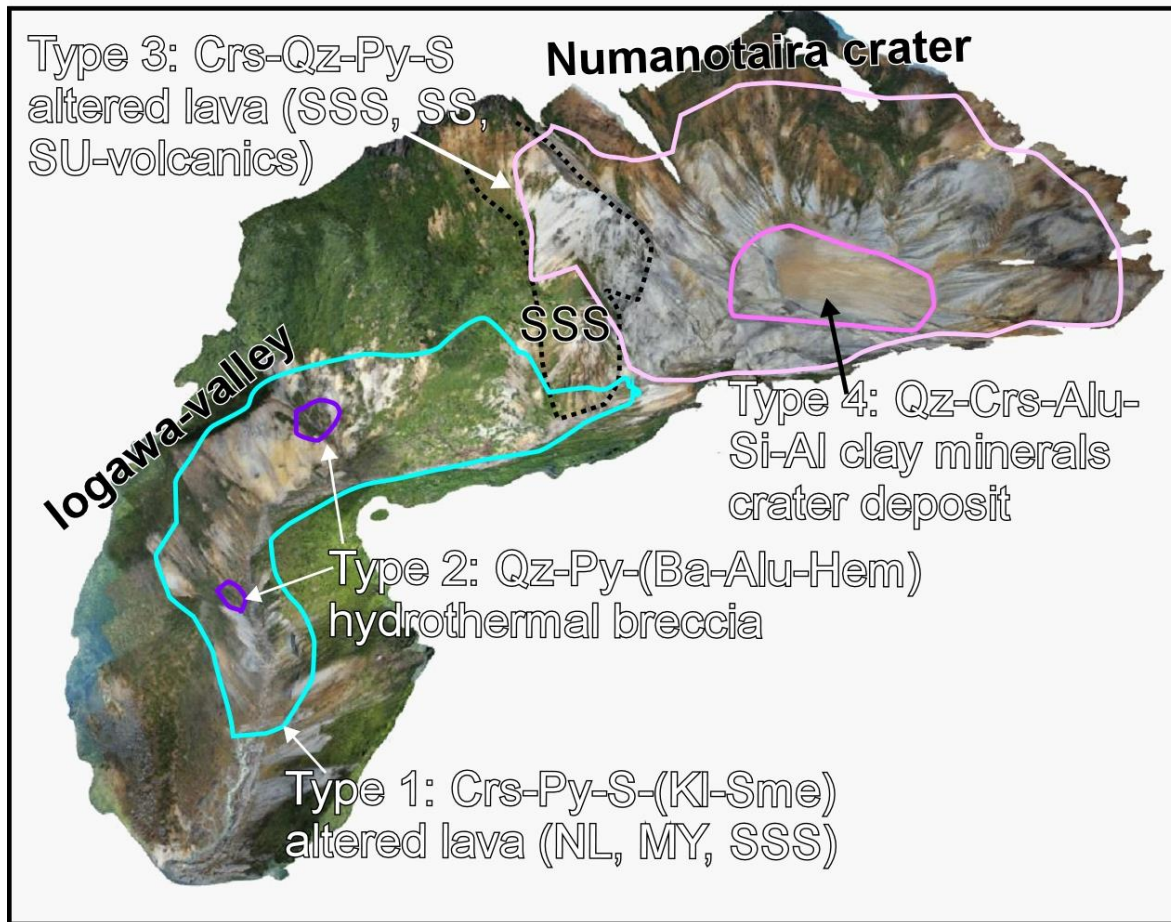


Figure 6.2: Types of hydrothermal alteration of alteration at the Numanotaira crater of Adatara volcano (see text for mineral abbreviations; Imura et al., in preparation)

The entire valley of Iogawa River is occupied by cristobalite-pyrite-native sulfur (kaolinite-smectite) altered lava along the valley between elevations of 1200 m a.s.l. and 1390 m a.s.l. (Type 1, Steam-heated origin), developing in lava rocks that erupted around 70 ka. Within the Type 1 alteration there are smaller zones consisting of quartz-pyrite (barite-alunite-hematite) hydrothermal breccia (Type 2, Magmatic-hydrothermal origin). The Type 1 and Type 3 were spatially divided by partially altered lava erupted between 70 and 50 ka. Above an elevation of

1420 m a.s.l. around Numanotaira crater (Fig. 6.2), Type 3 (Steam-heated origin) widely occurs as cristobalite-quartz-pyrite-native sulfur altered lava comprised the inner wall of the crater. The Type 3 alteration is distributed in the inner wall of Numanotaira crater, which consists of the volcanic rocks produced between 200 ka and 50 ka. Quartz-cristobalite-alunite-Si-Al-clay minerals crater deposit (Type 4, Magmatic-hydrothermal origin) occurs inside the Numanotaira crater (Fig. 6.3) and covers the lithology of Type 3.

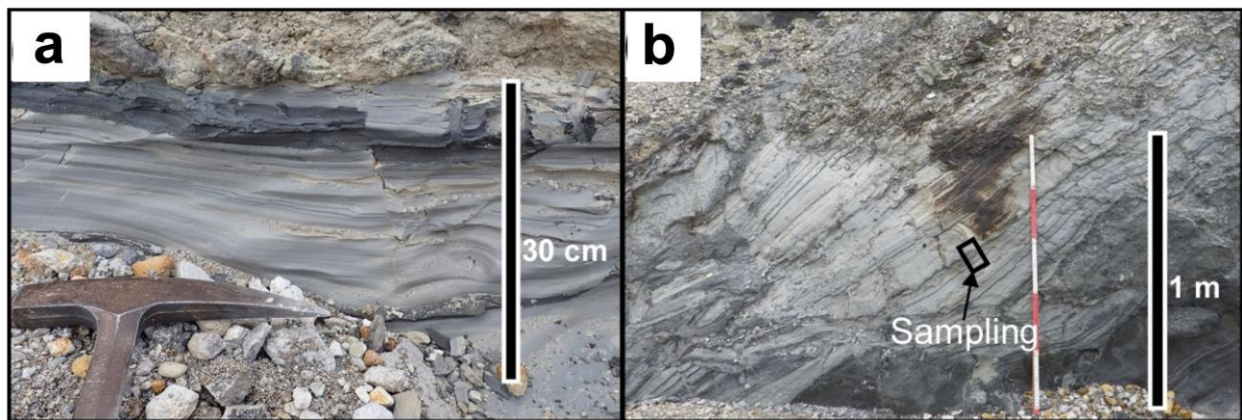


Figure 6.3: Field photographs of samples studied. (a) Large-platy block of the layered clay sediment in Locality. 16 of Numanotaira crater. (b): Large block of layered clay sediment in terrace deposit at Locality. 15 (Imura et al., in preparation).

The stratigraphic and lithologic relations show that Type 1 and 2 were derived from past magmatic-hydrothermal system presented in Iogawa-valley between 1200-1390 m a.s.l., while Type 3 and 4 above 1420 m a.s.l. are associated with the younger and recent magmatic-hydrothermal system around the Numanotaira crater. Thus, the magmatic-hydrothermal alteration center of alteration moved from the west (Iogawa River valley) to the west (Numanotaira crater), corresponding to the movement of the eruptive center and hydrothermal/phreatic or phreatomagmatic/magmatic-hydrothermal eruptions.

6.3. SAMPLES

An Adatara crater lake sediment sample (Fig. 6.4), was analyzed to test Micro-XRF's ability to process very fine grains of less than 1mm. An analysis was performed under beam conditions of 50 kV and 600 μ A. The measurement was performed with a step size of 30 μ m and pixel time of 30ms, resulting in a total measurement time of 17hr.

Table 6.1: Analytical conditions for Adatara crater lake sediment.

Sample ID	Pixel spacing	Dwell Time	Map time	Detectors
20180815-6A	30 μ m	30 ms	~17 hrs	1 SDD

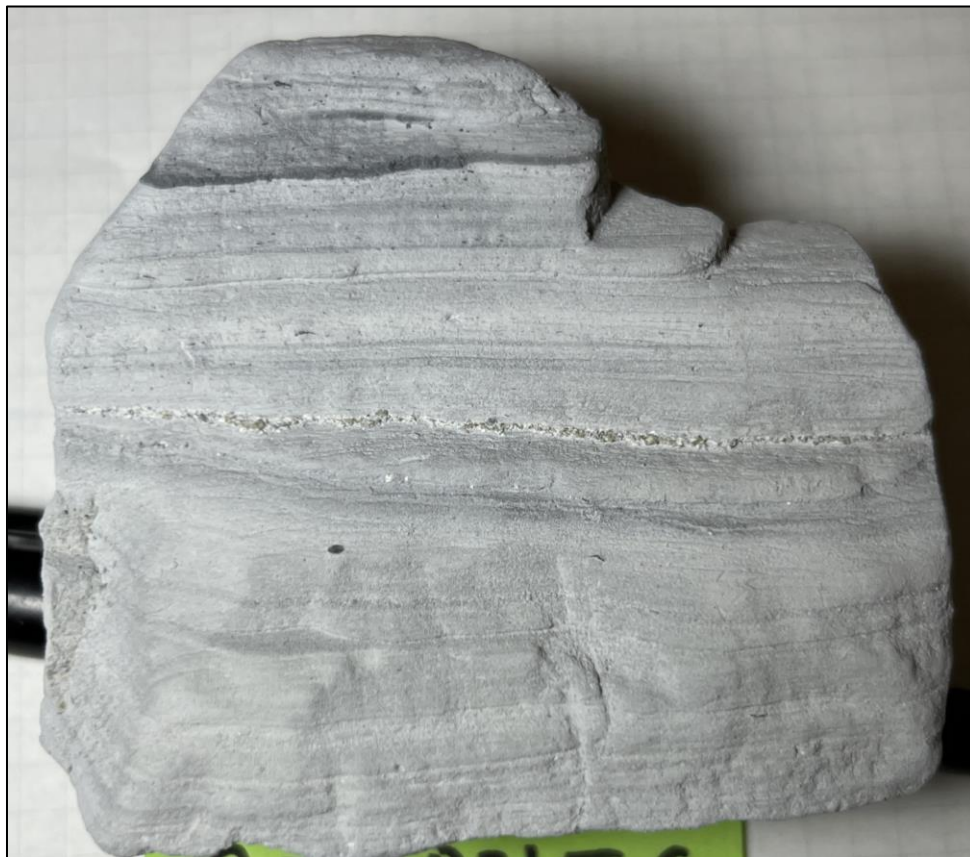
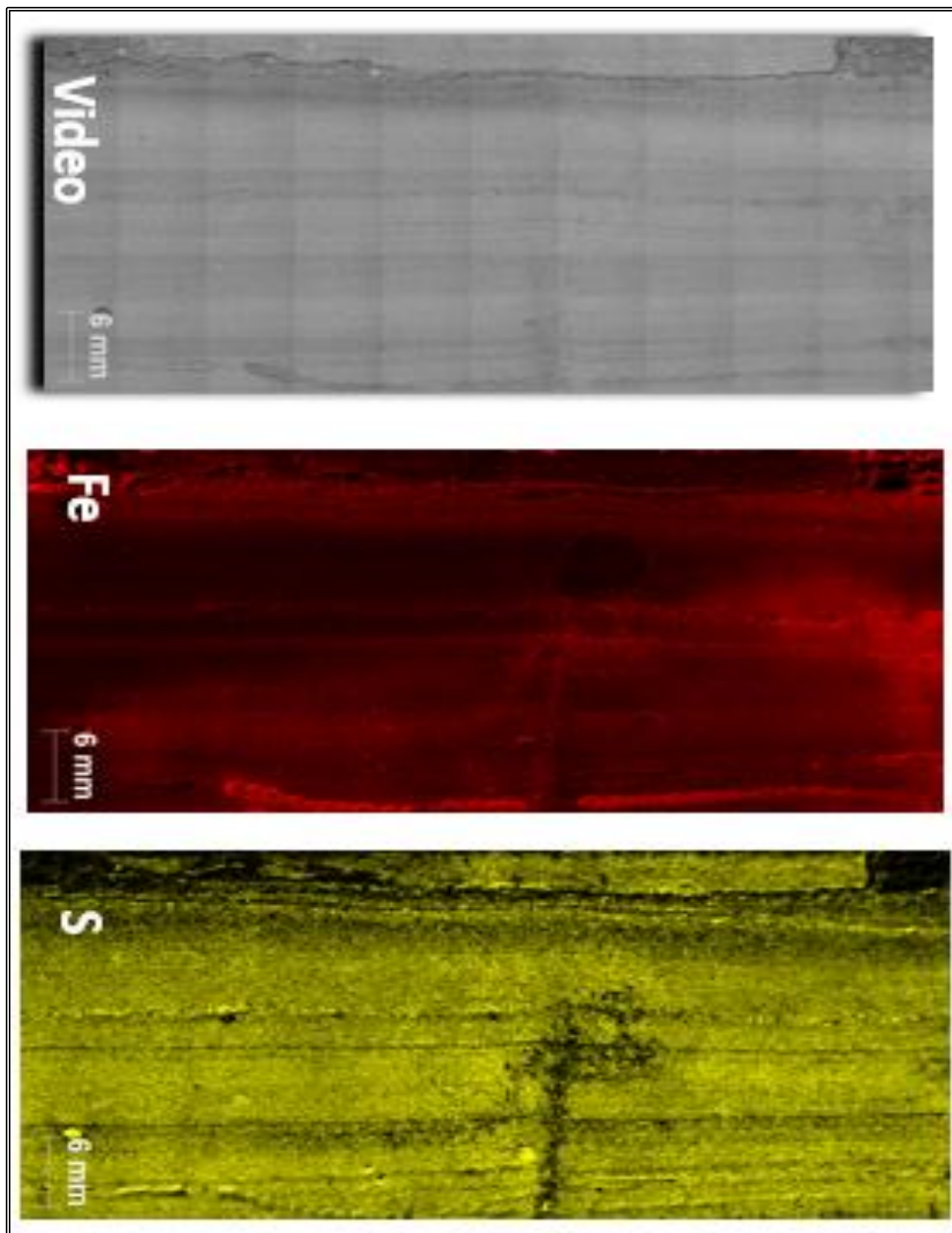


Figure 6.4: Sample of crater lake sediments from Adatara volcano (20180815-6).

6.4. RESULTS AND DISCUSSION

Geological materials' composition, grain size, texture, and surface roughness are incredibly diverse. The spatial scale of these features can be highly variable, which affects the XRF analysis. According to the Adatara elemental maps produced with the uXRF, the main minerals are native sulfur (S), iron (Fe), silica (Si), potassium (K), and calcium (Ca). Since the grain size is so fine, it isn't easy to see much (6.5).



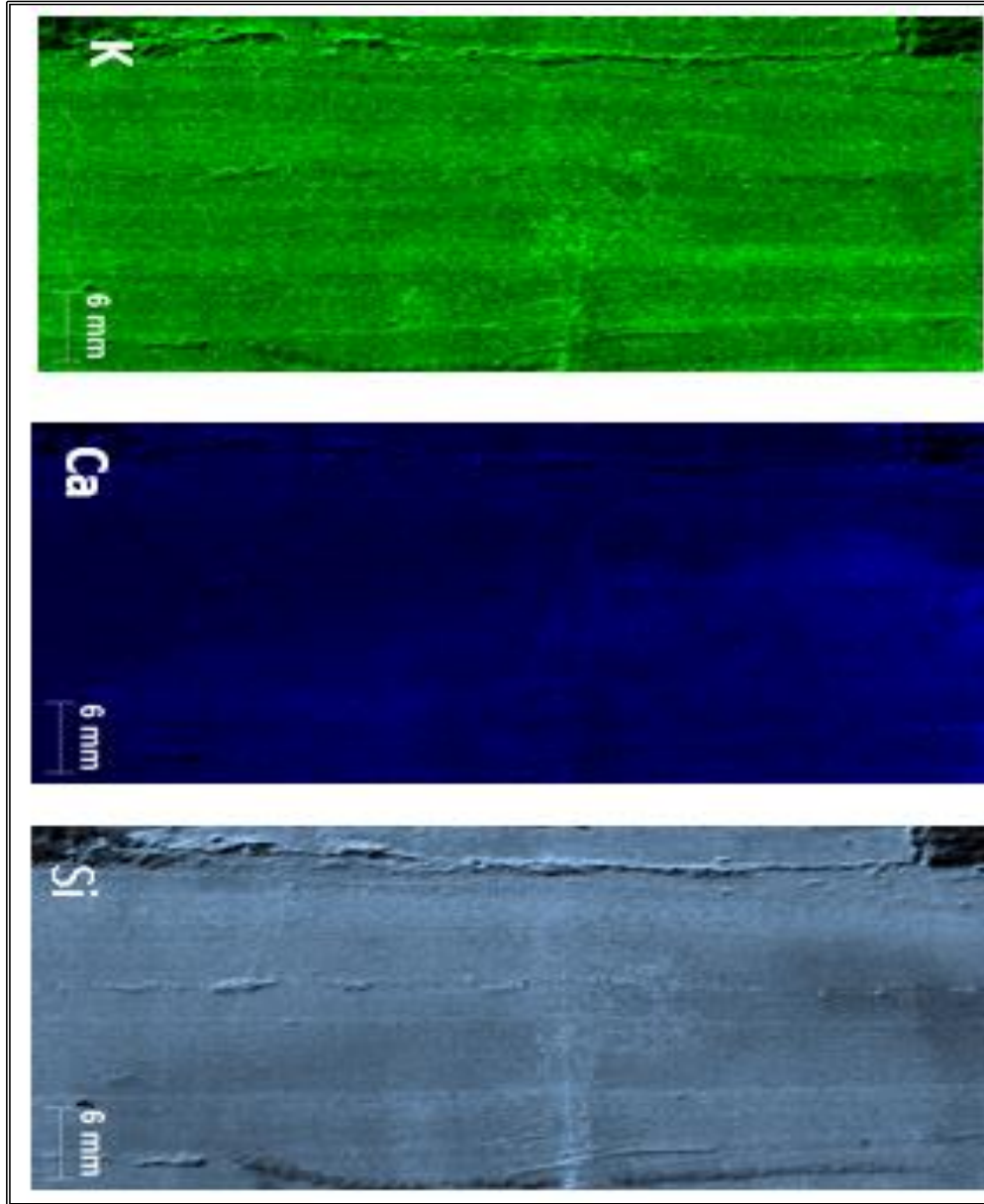


Figure 6.5: Micro-XRF elemental images of Adatara crater lake sediment: Fe, S (previous page), K, Ca and Si (above)

Chapter 7: Conclusions

- Micro-XRF (μ XRF) can be extremely useful to better understand economic geology questions like the origin and evolution of an ore deposit.
- It applies to geoscience problems.
- Micro-XRF is more effectively applied when the sample:
 - is heterogeneous
 - has a range of atomic weights
 - has a grain size not too small ($<100 \mu\text{m}$ not ideal)

References

Annels, A.E. (1974). Some aspects of the stratiform ore deposits of the Zambian Copperbelt and their genetic significance. In: Bartholomé, P. (Ed.) *Gisements Stratiformes et Provinces Cuprifères*. Liège: Centenaire Société Géologique de Belgique, 235–254.

Arribas Rosado, A. and Arribas Moreno, A. (2011). The Rodalquilar caldera complex and associated gold-silver and alunite deposits - Field-trip guide to the Rodalquilar deposits. In Ortiz, J.E, Puche, O., Rábano, I., and Mazadiego, L.F. (Eds.) 2011. *History of Research in Mineral Resources*. Cuadernos del Museo Geominero, 13, p. 1059-1070. Instituto Geológico y Minero de España, Madrid.

Arribas, A. Jr., Cunningham, C. G., Rytuba, J. J., Rye, R. O., Kelly, W. C., McKee, E. H., Podwysocky, M. H., and Tosdal, R. M. (1995) Geology, geochronology, fluid inclusions, and isotope geochemistry of the Rodalquilar Au-alunite deposit, Spain. *Economic Geology*, 90, 795-822.

Barker, R. D., Barker, S. L., Wilson, S. A., & Stock, E. D. (2021). Quantitative mineral mapping of drill core surfaces I: a method for μ XRF mineral calculation and mapping of hydrothermally altered, fine-grained sedimentary rocks from a Carlin-type gold deposit. *Economic Geology*, 116(4), 803-819.

Bergman, S. C., Coffield, D. Q., Talbot, J. P. and Garrard, R. A. (1996) Tertiary tectonic and magmatic evolution of Western Sulawesi and the Makassar Strait, Indonesia: Evidence for a Miocene continent-continent collision.

Berner, R.A. (1964). Iron sulfides formed from aqueous solution at low temperatures

and atmospheric pressure. *Journal Geology*, 72, 293–306.

Berner, R.A. (1970). Sedimentary pyrite formation. *American Journal of Science*, 268, 1–23.

Borg, G. (1995). Metallogenesis of Neoproterozoic basins in Namibia and Botswana. *Communications of the Geological Survey of Namibia*, 10, 109–119.

Borg, G. and Maiden, K.J. (1986). Stratabound copper-silver-gold mineralization of late proterozoic age along the margin of the Kalahari Craton in Southwest Africa/Namibia and Botswana. *Canadian Mineralogist*, 24, 178.

Borg, G. and Maiden, K.J. (1987). Basalt alteration and its relation to middle proterozoic stratabound copper-silver-gold deposits along the margin of the Kalahari Craton in Southwest Africa/- Namibia and Botswana, in: Pharaoh, T.C., Beckinsale, R.D., and Rickards, D.T., (Eds.), *geochemistry and mineralization of proterozoic volcanic suites*. Geological Society of London Special Publication, 33, 347–354.

Borg, G. and Maiden, K.J. (1989). The middle proterozoic Kalahari Copper Belt of Namibia and Botswana. In: Boyle, R.W., Brown, A.C., Jefferson, C.W., Jowett, E.C. and Kirkham, R.V. (Eds.) *Sediment-Hosted Stratiform Copper Deposits*, Vol. 36. Ottawa, Canada: Geological Association of Canada Special Paper, 524–540.

Bright, D. S., & Newbury, D. E. (2004). Maximum pixel spectrum: a new tool for detecting and recovering rare, unanticipated features from spectrum image data cubes: *Journal of Microscopy*, 216-2, 186-193.

Bruker Webpage; <http://www.bruker-axs.com>

Carney, J.N., Aldiss, D.T. and Lock, N.P. (1994). The geology of Botswana. Botswana Geological Survey Bulletin, 37, 113.

Croudace, I. W., & Rothwell, R. G. (Eds.). (2015). Micro-XRF Studies of Sediment Cores: Applications of a non-destructive tool for the environmental sciences (Vol. 17, p. 668). Dordrecht: Springer.

Djuri, S., & Bachri, S. (1998). Sukindo, Geological Map of the Majene and the Western Part of Palopo Sheets, Sulawesi, Scale 1: 250000.

Elam, W., Shen, R., Scruggs, B., and Nicolosi, J. (2004) Accuracy of standardless FP analysis of bulk and thin film samples using a new atomic database: *Advances in X-Ray Analysis*, vol. 47, p. 104–109.

Elburg, M., & Foden, J. (1999). Sources for magmatism in Central Sulawesi: geochemical and Sr–Nd–Pb isotopic constraints. *Chemical Geology*, vol. 156, 67-93.

Fritz, J., Tagle, R., Ashworth, L., Schmitt, R. T., Hofmann, A., Luais, B., ... & Koeberl, C. (2016). Nondestructive spectroscopic and petrochemical investigations of Paleoproterozoic spherule layers from the ICDP drill core BARB 5, Barberton Mountain Land, South Africa. *Meteoritics & Planetary Science*, 51(12), 2441-2458.

Flude, S., Haschke, M., Storey, M., & Harvey, J. (2017). Application of benchtop micro-XRF to geological materials. *Mineralogical Magazine*, 81(4), 923-948.

Gottlieb, P. (2008, September). The revolutionary impact of automated mineralogy on mining and mineral processing. In the XXIV International Mineral Processing Congress (pp.

165-174).

Genna, D., Gaboury, D., Moore, L., & Mueller, W. U. (2011). Use of micro-XRF chemical analysis for mapping volcanogenic massive sulfide related hydrothermal alteration: Application to the subaqueous felsic dome-flow complex of the Cap d'Ours section, Glenwood rhyolite, Rouyn-Noranda, Québec, Canada. *Journal of Geochemical Exploration*, 108(2), 131-142.

Gorman, A. (2013). Constraining a genetic model for copper-silver mineralization in the Kalahari Copperbelt, Botswana: Mineralogy, Geochemistry and Structure. MGeol. thesis, University of Leicester, England.

Gray, D.R., Foster, D.A., Meert, J.G., Goscombe, B.D., Armstrong, R., Trouw, R.A. and Passchier, C.W. (2008). A Damara orogen perspective on the assembly of southwestern Gondwana. *Geological Society of London Special Publications*, 294, 257–278.

Hall, W. S. (2013) Geology and paragenesis of the Boseto copper deposits, Kalahari Copperbelt, Northwest Botswana: M.Sc. Thesis, Golden, Colorado, Colorado School of Mines, 146.

Hall, W. S. (2017) Geochronology, magnetic lithostratigraphy, and the tectonostratigraphic Evolution of the Late Meso- to Neoproterozoic Ghanzi Basin in Botswana and Namibia, and implications for copper-silver mineralization in the Kalahari Copperbelt. Ph.D. dissertation, Golden, Colorado, Colorado School of Mines, 62.

Hall, W.S., Hitzman, M.W., Kuiper, Y.D., Kylander-Clark, A.R.C., Holm Denoma, C.S., Moscati, R.J., Plink-Bjorklund, P. and Enders, M.S. (2018). Igneous and detrital zircon

U-Pb and Lu-Hf geochronology of the late Meso- to Neoproterozoic Northwest Botswana rift: maximum depositional age and provenance of the Ghanzi group, Kalahari Copperbelt, Botswana, and Namibia. *Precambrian Research*, 318, 133–155.

Hall, W.S., Knight, C., Catterall, D.J., Augenstein, C., Davies, B.M., Deane, J., Muyoba, B., Disang, O., Emsbo, P., Li, Y., Enders, M. S. and Hitzman, M.W. (2018). Regional-to-deposit-scale geologic controls on copper-silver mineralization in the Kalahari Copperbelt, Botswana. *Society of Economic Geologists Special Publication*, 21, 207–236

Hall, W.S., Stein, H.J., Kylander-Clark, A.R.C., Hitzman, M.W., Kuiper, Y.D., Knight, C. and Enders, M.S. (2021). Diagenetic and epigenetic mineralizing events in the Kalahari Copperbelt, Botswana: evidence from re-Os sulfide dating and U-Th-Pb xenotime geochronology. *Economic Geology*, 116, 863–881.

Hamilton, W. (1979). Tectonic of the Indonesia region. United States Geological Survey Professional Paper, 1078, 345p.

Harahap BH (2014). Metallogenic Map of Indonesia. Geological Agency, Indonesia

Kamunzu, A.B., Akanyang, P., Mapeo, R.B.M., Modie, B.N. and Wendorff, M. (1998). Geochemistry and tectonic significance of the mesoproterozoic Kgwebe metavolcanic rocks in Northwest Botswana: implications for the evolution of the Kibaran Namaqua-Natal Belt. *Geological Magazine*, 135, 669–683.

Kamunzu, A.B., Armstrong, R.A., Modisi, M.P. and Mapeo, R.B. M. (2000). Ion microprobe U-Pb ages on detrital zircon grains from the Ghanzi group: implications for the identification of a Kibaran-age crust in Northwest Botswana. *Journal of African Earth Sciences*,

30, 579–587.

Kanngießer, B. (2003). Quantification procedures in micro X-ray fluorescence analysis. *Spectrochimica Acta Part B: Atomic Spectroscopy*, 58(4), 609-614.

Katili, J. A. (1978) Past and present geotectonic position of Sulawesi, Indonesia. *Tectonophysics*, 45, 289–322.

Kelepile, T., Betsi, T.B. and Shemang, E. (2020). Metal sources and mineralizing fluids characteristics and evolution of the Khoemacau sediment-hosted Cu-Ag deposits, in the Ghanzi- Chobe belt portion of the Kalahari Copper Belt. *Ore Geology Reviews*, 122, 103559.

Kelepile, T., Bineli Betsi, T., Franchi, F., Shemang, E. and Suh, C.E. (2017). Provenance and tectonic setting of the neoproterozoic clastic rocks hosting the Banana zone Cu-Ag mineralisation, Northwest Botswana. *Journal of African Earth Sciences*, 129, 853–869.

Key, R.M. and Ayres, N. (2000). The 1998 edition of the national geological map of Botswana. *Journal of African Earth Sciences*, 30, 427–451.

Key, R.M. and Rundle, C.C. (1981). The regional significance of new isotopic ages from Precambrian windows through the “Kalahari beds” in North-Western Botswana. *Transactions of the Geological Society of South Africa*, 84, 51–66.

Lehmann, J., Master, S., Rankin, W., Milani, L., Kinnaird, J.A., Nydenov, K.A., Saalman, K. and Kumar, M. (2015). Regional aeromagnetic and stratigraphic correlations of the Kalahari Copperbelt in Namibia and Botswana. *Ore Geology Reviews*, 71, 169–190.

Litherland, M. (1982). The geology of the area around Mamuno and Kalkfontein,

Ghanzi District, Botswana. Geological Survey of Botswana District Memoir, 4, 145.

Maiden, K.J. and Borg, G. (2011). The Kalahari Copperbelt in Central Namibia: controls on copper mineralization. *Society of Economic Geologists Newsletter*, 87, 14–19.

Maulana, A., Imai, A., van Leeuwen, T., Watanabe, K., (2016). Origin and geodynamic setting of late Cenozoic granitoids in Sulawesi, Indonesia. *J. Asian Earth Sci.*, 124, 102–125.

Meixner, H.M., 1983, Geological framework of western Botswana and adjacent areas: Geological compilation map, no. 1, Botswana Geological Survey, scale 1:2,000,000.

Metcalf, I. (2011). Paleozoic—Mesozoic history of SE Asia. In Hall, R., Cottam, M. A. and Wilson, M. E. J. (eds.) *The SE Asian gateway: History and tectonics of the Australia-Asia collision*, The Geological Society of London, Special Publication, The Geological Society, London, No. 355, 7–36.

Miller, R.M. (2008). *The Geology of Namibia*. Windhoek: Geological Survey of Namibia.

Modie, B.N. (1996). Depositional environments of the meso- to neoproterozoic Ghanzi-Chobe zone, northwest Botswana. *Journal of African Earth Sciences*, 22, 255–268.

Modie, B.N. (2000). Geology and mineralization in the meso- to neoproterozoic Ghanzi-Chobe zone, northwest Botswana. *Journal of Africa Earth Sciences*, 30, 467–474.

Morgan, K. (2013). Developing genetic models for copper-silver mineralization in the Kalahari Copperbelt, Botswana: source and evolution of fluids. MGeol. thesis, University of Leicester, England.

Phillips, G. N., and Powell, R. (2010) Formation of gold deposits: A metamorphic devolatilization model. *J. Metamor. Geol.*, 28, 689–718.

Piestrýnski, A., Wendorff, M., Letsholo, M. and Mackay, W. (2015). Platinum-group minerals in the neoproterozoic stratabound copper-silver mineralization, the Kalahari Copperbelt, northwestern Botswana. *South African Journal of Geology*, 118, 275–284.

Potter, N., & Brand, N. (2019). Application of micro-XRF to characterise diamond drill-core from lithium-cesium-tantalum pegmatites. *ASEG Extended Abstracts*, 2019(1), 1-4.

Priadi, B., Polve, M., Maury, R. C., Bellon, H., Soeria- Atmadja, R., Joron, J. L. and Cotten, J. (1994). Tertiary and quaternary magmatism in Central Sulawesi: Chronological and petrological constraints. *J. Southeast Asian Earth Sci.*, 9, 81–93.

Querubin CD & Walter S (2012). Geology and Mineralization of Awak Mas: A Sedimentary Hosted Gold Deposit, South Sulawesi, Indonesia. *Majalah Geologi Indonesia* 27:69-85.

Ramokate, L.V., Mapeo, R.M.M., Corfu, F. and Kampunzu, A.B. (2000) Proterozoic geology and regional correlation of the Ghanzi-Makunda area, western Botswana. *Journal of African Earth Science*, 30, 453–466.

Reed, M. H. (1997). Hydrothermal alteration and its relationship to ore fluid composition. *Geochemistry of hydrothermal ore deposits*, 303-365.

Reeves, C. V. and Hutchins, D.G. (1982). A progress report on the geophysical exploration of the Kalahari in Botswana. *Geoexploration*, 20, 209–224.

Ruxton, P.A. (1986). Sedimentology, isotopic signature and ore genesis of the Klein Aub copper mine, south West Africa/Namibia. In: Anhaeusser, C.A. and Maske, S. (Eds.) Mineral Deposits of Southern Africa, Vol. 2. Johannesburg, South Africa: Geological Society of South Africa, pp. 1725–1738.

Ruxton, P.A. and Clemmey, H. (1986). Late Proterozoic stratabound red bed-copper deposits of the Witvlei area, south West Africa/- Namibia, in Anhaeusser C.A., and Maske, S., eds., mineral deposits of southern Africa. Geological Society of South Africa, 2, 1739–1754.

Schwartz, M.O., Akanyang, P., Trippler, K. and Ngwisanyi, T.H. (1995). The sediment hosted Ngwako pan copper deposit, Botswana. *Economic Geology*, 90, 1118–1147.

Schieber, J. (1999). Microbial mats in terrigenous clastics; the challenge of identification in the rock record. *Palaios*, 14(1), 3-12.

Schwartz, M.O., Kwok, Y.Y., Davis, D.W. and Akanyang, P. (1996). Geology, geochronology, and regional correlations of the Ghanzi ridge, Botswana. *South African Journal of Geology*, 99, 245–250.

Shephard, G. (2014). Origin and fluid sources of Kalahari Copperbelt mineralization, Botswana: an in-depth study of Zone 5 and 6 of the Khoemacau copper-silver exploration project MGeol. Thesis, University of Leicester, Leicester, England.

Sherman, J. (1955). The theoretical derivation of fluorescent X-ray intensities from mixtures. *Spectrochimica acta*, 7, 283-306.

Sillitoe, R.H., Perello, J. and Garcia, A. (2010). Sulphide-bearing veinlets throughout the stratiform mineralisation of the central African Copperbelt: temporal and genetic

implications. *Economic Geology*, 105, 1361–1368.

Sweeney, M.A. (1987) The use of fluid inclusion geochemistry in determining the origin of veins, examples from the Zambian copper-belt. *Journal of Geological Society of Zambia*, 1, 18–28.

Walraven, F. and Borg, G. (1992). Lead isotopic signatures at the Klein Aub mine, Namibia: implications for mineralization models. *Mineralium Deposita*, 27, 115–121.

Walsh, A.M. (2014). Origin and fluid sources of Kalahari Copperbelt mineralization, Botswana: regional variations in mineralogy, isotopic signatures and fluid characteristics at the Khoemacau Cu-Ag project. Geol. Thesis, University of Leicester, Leicester, England.

Wang, H., Treble, P., Baker, A., Rich, A. M., Bhattacharyya, S., Oriani, F., ... & Marjo, C. E. (2022). Sulfur variations in annually layered stalagmites using benchtop micro-XRF. *Spectrochimica Acta Part B: Atomic Spectroscopy*, 189, 106366.

White, L. T., Hall, R., Armstrong, R. A., Barber, A. J., Fadel, M. B., Baxter, A., Wakita, K., Manning, C. and Soesilo, J. (2017). The geological history of the Latimojong region of western Sulawesi, Indonesia. *J. Asian Earth Sci.*, 138, 72–91.

Wilkinson, J. J. (2001) Fluid inclusions in hydrothermal ore deposits. *Lithos*, 55, 229–272.

Xu, J., Zhu, S. Y., Luo, T. Y., Zhou, W., & Li, Y. L. (2015). Uranium mineralization and its radioactive decay-induced carbonization in a black shale-hosted polymetallic sulfide ore layer, southwest China. *Economic Geology*, 110(6), 1643-1652.

MICRO-XRF USER MANUAL

A Guide to Using and Operating the Bruker M4 Tornado



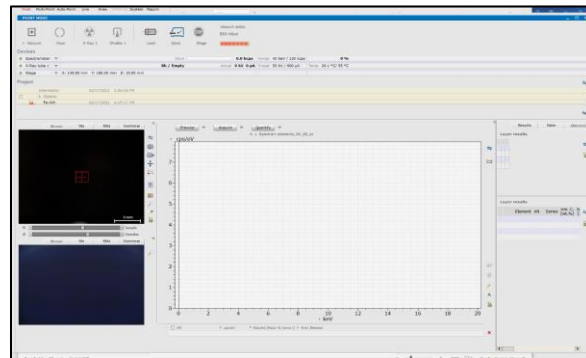
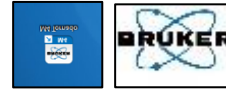
Table of Contents (Page # and Contents)

- Pg. A1. Start-up operation and login.
- Pg. A2. A step-by step guide to sample analysis and map generation
- Pg. A3. Creation of a mosaic image
- Pg. A6. Maximum pixel spectrum
- Pg. A7. Generating heat maps
- Pg. A7. Analyzing an object on the sample surface
- Pg. A8. Energy calibration

The University of Texas at El Paso
Department of Earth, Environmental, and Resource Sciences
Hannah Buamono

1. Start-up operation and Login

1. **Slight check** of the mains supplies for the spectrometer, pump, control unit
2. **Switch the key** on the frontal panel and turn the **Power Button ON**
3. **Switch ON** the control unit
4. **Click on the measuring software Icon on the Desktop.**
5. **Login** comes with a start-up screen



2. A step-by-step guide to sample analysis and map generation

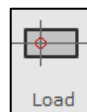
1. **Click Eject icon** to open the sample chamber



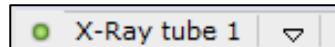
2. **Level the sample in the box of beads** to achieve a horizontal surface and place it on the stage in reference to the X-Y-Z axis



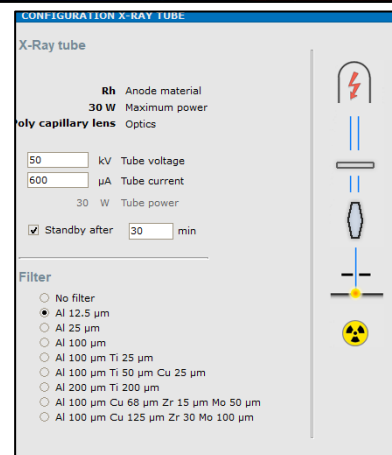
3. **Click on load** to move the stage to measure the position



4. **Turn the X-ray tube on** by clicking on the X-Ray 1 display on the main menu (it will turn yellow)



5. **Click on the downward-facing arrow** and set the tube voltage and current to **(50kv, 600 μ A)** and tick "Standby after 30 mins"

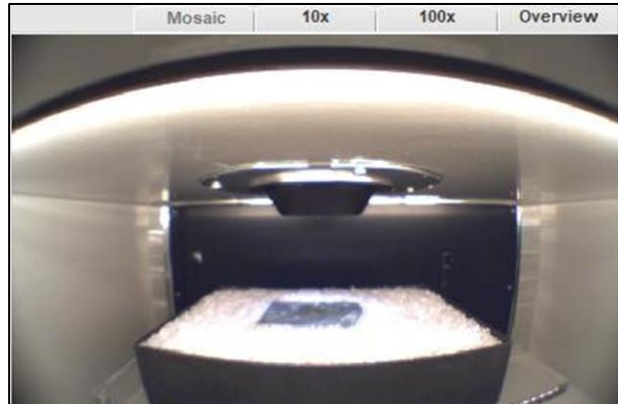
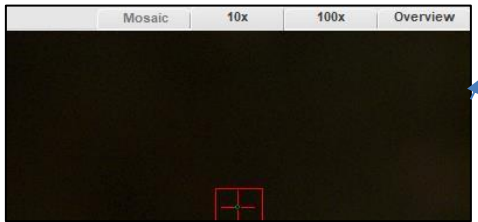


6. **Select a filter**, such as Al 12.5 μ m (for lighter elements)
7. **Make sure that the tube conditions** on the main menu are set to (50kv and 600 μ A) before starting the analysis.

8. **Click on the vacuum button** on the user interface or the main menu to pump the vacuum to the standard operating pressure of 20 mbar. The analysis is best performed in a vacuum.
9. **Click on the point mode** if in a different mode.



For fine positioning of the measurement spot, we use the camera below, with a field of view of approximately 1.4 mm x 1.1 mm.



For an overview of the sample and for mosaic generation, we use the camera.

10. **Click on the icon** to the right and drag upwards to move the stage into Z-direction to focus the sample in 10x or 100x magnification camera.



11. **To achieve clarity** of the sample, focus at 10x first, then go to 100x. **Click on autofocus icon** at the right corner toolbar. Autofocus with caution by clicking on the enter key the moment you achieve sample clarity so that the sample does not penetrate the rectangular aperture and damage the Be-windows. Note that the polycapillary X-ray optics and the Be-windows of the SD detector are closer to the rectangle aperture, which is unprotected.



12. **Switch back** to 10x

3. Creation of mosaic image

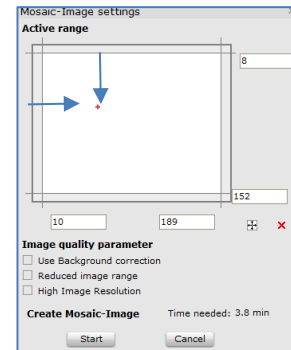
1. **To create a mosaic image**, click on the icon to the right and map the surface of the sample by first moving the stage in direction of the cursor to the top left-end corner of the sample.

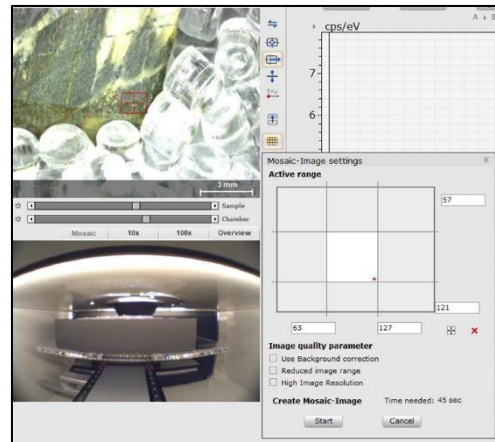
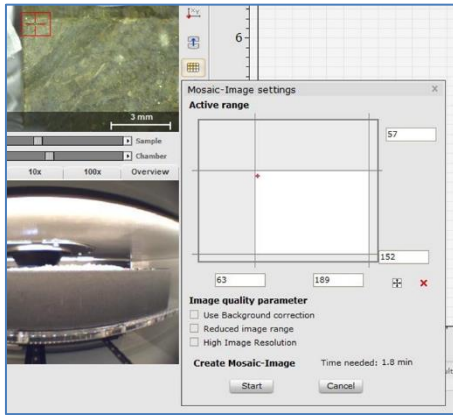


2. **Click on** the icon to open mosaic image settings.

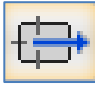




3. Since the spot is positioned at the top left corner of the sample, click and drag the upwards line down to the red icon and move the left line closer to (X&Y) lines, as shown with the arrows and below (left).





4. Click on cancel.

5. Click on this icon  and move the stage again in direction of the cursor to the bottom right corner of the sample.

6. Drag the downward line upwards close to  and also drag the right line (X&Y) lines closer to  as shown above right.

7. Select Background correction and Reduced image range.

8. Click start to generate a mosaic image (right)

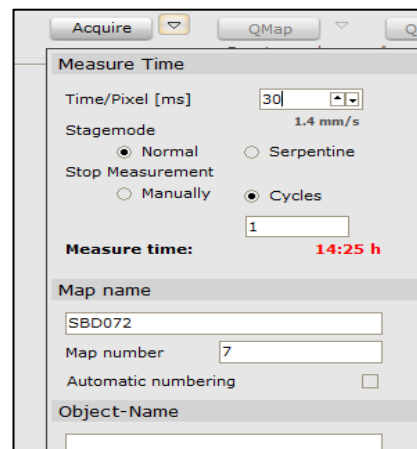
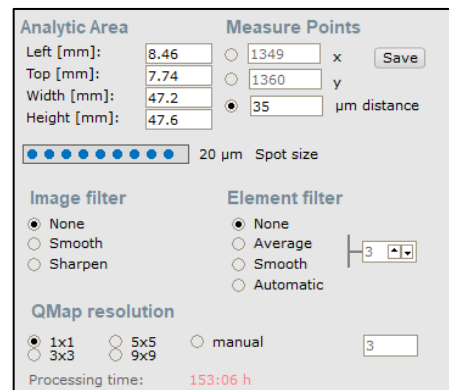
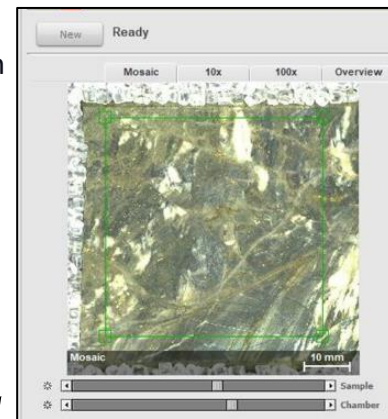
9. Switch to area mode on Title/Top Bar and select the area of interest on the surface of the sample for map scan by clicking on the green rectangle which turns to yellow to define the scanning range.

10. Under the measure points, change the pixel spacing:(μm distance) to arrange of 25-50 μm as shown to the right

11. Click on the downward-facing arrow next to Acquire and enter the parameters

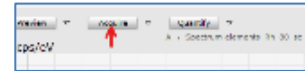
12. Click OK

13. Check to make sure the tube voltage and current are set to 50kv and 600 μA by clicking on the X-ray Tube 1 downwards facing arrow, first switch to no filter and then back to filter to set the voltage and



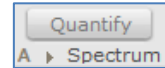
current condition

14. Click on the **Acquire** button and the map will start scanning.



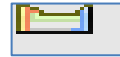
15. While the map is scanning, click on the periodic table and select the elements that you think may be present in the sample.

16. After the map is generated, click on **A** under **Quantify** to change **A** → **i**.




17. Click on **quantify** >> **Spectrum** for Element Identification (finding the elements that best fit the peaks).


18. Click on the icon (right) to open the periodic table.



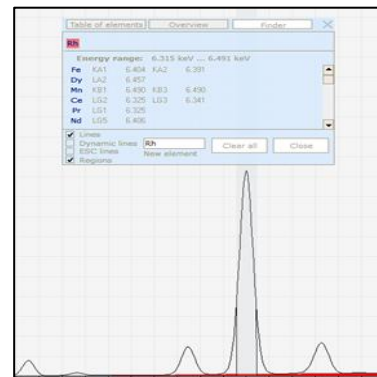
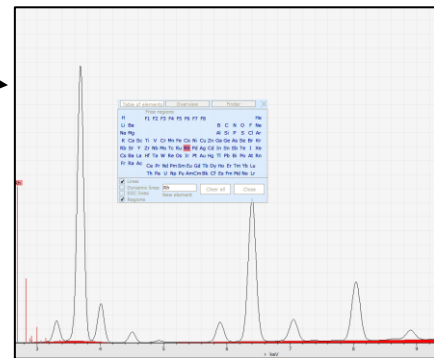
19. Right-click + drag to highlight peaks.

20. Click on **Finder** on the periodic table to view the available elements, and choose the element that best fits the peak.

21. Use  icon to auto X- and Y-axis once.

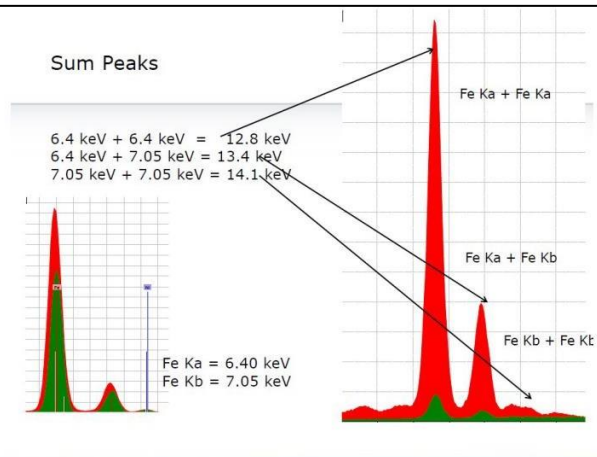
22. Click on  to zoom the spectrum.

23. When identifying elements that best fit the peaks, look out for artifacts (Sum peaks, Escape peaks).



• **Sum (pile-up) peaks**

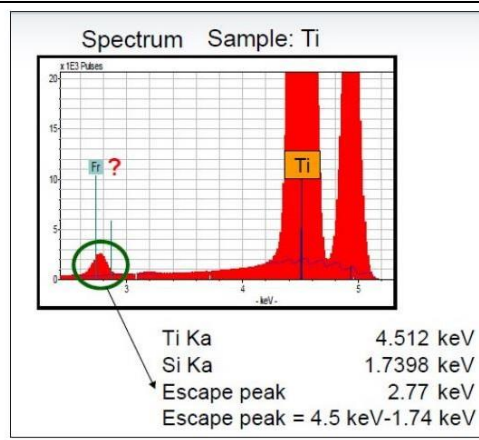
- Two or more energy pulses arrive at the detector simultaneously
-



- **Escape peaks**

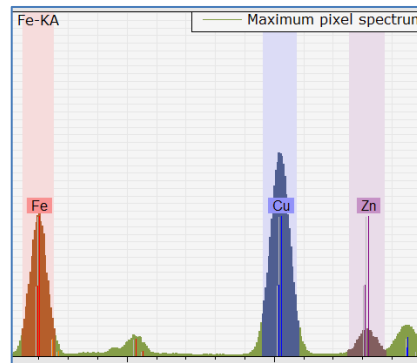
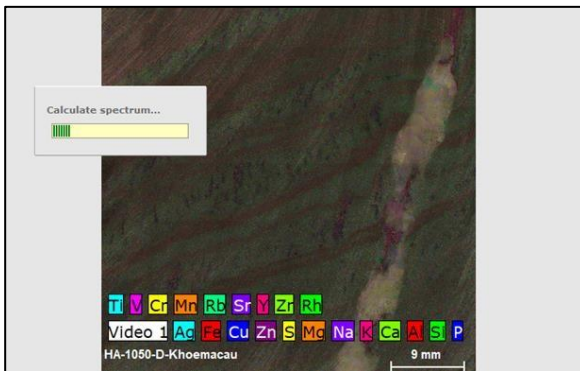
- Incoming X-ray displaces a silicon atom in the detector
- X-ray loses energy proportional to the Si-K α energy (1.74 keV)

Ca-K α escape peak: 1.951 keV
 P-K α = 2.013 keV

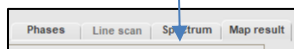


6. Maximum Pixel Spectrum

1. Use the maximum pixel maximum pixel spectrum icon to calculate the maximum pixel value within each X-ray energy plane.



2. Click on view peaks.




3. After using the maximum pixels, click on the map result to generate the final map.

4. Click on to select and unselect the map.



5. Using the bars below, adjust the brightness and contrast of the maps.

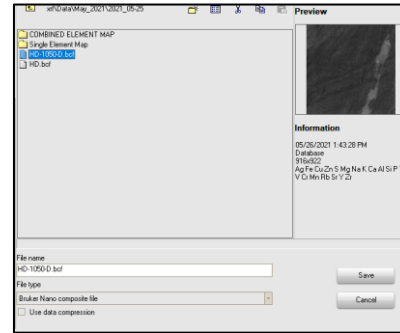
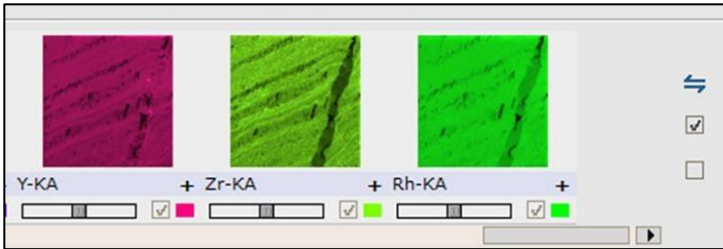


6. Use this icon  to check the final appearance of the map.

7. Click on export image button >> save under database. 

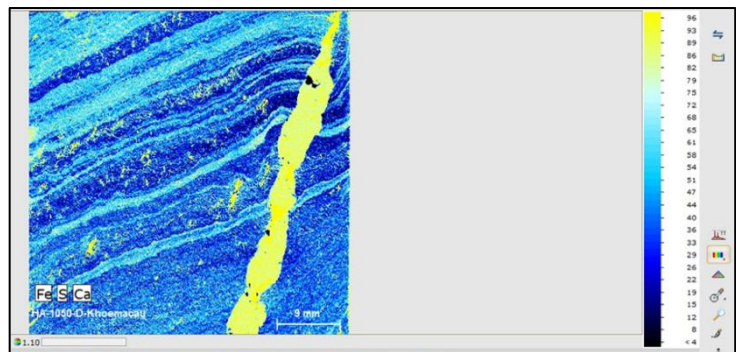
8. Save the project in the XRF folder after entering the file name (projectfile type is saved as bcf).

9. Tick  and Click on  export mapping data save individualmaps to the working folder.




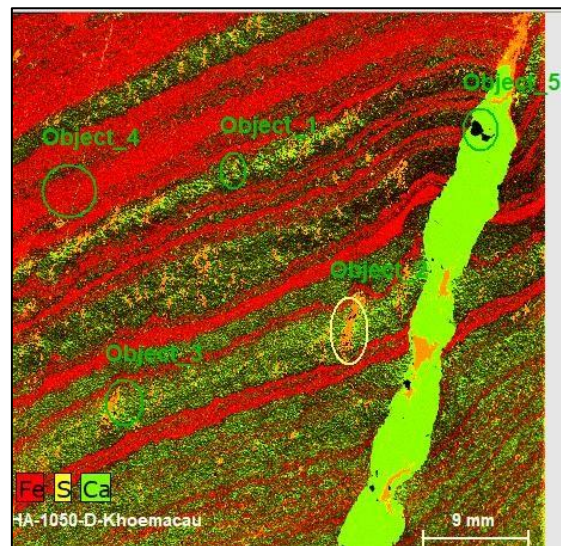
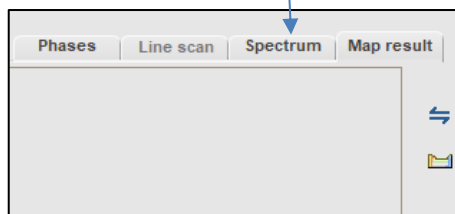
7. Generating heat maps

- Click the downward-facing arrow next to change the palette settings to create a heat map.



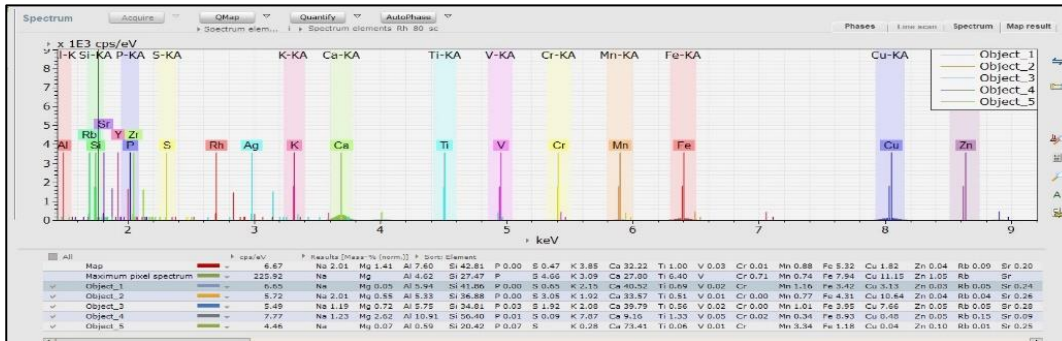
8. Analyzing an object on the sample surface


1. Click the downward-facing arrow next to objects  and select the object tool of interest.
2. Use the object tool to select the object of interest on the sample surface (right).
3. To delete the selected object on the sample, unselect the object tool, click on the selected object on the sample, and press the delete key.
4. Click the spectrum button.




5. Uncheck the checkbox All for spectrum display.

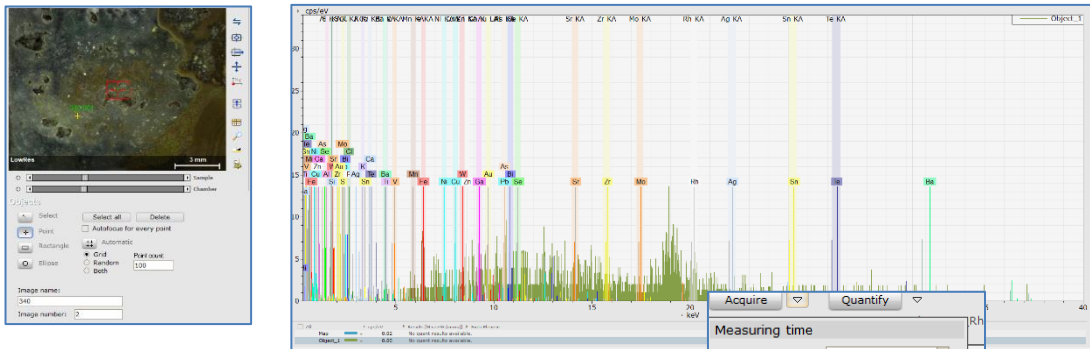
- Select and highlight the object of the interest spectrum
- Change A-i and quantify the selecte spectra



- Click this button  to save the pectrum result in the working folder
- Under the result table, click save to save the results in excel format

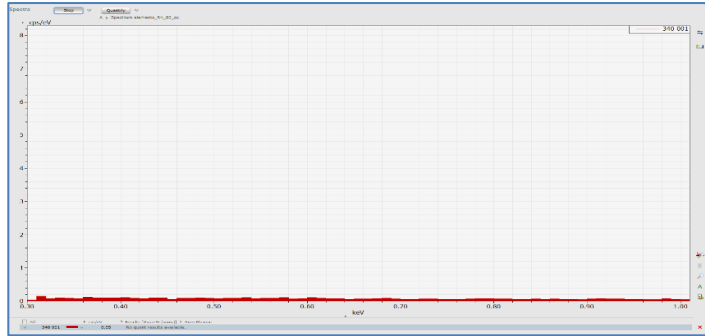
8. Energy Calibration


- To correct the peaks to fit well, click on multi-points on the Title/Toolbar
- Select the point  under objects and click on the sample surface to generate a sample point.
- Enter the image name and number.

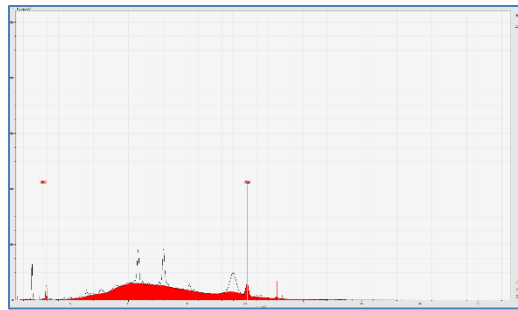
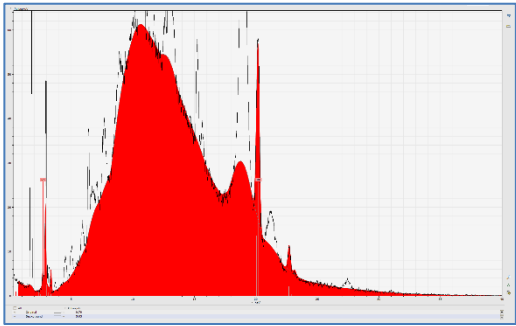


- Go to acquire, click on the downwards-facing arrow and enter the measurement conditions for multi-point analysis as shown right.
- Click Ok.
- Check that the voltage is 50kv, and the current is within the range of 200-600 µA.

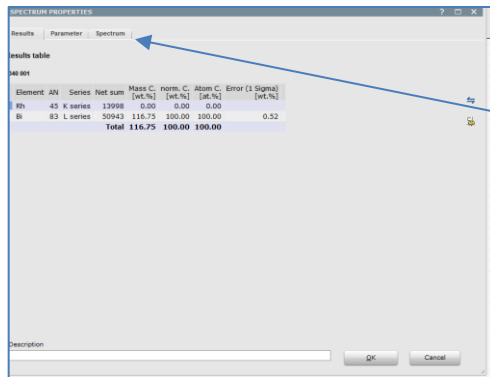
7. Hit on acquire to start running
8. Change A-i and click on quantify




9. Click on  on the right tool bar at the spectrum interface to autoscale the spectrum



10. Double-click on



Click on spectrum to open the spectrum tab

11. Define two energies by selecting the energies lines which will automatically be defined
12. Click on this icon  4 or 5 times until the linear, absolute, Fano factor (Detector parameter) and FWHM Mn values stabilize
13. Under the result table, click save to save the results in excel format

<

Vita

Hannah Adwoa Buamono was born, raised, and educated in Ghana. After completing her undergraduate degree in Earth Science, she worked as a field geologist for two mineral exploration companies, exploring gold in an orogenic deposit system. Hannah began her graduate studies in geological sciences at UTEP in January 2021, working under Dr. Antonio Arribas. In her studies at The University of Texas at El Paso (UTEP), she earned an official Certificate in Geographic Information Science and Technology (GIST). She worked as Research and Teaching Assistant. In addition, Hannah interned at First Majestic Silver Corp.'s Jerritt Canyon Gold Mine in Elko, Nevada, exploring Au in the Carlin Belt.

Her research focused on economic geology, utilizing advanced technologies like scanning μ XRF to understand geologic events in ore deposits.

While at UTEP, she also served as treasurer of the Society for Economic Geologists Student Chapter. The College of Science honored her with an honorary role as Graduate Student Marshal of Students in Fall 2022 in recognition of her high academic standing.

Email: Habuamono@miners.utep.edu

Adwoanhyira67@gmail.com